Institut für Physikalische und Theoretische Chemie der
Technischen Universität München

Advancing and Developing Experimental Methodologies for Studying Ultrafast Photoinduced Processes in Liquid Solutions

Anton Aleksandrov Trifonov

Vollständiger Abdruck der von der Fakultat für Chemie der Technischen Universität München zur Erlangung des akademischen Grades eines

Doktors der Naturwissenschaften

genehmigten Dissertation.

Vorsitzender:	Univ.- Prof. Dr. St. J. Glaser
Prüfer der Dissertation:	
	1. Univ.- Prof. Dr. T. Fiebig, Boston College, MA / USA
	2. Univ.- Prof. Dr. Dr.h.c. A. Laubereau

Die Dissertation wurde am 30.08.2005 bei der Technischen Universität München eingereicht und durch die Fakultät für Chemie am 27.10.2005 angenommen.

Table of Contents

1. Introduction

The work presented in this dissertation was conducted between September 2001 and November 2004 in the laboratories of Prof. Torsten Fiebig at the Technical University Munich and at Boston College (Boston, USA). This thesis summarizes the diverse scientific activities that I was involved in during these three years, starting from the design and development of ultrafast spectroscopy instrumentation, their application to various molecular systems in the condensed phase, and ending with the first steps towards establishing a new experimental methodology for measuring excited state structural changes.

A significant effort was spent on the design of a state-of-the-art femtosecond pump-probe setup using a laser induced white light for probing (**Chapter 2**). The diversity and complexity of the molecular systems of interest require a broad probing window, ranging from the UV to the NIR. Femtosecond broadband spectroscopy provides a unique possibility to *simultaneously* monitoring transient (excited state) absorption, stimulated emission and ground state bleaching.

In addition, during the course of this work a home-built picosecond laser was developed as an excitation source for fluorescence lifetime measurements utilizing time-correlated single photon counting technique.

The spectrum of systems studied in this dissertation ranges from solvated electrons and labeled DNA bases to more complex artificial and natural multichromophore systems. The scientific scope of this work is directed towards the nature of molecular excited states, the degree of electronic delocalization in multichromophores, mixing and electron transfer coupling. Because of the diverse nature of these projects we will present a brief description of the scientific background in the beginning of each chapter. The thesis is outlined as follows:

Chapter 3 describes our experimental results on **electron transfer in a model pyrene-labeled DNA base** 5-pyrenyl-2'-deoxyuridine (**PydU**) using fs-broadband pump–probe spectroscopy. The dynamics of **PydU** in a nonprotic solvent (acetonitrile) was compared to the

dynamics in a protic solvent (methanol). Evidence for the formation of a planar intramolecular charge transfer state is presented. This structural change accompanies the formation of pyrene radical cations. The temporal evolution of the excited state absorption spectrum provides a direct evidence for a greatly enhanced electron transfer (ET) yield in methanol. These results will be discussed in terms of hydrogen bond dynamics and their involvement in DNA ET.

After studying the dynamics of the isolated **PydU** in organic solvents, the next step was to utilize **PydU** in DNA and to study the mechanism of **electron injection and subsequent interbase electron shift** using **PydU** as electron donor and 5-bromo-2'-deoxyuridine (**Br-dU**) as electron acceptor. Again, broadband pump-probe spectroscopy has been applied. The observation of kinetic dispersion in the lifetimes of the charge transfer states will be reported and discussed. Important general conclusions regarding time-resolved measurements in DNA are drawn.

The further investigations in **Chapter 3** are focused on the study of ultrafast **local structural dynamics and excitation energy transfer in DNA** using a **pair** of pyrenyl-labeled DNA bases. The temporal evolution of the femtosecond pump-probe spectra reveals the existence of two electronic coupling pathways – through-base stack and through-space – which lead to excitation energy transfer and excimer formation even when the labeled DNA bases are separated by one A-T base pair. The data explicitly show that the electronic coupling which mediates through-base stack energy transfer is so strong that a new absorption band arises in the excited state absorption spectrum within 300 fs. From the analysis of time-dependent spectral shifts due to through-space excimer formation, the local structural dynamics and flexibility of DNA can be characterized on the picosecond and nanosecond time scales.

The work on the functionalized DNA bases and DNA oligonucleotides has been conducted in collaboration with the group of Dr. Achim Wagenknecht (TUM). The various results presented in **Chapter 3** have been published in three publications which appeared in *Chemical Physics Letters, Angewandte Chemie*, and *The Journal of Physical Chemistry B.*

In **Chapter 4** the photophysical properties of a series of acridinetriarylamine redox cascades are reported. The purpose of these artificially syntesized cascades is to promote **photoinduced hole transfer from an acridine fluorophore into an adjacent triarylamine**. The rates of hole migration along the redox gradient, tuned by substituents attached to the triarylamine redox centers are determined by fs-broadband pump-probe experiments. Our studies reveal different dynamic processes in the cascades depending on the solvent polarity, e.g., direct charge separation after photoexcitation vs a two step hole transfer mechanism. The work presented in **Chapter 4** has been done in collaboration with Prof. Christoph Lambert (University Würzburg) and recently published in *The Journal of the American Chemical Society*.

Chapter 5 is dedicated to the study of the **electron photo detachment dynamics** after resonant excitation of the lowest charge transfer state of **aqueous iodide solution** at various temperatures. As described in detail in Chapter 2, in this experiment we have generated and applied a probe white light with a very broad spectrum (400 - 1100nm) in order to reveal more spectral features of the observed transient absorption band. The kinetic analysis suggests that (at least) two intermediate states are involved in the photo dissociation process. The first intermediate builds up with a time constant of 220–180 fs in the investigated temperature interval (25-75°C) and has been assigned to an iodine:electron pair in a transient solvent configuration. Subsequent solvent reorganization leads to a quasi-equilibrated hydrated atom:electron pair state that builds up with a time constant of 700–540 fs. The following relaxation seems to be governed by partially diffusion-controlled recombination of the electron in the presence of an attraction potential well with depth of about 850 cm^{-1}. This work was conducted in collaboration with Prof. Alfred Laubereau and Dr. Hristo Iglev (TUM) who developed a theoretical model based upon the kinetic analysis of the transient spectra. The results were published in a joint publication in *Chemical Physics Letters.*

Finally, **Chapter 6** describes the development of a new methodology to measure time-dependent excited state **circular dichroism** (CD) spectra. This exciting new approach goes conceptually beyond conventional pump-probe spectroscopy and demonstrates a new way to

probe structural changes in the excited state of molecules and molecular assemblies in chiral environments. In this chapter we present an outline of the general principle of this approach, discuss the polarization properties of the broadband white light continuum, and present preliminary results which demonstrate the technical feasibility of fs-broadband CD spectroscopy.

2. Experimental methodologies

2.1. Femtosecond broadband pump-probe setup.

2.1.1. Femtosecond pulse sources.

All time-resolved pump-probe measurements presented in this thesis were performed with the home-built femtosecond pump-probe spectrometer, shown in Figure 2.1. The laser source is a commercial Ti:sapphire amplifier system (Clark MXR CPA2001) producing 775nm, 1 kHz, 170 fs, 800μJ pulse train. Approximately one third of the output is split into two beams using the beamsplitter BS (R=92%) with energies of 4 μJ and 230 μJ, respectively. The high energy beam is used to pump a commercial two stage visible noncollinear optical parametric amplifier (Clark MXR NOPA). The output of the NOPA is a chirped broadband pulse, tunable between 470 – 720 nm with energies of about 7-20 μJ which is compressed using a two prism (P1 and P2) compressor.[1] The measured output spectra are shown in Figure 2.2(a) and they are taken using commercial fiber spectrograph (Ocean Optics USB2000). After the compression the autocorrelation traces are measured by a commercial autocorrelator (APE PulseCheck™) and are depicted in Figure 2.2a) The resulting pulse durations are typically between 28-40 fs FWHM, assuming Gaussian pulse shape. In the experiments, carried out in the course of current work the excitation pulses were produced by second harmonic generation (SHG) of the NOPA output in a 100 μm thick BBO crystal (type I phase matching) and subsequent compression.[2] Since the phase matching bandwidth of the doubling crystal is limited to ~7nm in the near UV range, the converted pulses width is broadened to ~70fs. In order to minimize Fresnel losses in the compressor prisms (P3 and P4) the polarization of the second harmonic must be the horizontal. To fulfill this condition, the NOPA output polarization before the doubling crystal is changed from horizontal to vertical by a periscopical pair of mirrors M7, M8, twisted at 90° in the horizontal plane.

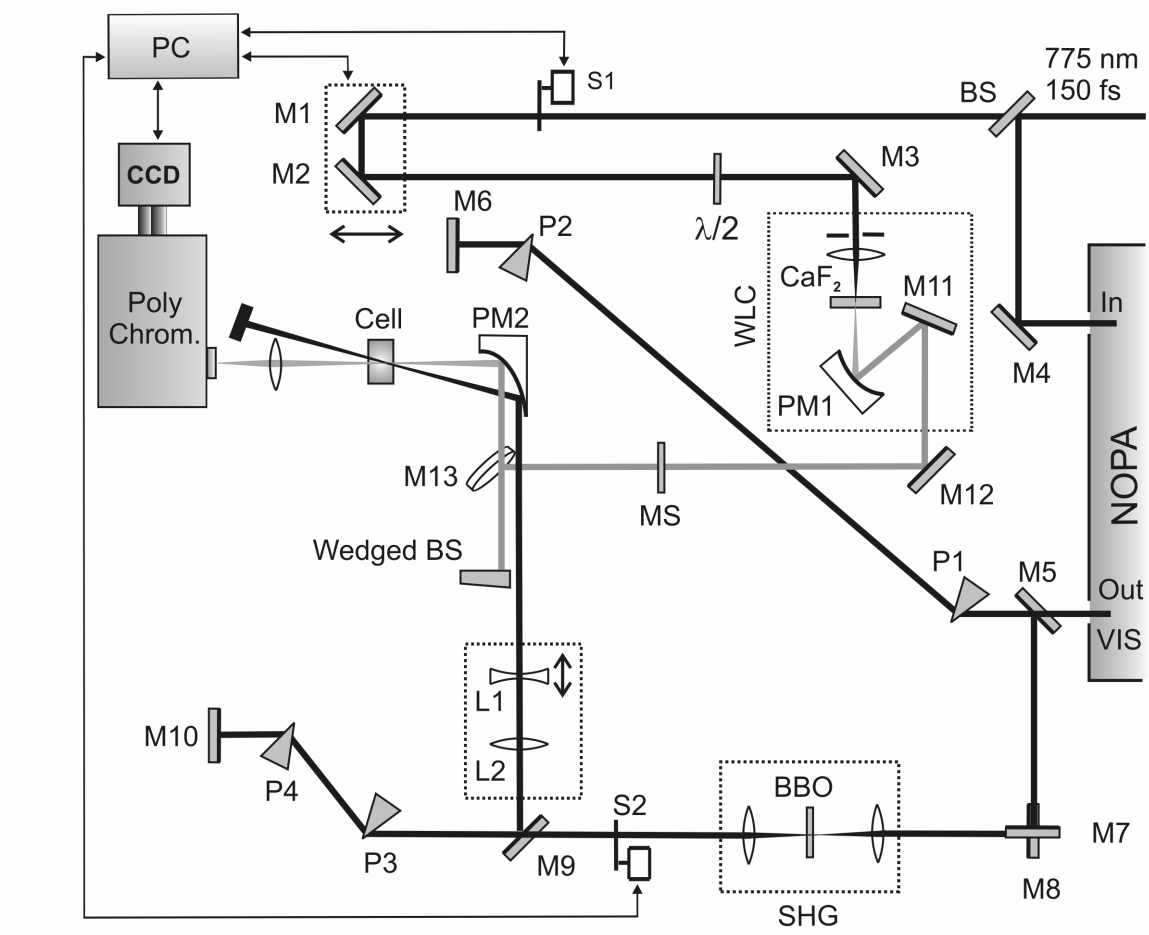

Figure 2.1. : *Schematic representation of the transient absorption experimental setup. The following abreviations are used: BS - beamsplitter of the fundamental 775nm beam; S1 and S2 - two motorized shutters which block the probe and pump beams respectively; M1, M2, M3 and M4 - high reflection dielectric mirrors at 775nm, 45°; l/2 - a l/2 plate; CaF_2 – calcium fluoride plate that is used for white light continuum (WLC) generation; M5, M6, M7, M8, M9, M10, M11, M12 and M13 - aluminum mirrors; PM1 - 30° off-axis parabolic mirror; PM2 - 90° off-axis parabolic mirror; MS - a stack of dielectric filtes used to cut off the fundamental; wedged BS - a wedged beamsplitter that is used to split the WLC into probe and reference beams, respectively; P1, P2, P3 and P4 - fused silica prisms; L1, L2 – telescopical system of lenses used for varying the spot size of the pump in the cell.*

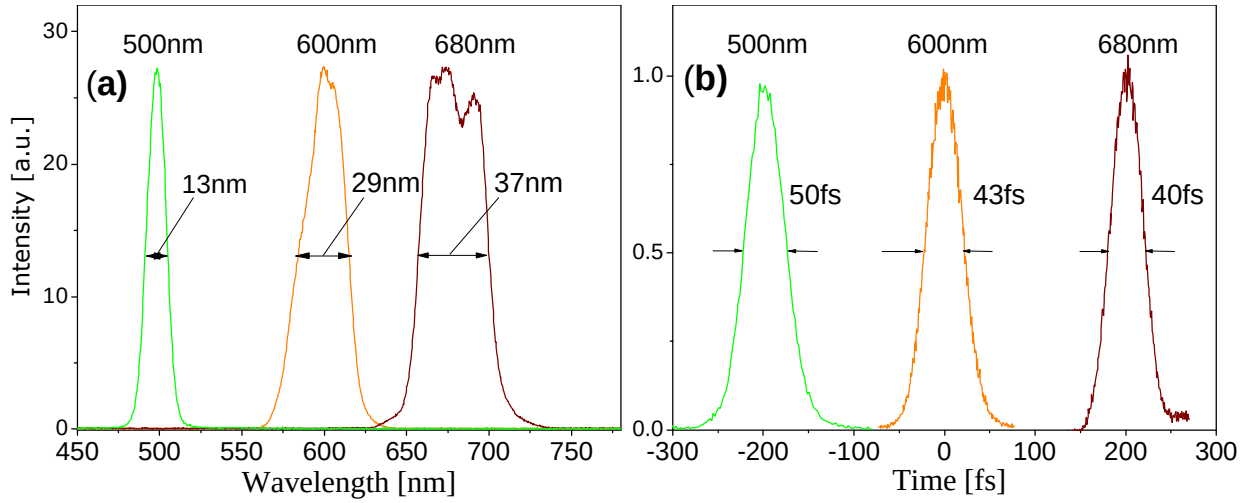

Figure 2.2. *(a) Typical output spectra from the NOPA. The amplification bandwidth is optimized for shortest pulse performance. (b) Autocorrelation functions for the NOPA output pulses. Pulsewidths are in the range 28-36 fs FWHM, assuming Gaussian pulse shape.*

2.1.2. Probe white light generation and characterization.

The optical density changes induced by optical pumping in the sample are probed by a femtosecond white-light continuum (WLC) which is delayed by using a 2ns-range, 0.2μm resolution computer controlled translation stage (PI-M5.11). The WLC is generated by tightly focusing of the lower energy beam (~4 μJ) in a 3-mm thick rotating CaF_2 plate using lens with focal length of 100 mm. By adjusting the parameters of the beam with neutral density filters and a diaphragm a self focusing mode can be achieved. It is possible to obtain a single filament WL by increasing the input energy beyond the self focusing point. Collimation of the wide spectrum WLC is performed by 30° off-axis parabolic mirror PM1 with off-axis focus length 77 mm. A dielectric mirror MS with custom design multilayer coating is used for attenuation of the fundamental (775 nm) and to smooth the probe spectrum (Figure 2.3 inset). The filtered WLC provides a usable probe source between 320-750 nm. The WLC pulse passes through the CaF_2 plate and subsequent optical elements which introduce a chirp due to the group velocity dispersion (GVD) i.e. its different spectral components accumulate different group delays. As a result different spectral components of the WLC pulse are interacting with the excited sample

molecules at different delay times. Before entering the sample the WLC spreads in time typically from several hundred fs up to ps depending on the length of the passed

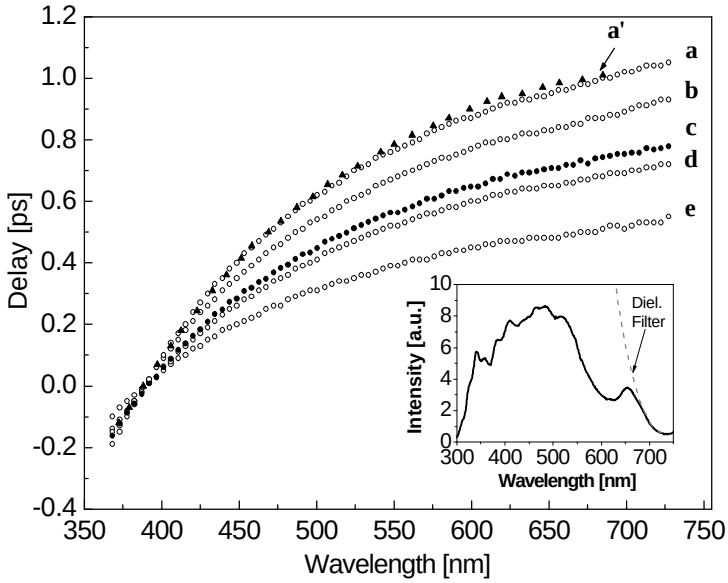

Figure 2.3. *Chirp measurements of the whitelight continuum (WLC) using the cross phase modulation (XPM) artifact (**a**-**d**) and the up-conversion technique (**a'**) in a 100 µm thick nonlinear BBO crystal. **a**, **a':** after propagating through a 1 mm cell, filled with solvent, **b**: after propagating through an empty cell (2×1.25 mm), **c**: resulting chirp used for the time correction (**c** = **d** + (**a**-**b**) / 2), **d**: after propagating through a single cell wall (1.25 mm quartz), **e**: in the absence of a cell. Inset shows typical spectra of WLC generated in 3mm CaF_2 crystal and relative transmission dependence of the used dielectric filter MS (shown in Fig 2.1).*

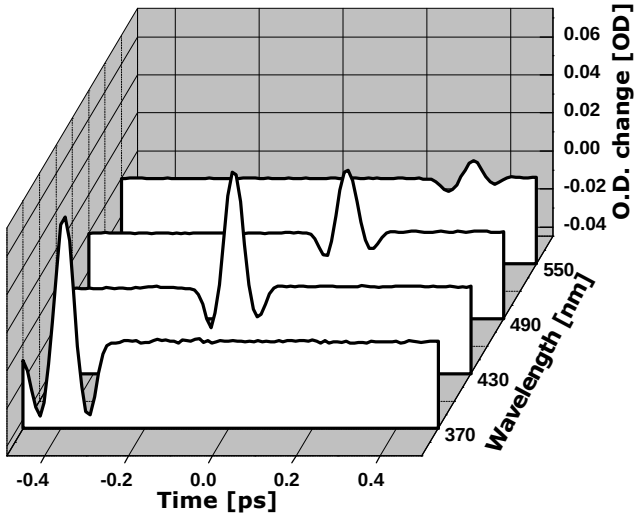

Figure 2.4. *Cross phase modulation (XPM) artifact generated in MeOH using excitation wavelength of 340 nm.*

dispersion material. To minimize the chirp in the current setup the overall thickness of the traversed optical material is reduced to only 2.25mm of low-dispersion fused silica. A stack of customized dielectric mirrors (filters) MS is made of two dielectic coated fused silica substrates with a thickness of 0.5 mm each. In the very broad probe spectrum, covering the entire range from 320 to 750 nm the "time-zero" is spread typically for 0.9 to 1.3ps (Fig. 2.3). Hence, in order to correct the wavelength dependence of "time-zero" in the transient absorption experiments one has to characterize the group delays of the different spectral components of the WLC very accurately.

All chirp-measurement techniques are based on c^2 as well as c^3 type nonlinear interaction between the WLC and a gate femtosecond pulse.[3-7] Several workgroups have reported recently a method based on a c^3 nonlinear process of cross-phase modulation (XPM) between a pump and a probe pulses interacting in the sample medium of a transient abortion experiment where a XPM artifact is observed.[4, 6-8] This XPM artifact provides a very convenient way to characterize the chirp because the measurement can be carried out in the same experimental arrangement as used for measuring the pump-probe spectra. However, the physical phenomenon which results from XPM is very complicated. An approximate description of the XPM artifact can be given assuming Gaussian shape wave packets and a linear chirp of the phase modulation function, where the artifact behavior strongly depends on the ratio of the value of chirp rate parameter and the square of pump pulse duration.[6, 7] Unfortunately, this simplified description does not guarantee a universally valid prediction of XPM artifacts under real experimental conditions. In addition, one can observe a substantial decrease in the accuracy of the group delay measurements going from the blue to the red part of the WLC (Figs. 2.3 and 2.4). Therefore, a second method can be used and it is based on sum-frequency generation between pump and the WLC to verify the results of the XPM artifact measurements. For the sum-frequency generation one 100μm thick BBO crystal (32° cut) and a gate pulse (35 fs, 675nm, 5 μJ) derived from the NOPA are used. The sum-frequency was detected using the commercial fiber spectrograph . In order to obtain the XPM artifact signal from the frequency-doubled NOPA output is used as gate

pulse (340nm), focused in the same 100μm thick BBO medium. Figure 2.3 (a and a') shows that both methods give similar results (within 7%). The precision of the chirp measurement is better then ±15fs. The accumulated group delay of the different spectral components of the WLC probe in the sample is obtained by measuring the chirp of the WLC in the presence and absence of the cell and the solvent, respectively (Fig. 2.3 b-e).

2.1.3. Data acquisition methods

After passing the mirror MS (for spectral smoothing) the WLC is split into two beams – probe and reference – using a wedged beam splitter. The reference beam is directed through a sample volume which is not affected by the pump pulse. Both the probe and reference spectra are detected independently and simultaneously by a CCD array. Pump, probe and reference beams are focused in the sample by a 90° off-axis parabolic mirror PM2 with off-axis focus length 100mm. The pump beam spot size in the sample is controlled by varying the distance between two lenses L1 and L2 with focal length 75 mm and -50 mm. Typical diameter of the pump spot is in the range of 200-600 μm. The pump energy varies between 200 and 800 nJ (measured using Coherent LM1 power meter), depending on the pump wavelength. The energy and pump spot size are adjusted to minimize contributions from the solvent to the signal. A sample cell with 1.25 mm fused silica windows and a light path of 1 mm is used for all measurements. All measurements are performed at the 'magic' angle (54.7°) between pump and probe pulse polarization to avoid contributions from orientational relaxation to the signal.

The detection system consists of an imaging polychromator (TRIAX 180, Jobin Yvon) and a CCD array (Hamamatsu S7031, 1044x128 pixels) cooled down to -20 °C using a multi stage thermo-electrical cooling (TEC) system.

To improve the sensitivity of the measurement a dual beam geometry (probe and reference) and a digital lock-in technique is implemented. The signals are collected in a four-step measurement cycle. In each step probe and reference signals are recorded at certain conditions

determined by the states of probe and pump shutters S1 and S2 in Figure 2.1, respectively. Hence, the four possible configurations of the shutters determine the spectral distribution of the transient absorption signal at a certain delay, which is given by:

$$OD = -\lg\left(\frac{I_{ps}^{pr+p} - I_{ps}^{p}}{I_{rs}^{pr+p} - I_{rs}^{p}} \Big/ \frac{I_{ps}^{pr} - I_{ps}^{0}}{I_{rs}^{pr} - I_{rs}^{0}} \right) \qquad (1)$$

where the lower index denotes the recorded probe (*ps*) and reference (*rs*) signal, respectively. The upper index characterizes the setting of the two shutters which control the pump (*p*) and the probe (*pr*) beams: *pr*: probe shutter is open, both the probe and the reference beam are passing through the sample; *p*: pump shutter is open, the pump is passing through the sample; *pr* + *p*: probe and pump shutter are open; 0 : both shutters are closed. Hence, the following signals are recorded during the full measurement cycle:

I. I_{ps}^{pr+p} , I_{rs}^{pr+p} : all beams are present in the sample;

II. I_{ps}^{pr} , I_{rs}^{pr} : probe and reference beams are present, pump beam is absent. The detector records the spectral distributions of the probe and the reference beam superimposed to noise;

III. I_{ps}^{p}, I_{rs}^{p} : only the pump beam is present. The detector records sample emission/scattering and noise;

IV. I_{ps}^{0} , I_{rs}^{0} : absence of all three beams. The detector records only the background noise.

The recorded signals at each step are result from integration, typically for several 100 laser pulses. The exact number of acquired laser shots within a single four steps cycle is selectable and depends on individual experimental conditions.

The overall sensitivity, i.e. the smallest absorbance change that can be measured is typically 2.10^{-4} or 0.2 mOD (1 mOD = 10^{-3} optical density units). The spectral amplitude of the signal before time zero (so-called baseline) is usually in the range of –2 to 2 mOD and is subtracted from the data.

2.1.4. Near infrared white light continuum generation

To observe the excited state absorption bands in the near infrared range (NIR) of 750 – 1200 nm an extended WLC is generated using an auxiliary parametric amplifier as a pump source (Figure 2.5a). The second NOPA produces 1180nm, 10μJ, 51fs (Figure 2.5(b), inset) pulses and the output beam is tightly focused in a CaF_2 spinning crystal with thickness of 3mm. The resulting continuum extends to the 400-1150nm range (Fig. 2.5 (b)), the chirp is characterized as described in paragraph 2.1.2. and the time-shift (chirp) correction is made using the dependency ***c*** as shown in Figure 2.3(a).

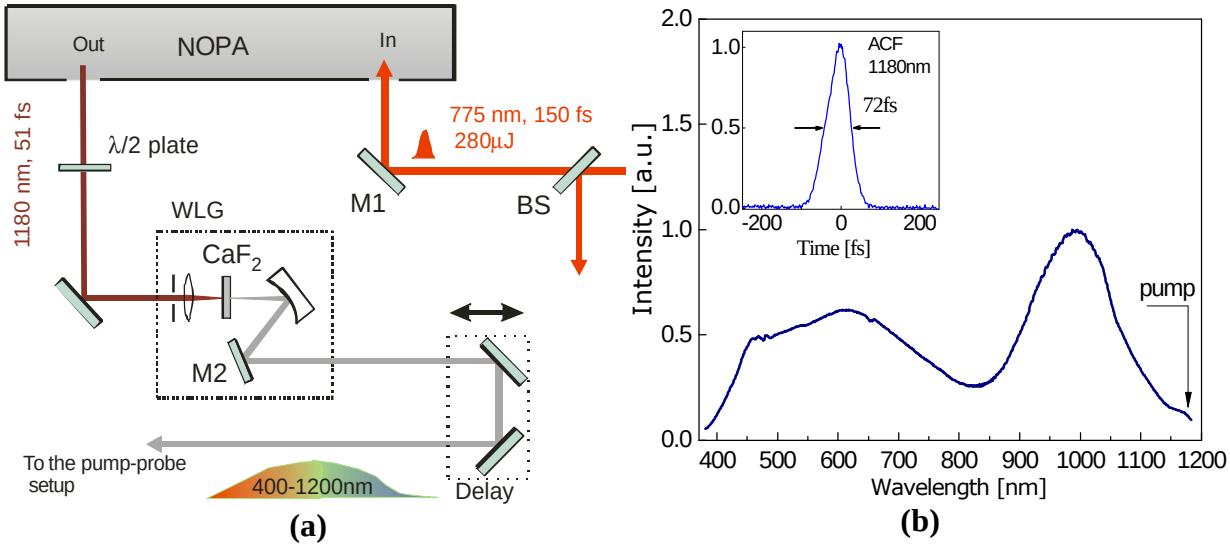

Figure 2.5. *(a) Schematic representation of the extended white light generation setup. (b) White light spectra generated using 1180nm, 50fs, 5μJ pulses. Inset shows an autocorrelation function of the second NOPA output 1180nm pulses.*

2.1.5. Numerical Data analysis

From the chirp characterization we obtained the relative time delay values between probe wavelengths. Hence, the temporal evolution of the entire pump-probe spectrum can be constructed by applying the proper time-shift correction. The time vector of the measured data is shifted for each spectral channel of the CCD according to the measured chirp. For the new time points are linearly interpolated the OD values between the OD values of the corresponding

nearest neighbor time points. However, for a quantitative analysis of the data determination of the absolute time-zero values with respect to the pump pulse is needed. This is realized by numerical deconvolution of an instantly rising spectral component $F_l(t)$ at a certain wavelength with an experimental response which is assumed to be a Gaussian function: $g(t)=1/(\pi^{1/2}\sigma)\cdot\exp[-\{(t-t_0)/\sigma\}^2]$. $F_l(t)$ is a sum of up to i exponentials:

$$F_l(t-t) = \sum_i c_i \, e^{-\frac{t-t}{t_i}} \qquad (t \geq \tau) \qquad (2)$$

The resulting time-dependent signal (at a given probe wavelength λ) $S_l(t)$ is given by:

$$S_l(t) = \int_{-\infty}^{t} g(t)\; F_l(t-t)\, dt \qquad (3)$$

which can be solved analytically to give:

$$S_l(t) = \sum_i c_i \cdot \frac{1}{2} \cdot \exp\left[-\frac{1}{t_i}\left(t - t_0 - \frac{s^2}{4t_i}\right)\right] \cdot \left\{1 - erf\left[\left(t - t_0 - \frac{s^2}{2t_i}\right)\frac{1}{s}\right]\right\} \qquad (4)$$

where *erf* is the error function and c_i is the amplitude of the component (i) with decay time t_i. s is related to the full width at half maximum (FWHM) of the experimental response (s = FWHM/1.6651). Here t_0 is the time shift fit parameter which is subsequently used to determine the absolute time-zero.

2.1.6. Time and spectral resolution

The overall instrumental response function (IRF) time resolution of the setup was obtained from the fit of the signal of acetonitrile solution of pyrene as a reference molecule system.[9] The excitation wavelength is set to 360nm to match the $S_0 \rightarrow S_2$ transition. Figure 2.6. represens the *instantaneous* rise of the optical density at 580nm, corresponding to pyrene transient $S_2 \rightarrow S_n$ absorption.[9] The data are analyzed by least squares fitting as described in the previous section 2.1.5. Assuming a Gaussian shape for IRF a width value of 125 fs (FWHM) is obtained and a decay constant of 89 fs (92%).

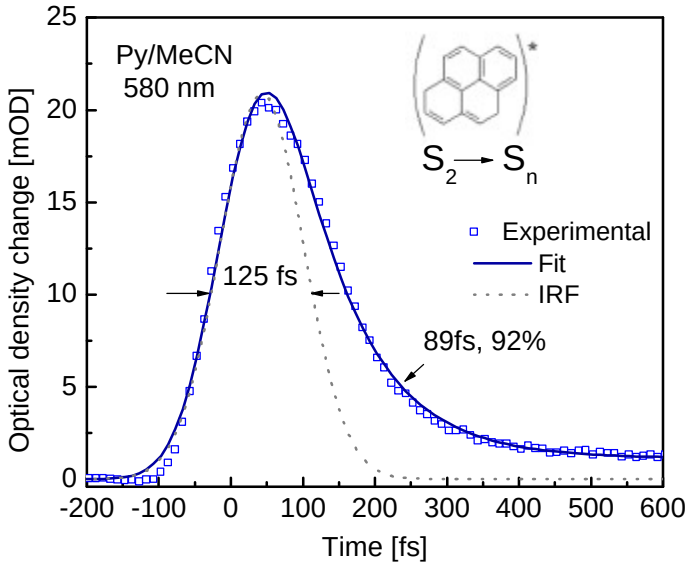

Figure 2.6. *Time-dependent change of optical density of pyrene in acetonitrile at 580nm. The sample cell optical path is 1mm.*

The spectral resolution of the experimental setup is determined by multi-peak Lorentzian fitting of reference Hg lamp spectra. For the entire range in use (320-750nm), a spectral resolution of 7 - 10 nm is obtained.

2.2. Picosecond time-resolved fluorescence setup

In recent studies [10-13] the fluorescent DNA base analogue 2-aminopurine (**Ap**) has been used as a probe for the investigation of DNA or RNA interactions. It has been shown that **Ap** does not change the DNA structure or disrupt the biological interactions of DNA. [11-13] The highly fluorescent character of **Ap** allows the direct base-to-base electron/hole transfer to be investigated using fluorescence lifetime measurement methods, in particular the time correlated single photon counting (TCSPC) technique. However, the lowest excited singlet state of **Ap** – which has p -p * character [14] – is shifted to longer wavelengths compared to those of the natural bases which allows selective excitation of **Ap** in DNA base stack in a spectral range around 320 nm. The simplest way this excitation wavelength to be made available is through fourth harmonic generation of short-pulsed laser oscillator working at ~ 1.3m m. However, such

lasers are not currently commercially available and therefore a customized Nd:YVO_4 picosecond pulse diode-pumped solid state laser (DPSSL) was designed and built. Since the amplification at the 1.32 μm laser line is almost four times less than at 1.06 μm we had to start the construction with a "conventional" wavelength 1064nm.

2.2.1. Passively mode-locked laser calculations and design.

Based on calculations for laser cavity in [15] a proper laser resonator is designed to minimize the influence of the induced thermal lens over the generated laser mode.

2.2.1.1. Resonator requirements for stable mode-locking operation.

The construction of diode-pumped solid state lasers (DPSSL) requires precise design of the laser resonator. The cavity requirements for highly efficient laser performance depend on the laser mode of operation, e.g. CW, Q-switching or mode-locking.

In the case of passive mode locking the stability of laser operation is a function of the beam waist radii in the active medium and in the passive mode-locking element.[16, 17] Therefore, the latter two parameters as well as the resonator g_1g_2 product are the three input parameters of our laser cavity design. In this context, a resonator calculation means to determine the optical components (curvature of the mirrors and focal lengths of the lenses) and their relative position, i.e. resonator spatial parameters, corresponding to these input conditions.

The most common approach is based on numerical fitting of the special parameters in order to comply with the desired beam waist radii.[18, 19] In this chapter we present a method for analytical calculation of 3- and 4-mirror resonators having as starting parameters the waist spot sizes and the g_1g_2 product.

In a passively mode-locked DPSSL using nonlinear mirror technique, strong requirements for tight focusing in the nonlinear mode-locker have to be fulfilled.[20-22] For mode locking by frequency doubling nonlinear mirror typical values of the waists in the active and in the nonlinear crystal are: w_C =300-600 μm and w_{NLC} =50-100μm, respectively.[20, 21] In the case of mode-

locking using a semiconductor saturable-absorber mirror (SESAM), the typical beam radii providing saturation of the amplification as well as absorption are 150-200μm for the active medium and 50-150μm for SESAM structures.[16, 22] In addition, higher numbers of modes can be supported by choosing long laser resonators. Resonator lengths in the range 1.0 -1.9 m corresponding to 150-80 MHz output pulse repetition rate are usually exploited.

General requirement for DPSSL resonator is to provide good overlapping between the pump beam and the laser mode in the active material.[23, 24] The optimum pump beam radius (w_{pump}) is determined by two opposing factors: reducing the pump beam diameter leads to lower threshold of the generation, but to higher thermal effect that is proportional to the square of l/w_{pump}.[25]

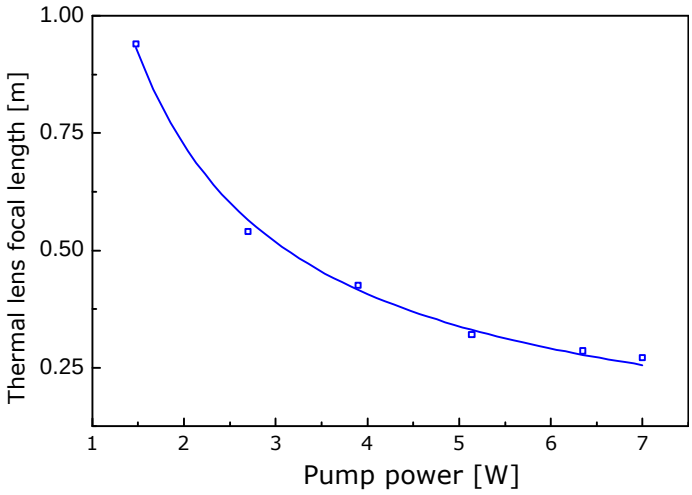

Figure 2.7. *Thermal lens focal length versus pump power*

To estimate the crucial impact of the thermal lens effect on the laser-diode pumping with power of over several watts, the thermal lens effective focal length is measured in the case of diode-pumped Nd:YVO_4 laser. The output of a fiber-coupled diode-laser array with maximal output power of 10 watts was focused into a spot size of w_{pump}=400 m m in the active crystal, 0.5% atomic concentration, a-cut Nd doped YVO_4. The thermal lens behavior was investigated by measuring the dependence of the TEM_{00} mode diameter in a 9 cm long plane parallel resonator, where one can consider the mode predominantly determined by the thermal lens. The diameter of the fundamental mode was measured as a function of the distance from the output mirror and

was extrapolated to obtain the beam waist radius at the output.[26] The results are shown in Figure 2.7. Approximation of the experimental data with the function $f_{th}=a/P^b$ gives: a = 0.13 m/W and b=0.83. The strong influence of the pump power over the thermal lens implies the design of a resonator working in a broad range of thermal lens focal lengths.

2.2.1.2. Implementation of the ABCD formalism to describe the resonator.

For description of the spatial parameters of the fundamental mode the ABCD laws of the geometric optics are used.[27] The beam waist radii of the fundamental mode at the mirrors as a function of the elements (A, B; C, D) of the single-pass matrix of the resonator are:

$$w_1^2 = \frac{l|B|}{p}\sqrt{\frac{g_2}{g_1(1-g_1g_2)}} \quad w_2^2 = \frac{l|B|}{p}\sqrt{\frac{g_1}{g_2(1-g_1g_2)}} \qquad (5)$$

where $g_1 = A - B/R_1$, $g_2 = D - B/R_2$, l is the wavelength of the laser radiation. For the widely used 3- and 4-mirror resonators in DPSSL typically the end-mirrors are flat. Starting with equation (1) one could obtain simple expressions for g_1 and g_2: $g_2/g_1 = (w_1/w_2)^2$. Assuming that the ratio g_2/g_1 is a known parameter as well as g_1g_2, which meets the stability condition $0 < g_1g_2 < 1$ and characterizes the resonator position in the stability diagram can be derived:

$$g_1 = \pm\sqrt{g_1g_2}\,\frac{w_2}{w_1} \;; \quad g_2 = \pm\sqrt{g_1g_2}\,\frac{w_1}{w_2} \qquad (6)$$

Applying these equations in the following sections analytical solutions can be obtained for the spatial parameters of the resonator as a function of the mode spot sizes w_1, w_2 and the g_1g_2 parameter.

2.2.1.3. Analytical solution for 3-mirror resonators

A common scheme of the resonator is shown in Figure 2.8. To fulfill the requirement for the beam diameters on the mirrors M_1 and M_3 one should select suitable values for L_1, L_2 and the radius of the concave folding mirror M_2. It can be assumed that the thermal lens is placed at the very surface of the mirror M_1, which is satisfied for end-pumped solid state lasers implementing a mirror-coated active crystal.

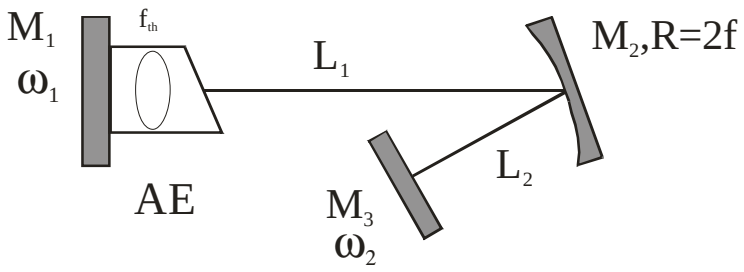

Figure 2.8. *Principle scheme of 3-mirror resonator.*

The following single-pass matrix describes the 3-mirror resonator:

$$M_S^V = \begin{vmatrix} A & B \\ C & D \end{vmatrix} = \begin{vmatrix} 1-\frac{L_2}{f}-\frac{1}{f_{th0}}\left(L_1+L_2-\frac{L_1L_2}{f}\right) & L_1+L_2-\frac{L_1L_2}{f} \\ -\frac{1}{f}-\left(1-\frac{L_1}{f}\right)\frac{1}{f_{th0}} & 1-\frac{L_1}{f} \end{vmatrix} \quad (7)$$

$$g_1 = 1-\frac{L_2}{f}-\frac{1}{f_{th0}}\left(L_1+L_2-\frac{L_1L_2}{f}\right) \quad (8)$$

$$g_2 = 1-\frac{L_1}{f} \quad (9)$$

Here f_{th0} is the focal length at which the beam waist radii over the mirrors M_1 and M_2 are w_1 and w_2 respectively. From equations (1) - (5) the analytical solutions are derived for L_1, L_2 and R in the case where both g_1 and g_2 are negative:

$$\frac{R}{2} = f = \frac{p w_1 \sqrt{1-g_1 g_2}}{l w_2 \left(1-g_1 g_2+\frac{\sqrt{g_1 g_2}\, p w_1 \sqrt{1-g_1 g_2}}{f_{th0} w_2 l}\right)} \quad (10)$$

$$L_1 = f(1-g_2); \quad L_2 = f\left(1-g_1-\frac{p w_1 \sqrt{1-g_1 g_2}}{f_{th0} w_2 l}\right) \quad (11)$$

From equations (4)-(7) the limits of the stability zone are determined using the conditions $g_1 g_2$ ($f_{\text{th-cr1}}$)=0 and $g_1 g_2$(f_{th0}) = 1 and for the critical values of the focal length of the thermal lens we have:

$$f_{th-cr0} = \frac{f_{th0} B w_1}{B w_1 - f_{th0} w_2 \sqrt{g_1 g_2}}; \quad f_{th-cr1} = \frac{f_{th0} B w_1 \sqrt{g_1 g_2}}{f_{th0} w_2 + B w_1 \sqrt{g_1 g_2} - f_{th0} w_2 \sqrt{g_1 g_2}} \quad (12)$$

Therefore $f_{\text{th-cr1}}$ exists for every f_{th0}, while $f_{\text{th-cr0}}$ exists only for $f_{th0} < w_1 B / w_2 \sqrt{g_1 g_2}$.

The equations for L_1 and L_2 show that the whole length of the resonator $L=L_1+L_2$ is determined entirely by w_1, w_2, f_{th0}, and the parameter g_1g_2. The first three parameters are essential for the operation of the laser while g_1g_2 determines the sensitivity of the resonator to the thermal lens effect and could be varied in order to obtain longer resonators. This is depicted in Figure 2.9 by an example showing the beam waist radii at M_1 and M_2 mirrors, w_1 = 400 μm, w_2 = 80 μm respectively, for the two different values of f_{th0} and g_1g_2.

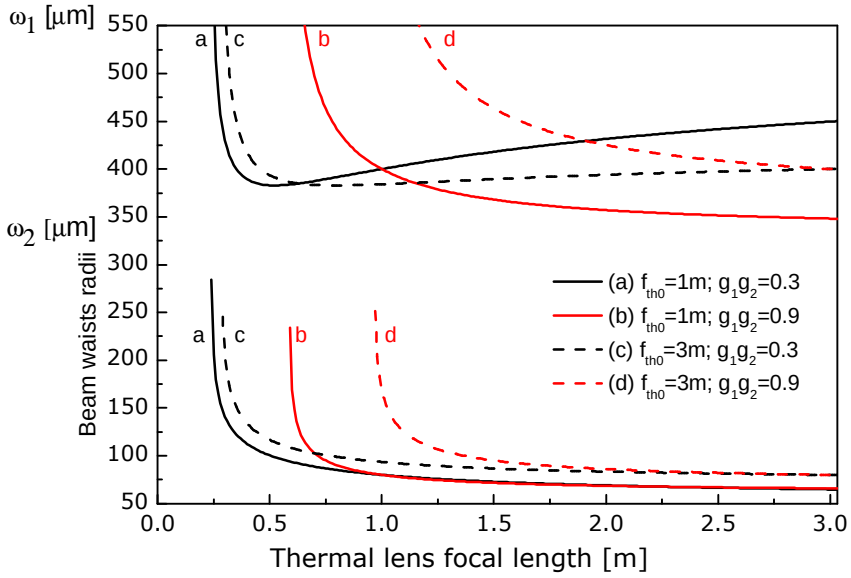

Figure 2.9. *Beam waists size w_1 and w_2 versus focal length of the thermal lens for resonator lengths: a) 0.41m; b) 0.85m; c) 0.49 m; d) 1.40 m.*

One can see that for values of g_1g_2, close to the critical stability condition g_1g_2=l, the length of the resonator is longer but more sensitive to changes of the thermal lens. Therefore it is possible to increase the length of the resonator with self-imaging system that consists of two identical lenses placed at a distance of twice their focal length. This technique increases the length of the resonator with four focal lengths without change of the beam parameters in

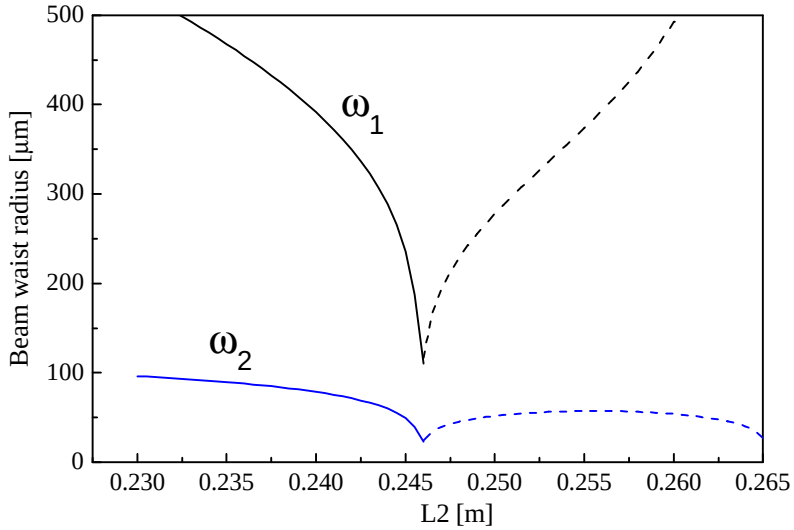

Figure 2.10. *Beam waists radii* w_1 *and* w_2 *versus* L_2 *for* f_{th}*= 3m (solid line) and* f_{th}*=0.3m (doted line). With small changes of* L_2 *one can obtain stable regime of operation in a broader range of thermal lenses conserving* w_1*, and* w_2 *close to the their initial values.*

the resonator. Another technique for construction of long laser resonators working for a broad range of thermal lenses relies on an appropriate selection of L_2 that provides $g_1(f_{th})=g_1(f_{th0})$ - this is shown in the example on Figure 2.10 associated with 'd' curve with initially calculated parameters using the formulae (6), (7): L_1 = 1.17 m, L_2 = 0.24 m and R = 0.40 m.

2.2.1.4. Reducing of 4- mirror resonators to 3-mirror resonators.

The optical scheme of a 4-mirror resonator used in DPSSL is show in Figure 2.11. It consists of two end-mirrors M_1 and M_4 and two folding mirrors M_2 and M_3 placed at a distance L_f.

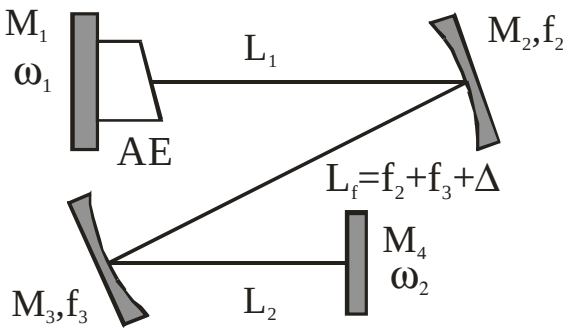

Figure 2.11. *4-mirror resonator scheme.*

The single pass matrix characterizing the 4-mirror scheme without taking into account the thermal lens is:

$$M_S^z = \begin{vmatrix} A & B \\ C & D \end{vmatrix} = \begin{vmatrix} 1-\frac{L_f}{f_2} - L_2\left(\frac{1}{f_2}+\frac{1}{f_3}\left(1-\frac{L_f}{f_2}\right)\right) & L_2\left(1-\frac{L_1}{f_2}\right)+\left(1-\frac{L_2}{f_3}\right)\left(L_1+L_f\left(1-\frac{L_1}{f_2}\right)\right) \\ \frac{\Delta}{f_2 f_3} & \left(1-\frac{L_1}{f_2}\right)-\frac{1}{f_3}\left(L_1+L_f\left(1-\frac{L_1}{f_2}\right)\right) \end{vmatrix} \qquad (13)$$

To find an analytical solution in an analogous way to the 3-mirror resonator, is a difficult problem because of the more complicated mathematical expressions for the matrix elements and because of the fact that there are only three initial conditions (w_1, w_2 and g_1g_2) to determine the unknown resonator parameters L_1, f_2, f_3, Δ and L_2.

We found a substitution reducing the M_s^z matrix to a matrix similar to the 3-mirror M_s^v matrix where the thermal lens effect is neglected:

$$L'_1 = L_1 + \frac{FL_f}{f_3}; \quad L'_2 = L_2 + \frac{FL_f}{f_2}; \quad F = \frac{\Delta}{f_2 f_3} \qquad (14)$$

where L_1', L_2', F could be determined from equations (6) and (7) for the 3-mirror resonator. The new variable F is a focal length $F(f_1, f_2, \Delta)$ of an effective lens. In order for the resonator to be in a stable regime the matrix element C must be negative. That means $L_{1,2} > L_{1,2}$' i.e. the 4-mirror resonator could provide longer resonator length than its equivalent 3-mirror one. For a full description of the resonator one should know additional initial parameters.

2.2.1.5. The laser resonator

The laser configuration is depicted in Figure. 2.12. The 4x4x4 mm Nd:YVO_4 crystal is pumped by a 808 nm fiber coupled diode laser (LIMO). The output power and fiber core diameter are 10 W and 400 μm, respectively. Two aspherical lenses L1 and L2 with focal lengths of 9 and 15 mm form a telescope. The laser cavity is closed on the active crystal side by a dichroic high reflectivity coating, directly on the Nd:YVO_4 crystal surface. On the other side, the frequency-doubling non-linear mirror (NLM)[28] consists of a 7-mm-long KTP crystal , cut

for oo-e type second harmonic generation (q = 39.2° j = 90°) and a dichroic mirror M5 with reflectivity above 99% at 532 nm and equal to 31% at 1064 nm. The nonlinear crystal mounting allows angle tuning and translation along the laser cavity axis. When the KTP crystal is tuned to the phase matching angle and translated at ~10 mm from the dichroic mirror, a noticeable increase of the SHG intensity reveals the efficient passive mode locking of the Nd:YVO_4 oscillator.

The average output power at 1064 nm was 0.7W for pump power of 8W. Although some works have shown that NLM can operate without additional mode locking, [28, 29] we observe a much more stable operation of the oscillator when a saturable-absorber mirror (SESAM) is used in the cavity. The obtained pulse train has a frequency of 70 MHz, corresponding to the resonator length of 214 cm.

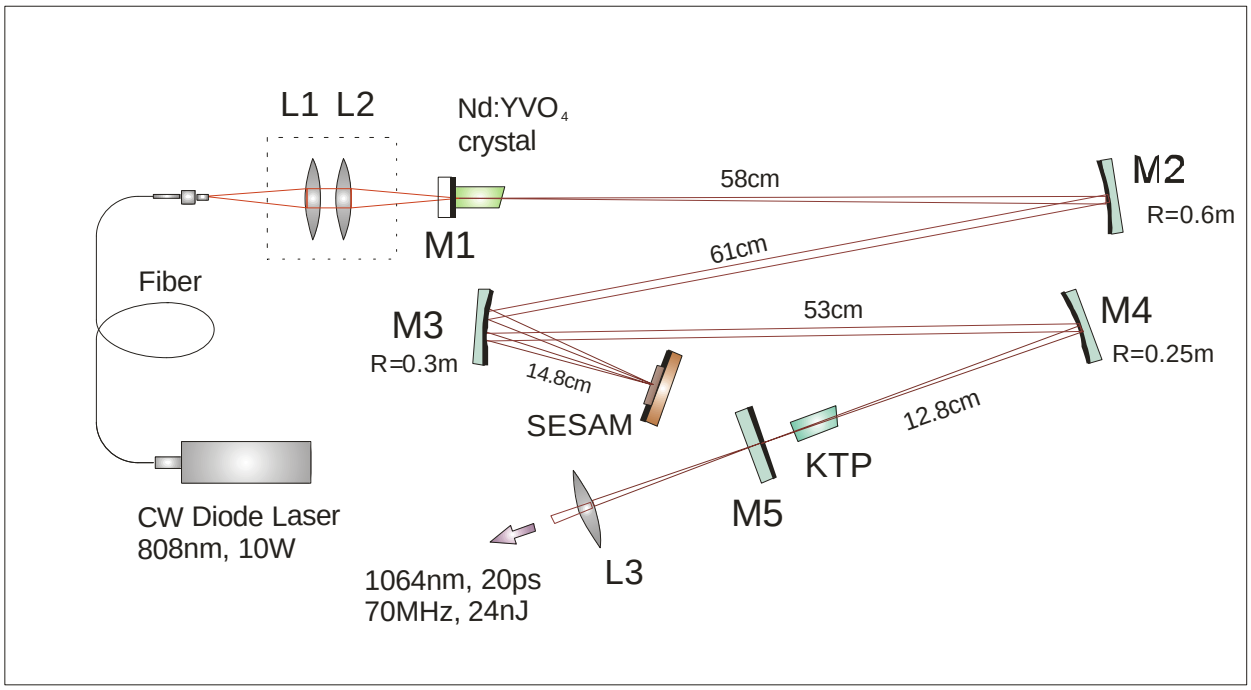

Figure 2.12. *Schematic diagram of the passive mode-locked Nd:YVO_4 laser. Used designations are: M1 – high reflective coating for 1064nm on the Nd:YVO_4 crystal; M2, M3, M4 – high reflection dielectric mirrors. M4 - R=90% output coupling mirror. SESAM – **se**miconductor **s**aturable **a**bsorber **m**irror with 1% unsaturated losses; L1, L2 – collimating and focusing lens, respectively; L3 – output collimating lens.*

2.2.2. Time correlated single photon counting setup

The apparatus for fluorescence kinetics is depicted in Figure 2.13. The output pulse train of the mode-locked Nd:YVO_4 is split into two using the beamsplitter BS (R=8%) and the main part of the power is focused through the lens L1 into a 5mm thick KTP nonlinear crystal (cut at q =39.5°, j =90°). The resulting 532nm pulse and the remaining fundamental are focused together using the lens L2 (f=50mm) into 6mm LBO nonlinear crystal (q =43°, j =90°) for third harmonic generation. The length of the KTP crystal is selected to compensate for its

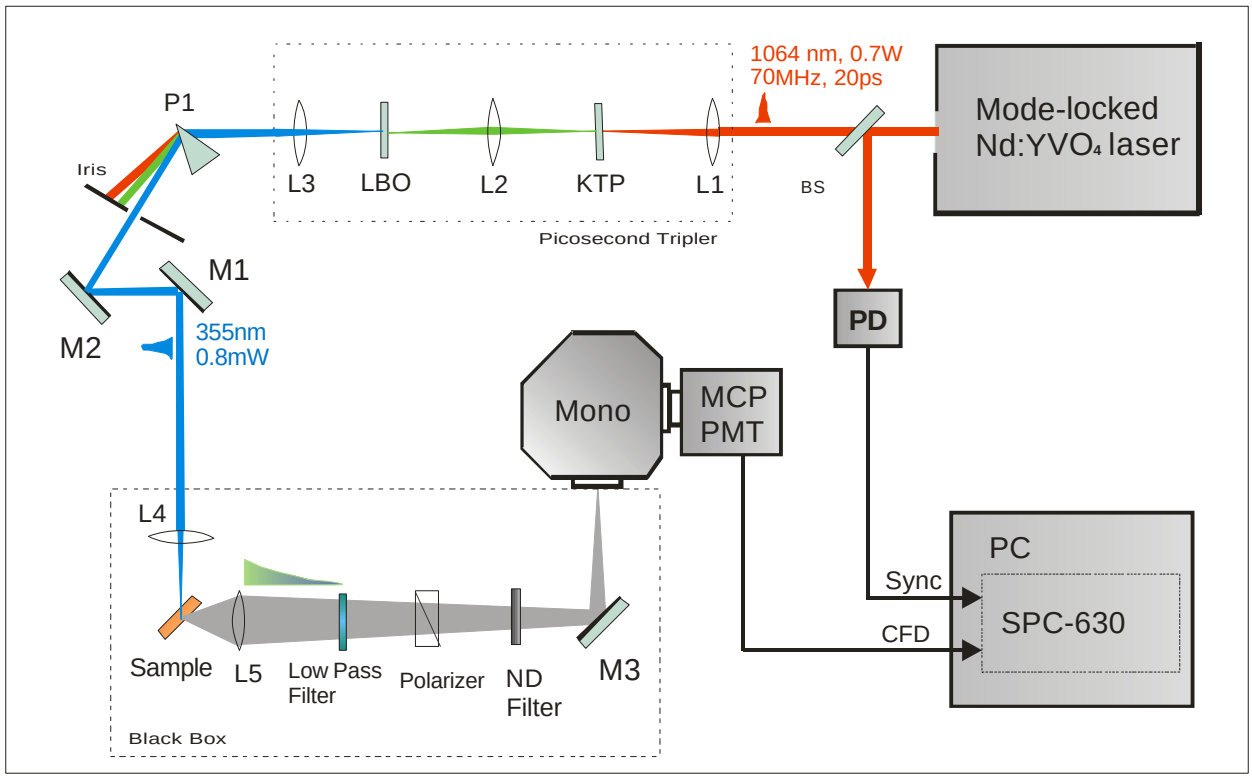

Figure 2.13. *Schematic setup of the picosecond time-resolved fluorescence apparatus. The following abbreviations are used : BS – beamsplitter R=4%; KTP – doubling crystal for 1064nm; LBO – nonlinear LBO third harmonic generation; P1 – fused silica prism for wavelength separation, L1 – L5 – fused silica lenses; M1,M2,M3 – flat aluminum mirrors; Mono – single grating monochromator; MCP – micro channel plate; PMT - photomultiplier; CFD – constant fraction discriminator input of the SPC630 photon counting board; PD – photodiode for time synchronization; Sync – synchronization input; PC – control and data acquisition computer.*

birefringence and the resulting polarization of the went-through 1064nm beam is linear and vertical as well as the polarization of the generated second harmonic at 532nm. The third harmonic output power is measured to be around 0.8 mW. After passing the separation prism P1 the 355nm beam is reflected by steering mirrors, M1 and M2 and is focused in the sample cell by the lens L4 (f=150mm). The cell has an optical path 2mm and is tilted by 45° in respect of the excitation beam to minimize the parasitic pump reflections from the cell walls.

The lens L4 is used to collect the fluorescence in solid angle of 1.3sr and to focus it into the entrance slit of a grating monochromator (Oriel MS125, 12.5cm). Suppression of the residual scattered pump light is achieved using Schott WG400 low pass filter. A Glan-Taylor polarizer is set to the 'magic angle' 54.7° in order to prevent the signal contributions from the polarization reorientation. The fluorescence intensity is adjusted varying the optical transmission of a neutral-density (ND) filter. The spectrally separated (12nm FWHM) photon flux passes through the monochromator and is detected by microchannel plate and photomultiplier head (Hammamatsu R3809U-50).

The signals are processed by a single photon counting PCI module (SPC-630, Becker-Hickl). The time-correlated single photon counting technique is based upon measuring the time between the excitation of the sample and the consecutive emission of a single photon. The fluorescence signal is attenuated so that physically only one photon per around 10^3-10^4 excitation pulses is detected. Accumulation of a manifold of such measurements yields a histogram depicting the time dependence of the fluorescence of the sample.

The IRF of the described fluorescence spectrometer is characterized by measuring the time profile of the scattered excitation pulses from a 2-mm optical cell filled with non-fluorescent scattering medium (e.g. milk), conserving the same excitation and detection geometry. The instrumental response has a full width at half maximum of 39.6±0.5ps (Fig. 2.14). The time window of the measurement is limited by the laser pulse repetition rate (70MHz) and is 14.2ns.

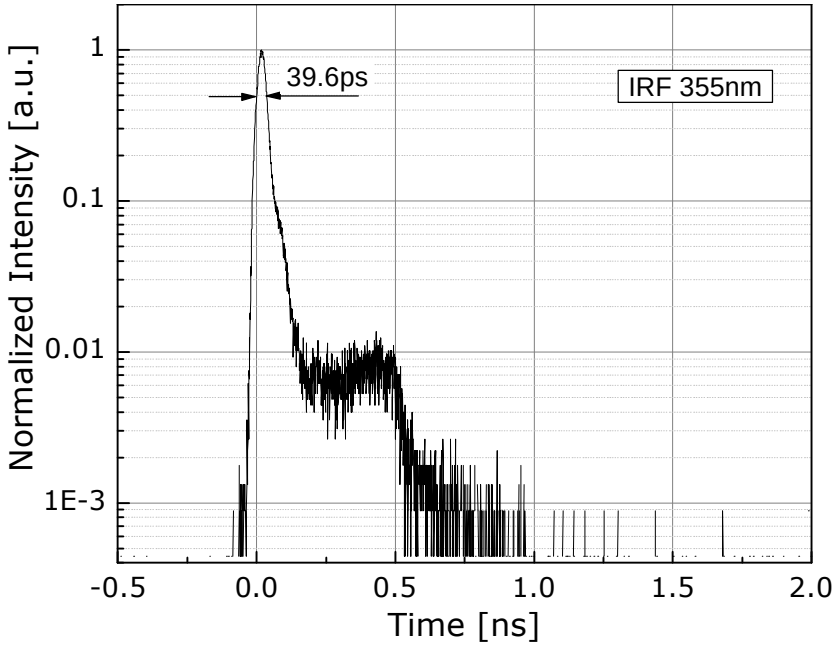

Figure 2.14. *Instrumental response function of the TCSPC fluorescence setup at excitation wavelength 355nm.*

2.3. Equipment and methods for steady-state absorption and fluorescence measurements

All the solvents for the measurements were Uvasol grade (Merck) and were used without further purification. The transient absorption experiments were carried out using sample cells with optical path lengths of 1 mm and 1.25 mm thick fused silica windows. For the steady-state measurements 10 mm cells were used. Steady-state fluorescence spectra were obtained with a Jobin-Yvon Fluoromax-3 fluorimeter. The spectra are intensity corrected. The absorption spectra are recorded with a Varian Cary 50 spectrometer.

To exclude a possible degradation of the samples during the measurement, steady-state absorption and fluorescence spectra of the samples were measured before and after the time-resolved experiments. In all the solutions used in the following chapters no indications of degradation were found.

3. Ultrafast photoinduced processes in DNA

3.1. Hydrogen-bond-assisted electron transfer to a DNA base

3.1.1. Background

The interplay between electron transfer (ET) and proton transfer (PT) remains a subject of lively scientific debates, especially in biological systems [30-41]. In particular DNA represents a unique supramolecular medium for PT and ET processes because the base pairs are structurally coupled in a Watson-Crick arrangement. Understanding the role that hydrogen-bond structures can play in driving electronic charges through the base stack is therefore critical.

In this chapter, a spectroscopic investigation of the ET dynamics in the model nucleoside 5- pyrenyl-2'-deoxyuridine (**PydU**) is presented. Pyrene derivatives have been used previously as artificial DNA bases by Kool et al. [42] Herein the different approach is used and the pyrenyl group is attached covalently to the 2'-deoxyuridine nucleobase [43, 44] as shown in Figure 3.1(a). The radical anion of thymidine (which is structurally very similar to uridine) and cytidine have been proposed as major intermediate charge carriers during electron transport in DNA [45]. The recent reports on the photophysics of **PydU** (and its cytidine analogue) both in DNA [41, 46] and in aqueous solutions [37, 39, 40] demonstrate the significance of protonation concomitant to the reduction of dT and dC. Although these results have relevant implications for electron migration through DNA they have been obtained in water which has a polarity not typical for the inner part of DNA, and under non-physiological pH conditions.

First, we present our femtosecond data of **PydU** in methanol (MeOH) and acetonitrile (MeCN), typical solvents *without* (MeCN) and *with* hydrogen bonding capabilities (MeOH). By comparing the ET dynamics in these solvents one can address the specific role of a proton donating and accepting medium on the ET process (as found in Watson-Crick base pairs). In

1995, Netzel *et al.* studied the steady state fluorescence and nanosecond fluorescence lifetime of **PydU** in MeOH and MeCN [44]. It was proposed that ET from **Py*** to **dU** should be more favorable in MeOH than in MeCN because of a proton-coupled electron transfer (PCET) process.

Combining the electrochemical potentials E($\mathbf{Py}^{\bullet+}$/**Py**) = 1.5 V [47] and E(**dT**/$\mathbf{dT}^{\bullet-}$) = -1.8 V (vs. NHE) [48], the driving force ΔG for the ET process in **PydU** is ~ 0.05 eV (using E_{00}=3.25 eV for **Py*** [47]) – if Coulombic stabilization is neglected. Netzel *et al.* concluded that the formation of $\mathbf{Py}^{\bullet+}\mathbf{dU(H)}^{\bullet}$ is thermodynamically exergonic whereas the formation of $\mathbf{Py}^{\bullet+}\mathbf{dU}^{\bullet-}$ is endergonic. Consequently, in MeCN no ET reaction would be possible. We have applied femtosecond broadband pump-probe spectroscopy to illuminate the early time excited state dynamics in **PydU** after optical pumping in both MeOH and MeCN.

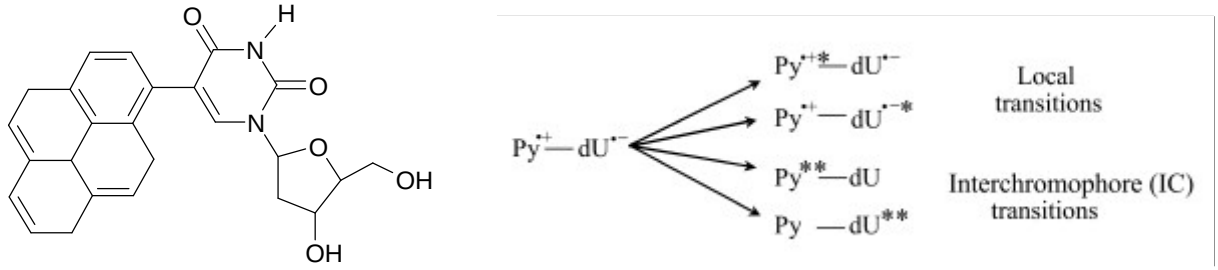

PydU

(a) **(b)**

Figure 3.1. *(a) Structure formula of **PydU**; (b) summary of the transitions represented in transient absorption spectra of **PydU**.*

After photoexcitation **PydU** undergoes an intramolecular ET which results in the formation of the contact ion pair (CIP) $\mathbf{Py}^{\bullet+}\mathbf{-dU}^{\bullet-}$. There are two categories of electronic transitions (as shown on Figure 3.1b) that can be observed in transient absorption spectra of strongly coupled contact ion pairs [49, 50]:

i) Local radical absorption bands are most commonly discussed when transient absorption spectroscopy is applied to charge transfer systems. The bands are usually very similar to those observed in separated $\mathbf{Py}^{\bullet+}$ or $\mathbf{dU}^{\bullet-}$ reference systems and therefore straightforward to interpret.

ii) The interchromophore (IC) transitions in Figure 3.1 (b) are reverse charge-transfer (RCT) transitions which lead to nonpolar, locally excited states. RCT absorption is analogous to exciplex emission since both processes involve charge recombination. Their intensities are largely dependent on the electronic coupling between **Py** and **dU** and should therefore reflect nuclear motions and structural changes that alter this coupling. The temporal evolution of RCT absorption bands can be regarded as a pendant to time-resolved emission spectra.

3.1.2. Femtosecond pump-probe data

Figure 3.2 reveals the different characteristics of local and IC bands for **PydU** by showing the pump-probe spectra of **PydU** in three different solvents, 20ps after photoexcitation. The band around 380 nm (Figure 3.2 inset) which reflects the absorption of the initially excited pyrenyl state (**Py***)[51] and the bands between 450 and 510 nm (local pyrenyl bands, $\mathbf{Py}^{\bullet+}$/**Py***) are virtually solvent independent because the underlying transitions

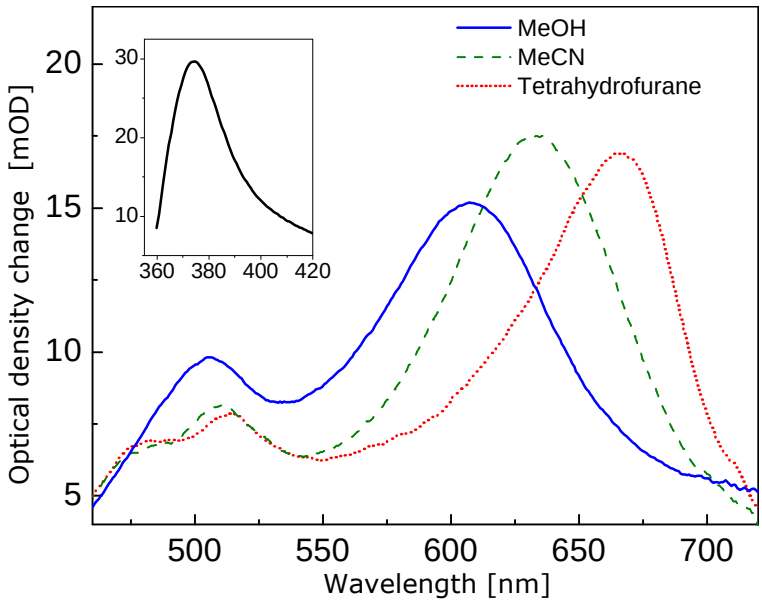

Figure 3.2. *Pump-probe spectra of **PydU** in three different solvents, 20 ps after excitation at 345 nm. One can clearly distinguish the solvent-independent (local) pyrenyl transitions and the strongly solvent-dependent CIP state absorption bands (reverse charge transfer). The inset shows the characteristic **Py*** absorption band around 375nm.*

are not accompanied by changes in the molecular dipole moments. In contrast, the broad (RCT) absorption band between 600 and 670 nm is strongly solvent dependent. This band exhibits a solvatochromic shift towards shorter wavelengths with increasing solvent polarity. On the other hand, the intensity of the IC band depends on the magnitude of the electronic coupling between the two aromatic subsystems and therefore on the conformation of **PydU**. A rise in the intensity suggests the transition from a twisted to a more planar geometry with enhanced π-electron overlap between **Py** and **dU** [52].

In MeOH the single-wavelength kinetics (Figure 3.3) indicate that the initial **Py*** population (~375 nm) decays with a 35 ps time component which matches the rise time of the $\mathbf{Py}^{\bullet+}$ absorption at 505 nm. The fact that the ET product ($\mathbf{Py}^{\bullet+}$) is rising on the same time scale as the IC band (Fig. 3.3) clearly indicates that the ET process is coupled to a structural change in the molecule. In other words, while the molecule is moving towards a more planar geometry, more charge is transferred from **Py*** to **dU**. In MeCN, on the other hand, it can be

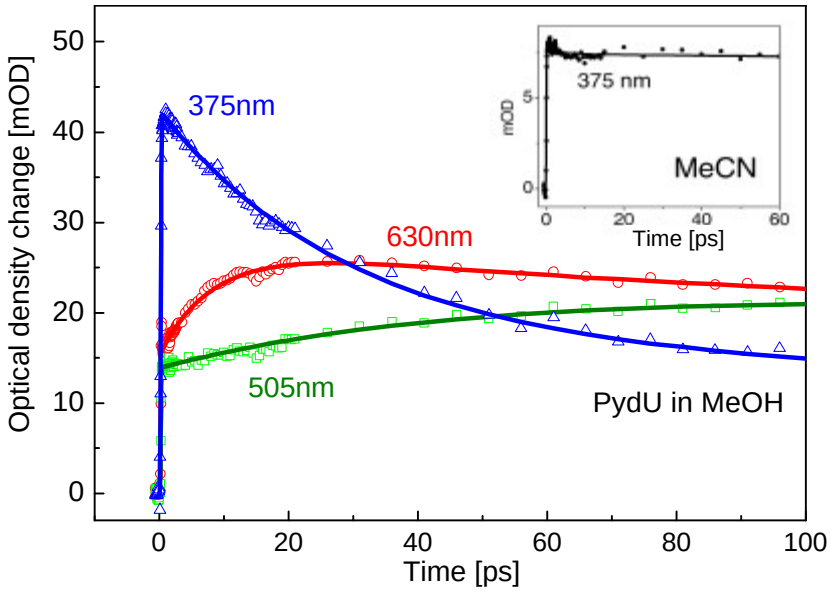

Figure 3.3. *Time-dependent transient absorption signals of **PydU** in MeOH at three selected wavelengths. The decay time at 375 nm (35 ps, 63%) matches the rise time of the $\mathbf{Py}^{\bullet+}$ absorption at 505 nm. The rise time of the IC band (7 ps at 630 nm) is convoluted with the spectral shifting dynamics. Inset: **PydU** in MeCN. The population decay of **Py*** probed at 375 nm. The short decay component (~ 4 ps) represents the ET equilibration dynamics.*

observed a fast equilibration between **Py*** and $\mathbf{Py}^{\bullet+}$ on the time scale of a few ps which is typical for electron donor (D) / acceptor (A) systems with small driving forces where the ET is incomplete. The inset of Figure 3.3 clearly shows the biexponential decay of the **Py*** population (probed at 375 nm) where the fast component (~4 ps) characterizes the equilibration dynamics. Subsequently, the molecule undergoes a similar structural relaxation as observed in MeOH, indicated by the rise of the IC band around 630 nm.

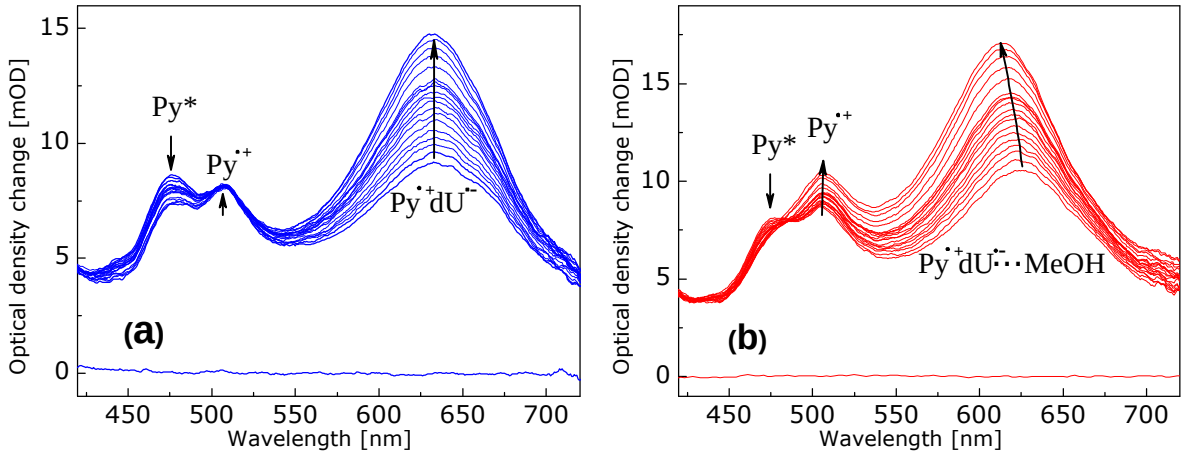

Figure 3.4. *Time-dependent evolution of the pump-probe spectrum of* ***PydU*** *in (a) MeCN and (b) MeOH between 3 and 20 ps after excitation. The arrows show the time evolution of corresponding peak maxima. The time difference between each spectrum is 1 ps.*

In contrast to the MeOH data, however, the IC band in MeCN is not exhibiting a blue shift (Figure 3.4 (a)). The absence of the spectral shift in MeCN indicates that the shift originates from MeOH-specific solute-solvent interactions. These interactions are likely caused by the hydrogen-bond network, particularly the H-bonds between MeOH and $\mathbf{dU/dU}^{\bullet-}$. However, the protonation of $\mathbf{dU}^{\bullet-}$ by MeOH should be thermodynamically unfavorable. This conclusion is based on the pK_a value of 6.9 which was determined by Steenken *et al.* for the protonated thymidine radical $\mathbf{dT(H)}^{\bullet}$ which thus represents a stronger acid than MeOH (pK_a 15.7).[53] Based on the difference in pK_a values one would expect a rate constant for $\mathbf{dU}^{\bullet-}$ protonation in the order of milliseconds, i.e. several orders of magnitude slower than the lifetime of the CIP state [54]. Instead of PCET more relevant is a hydrogen bond-assisted ET mechanism where

hydrogen bonding facilitates the transfer of electronic charge from **Py*** to **dU**. While protons will certainly be "re-adjusted" within the hydrogen bond network there should not be a kinetically distinguishable $\mathbf{Py^{\bullet+}dU(H)^{\bullet}}$ species based on thermodynamic arguments.

In MeCN, on the other hand, one observes a fast equilibration between **Py*** and $\mathbf{Py^{\bullet+}}$ on the time scale of a few ps which is typical for electron D/A systems with small driving forces where the ET is incomplete (Figure 3.4 (a)). Subsequent to ET the molecule is undergoing a similar structural relaxation as observed in MeOH, indicated by the rise of the IC band around 630 nm.

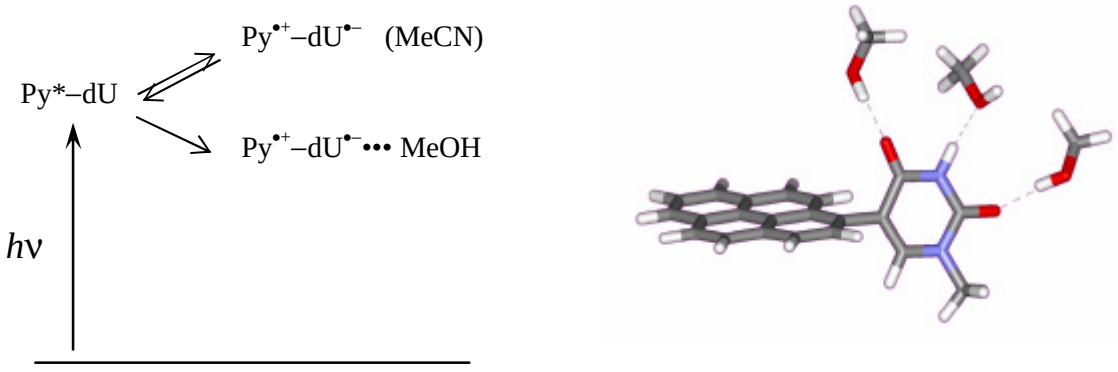

(a) **(b)**

Figure 3.5. *(a) Schematic of excited state interactions between **PydU** and MeOH/MeCN (b) Molecular model to illustrate hydrogen bond interactions between **PydU** and MeOH. The structure is optimized using the PM3 hamiltonian.*

The results presented in this section demonstrate the relevance of a proton donating/accepting environment for ET dynamics, especially in the small driving force regime. Even if protonation/deprotonation of the ionic intermediates is thermodynamically not feasible, the hydrogen-bonding interactions are capable of driving the ET to a specific site. Such hydrogen-bond-assisted ET mechanisms are likely to play a vital role in many biological ET reactions where ΔG is often very small.

3.2. Structural inhomogeneity and electron transfer dynamics in DNA

3.2.1. Background

Reductive electron-transfer (ET) processes in DNA have attracted considerable interest over the last 2–3 years.[55] The injection of an excess electron into DNA initiates a type of charge transfer which is complementary to the extensively studied oxidative hole transfer. [55, 56] Recent studies [39, 45, 46, 55, 57-62] support the idea that the reductive type of charge transfer has a high potential for application in new nanodevices based on DNA or DNA-inspired architectures.

Until five years ago, most knowledge about excess electrons in DNA came from g -pulse radiolysis studies.[57] However recent photochemical assays focus on the investigation of ET by chemical means:

1) Carell et al. could show that the amount of T–T dimer cleavage depends rather weakly on the distance to the electron donor. [58]

2) Giese et al. could show that a single injected electron can cleave more than one T–T dimer.[59]

3) Rokita et al. detected a significant base-sequence dependence of the ET efficiency.[60]

To date, only a few groups [46, 61] have focused on the dynamics of ET processes. In refs. [46, 55, 57-61] a thermally activated electron hopping mechanism has been suggested with $\mathbf{C}^{\bullet-}$ and $\mathbf{T}^{\bullet-}$ as intermediates.[45]However, we could show that proton transfer interferes with ET indicating that $\mathbf{T}^{\bullet-}$ is more likely to play a major role as an electron carrier rather than $\mathbf{C}^{\bullet-}$.[39, 62]

Over the last years it has become apparent that ET phenomena in DNA cannot be understood without explicitly considering the manifold of conformational states present in DNA. [63-67] Since ET rates strongly depend on the microscopic environment, a single kinetic rate constant might not be observed for DNA-mediated ET but rather a distribution of rates.

In this chapter we present a study of the mechanism of electron injection and subsequent interbase electron shift by ultrafast time-resolved measurements using 5-bromo-2'-deoxyuridine (**Br-dU**) as the electron acceptor.[68-71] Pyren-1-yl-2'-deoxyuridine (**PydU**)[43] has been applied as the electron donor, since photoexcited **Py*** allows the reduction of **C** and **T**.[47, 72] The synthesized [46, 73] and investigated **PydU**-modified DNA duplexes **PU1** and **PU2** are shown in Figure 3.6a).

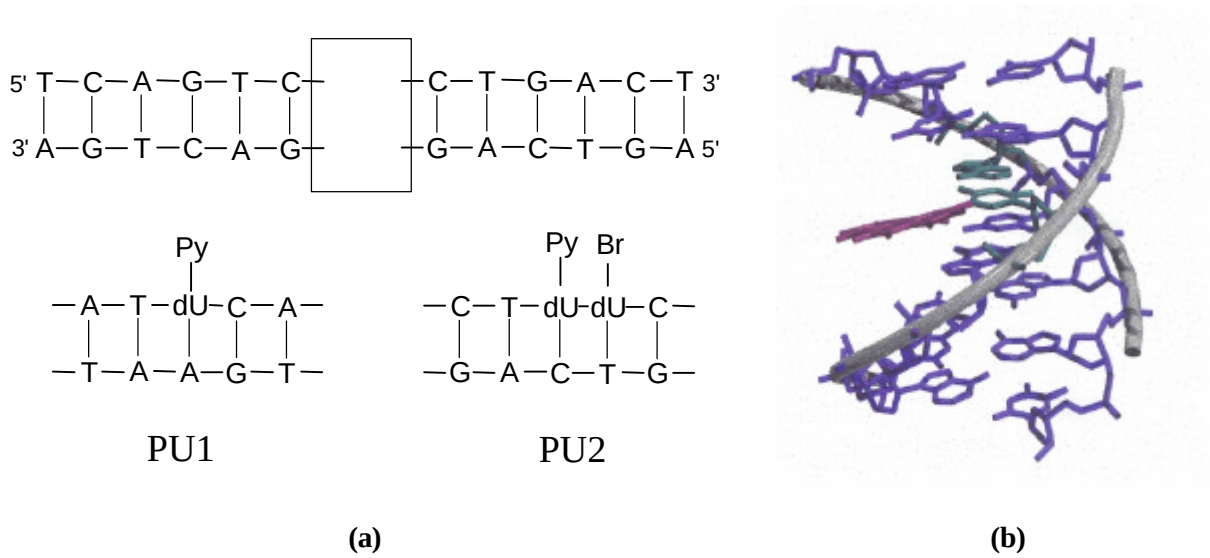

Figure 3.6. *(a) Pyrene-modified DNA duplexes PU1 and PU2; (b) force field (AMBER) minimized structure of a PydU-modified DNA duplex.*

The **PU1** is a control duplex containing only the **PydU** chromophore with adjacent **C** and **T** bases as acceptors for the subsequent electron transfer from $\mathbf{dU}^{\bullet-}$. The DNA duplex PU2 contains additionally the **Br-dU** group which is placed adjacent to **PydU.**

3.2.2. Experimental results and discussions

The femtosecond broadband pump-probe spectroscopy is applied to explore the early time ET dynamics in **PU1** and **PU2** within a broad spectral probing window and the temporal evolution of the pump-probe spectra of **PU1** is shown in Figure 3.7. Immediately after excitation at 350 nm a pyrene-like excited state (**PydU**)* is formed which undergoes ET yielding the

contact ion pair (CIP) $\mathbf{Py}^{\bullet+}$–$\mathbf{dU}^{\bullet-}$. Since the ET process formally represents the injection of an electron into the base stack, the injection rate can be obtained from the decay of the transient absorption band of (**PydU**)* at 385 nm.[40] In the CIP state the radical cation ($\mathbf{Py}^{\bullet+}$) and the radical anion ($\mathbf{dU}^{\bullet-}$) are electronically coupled (as a result of a direct p-orbital overlap) and thus exhibit strong spectral features which extend from around 450 to approximately 750 nm.

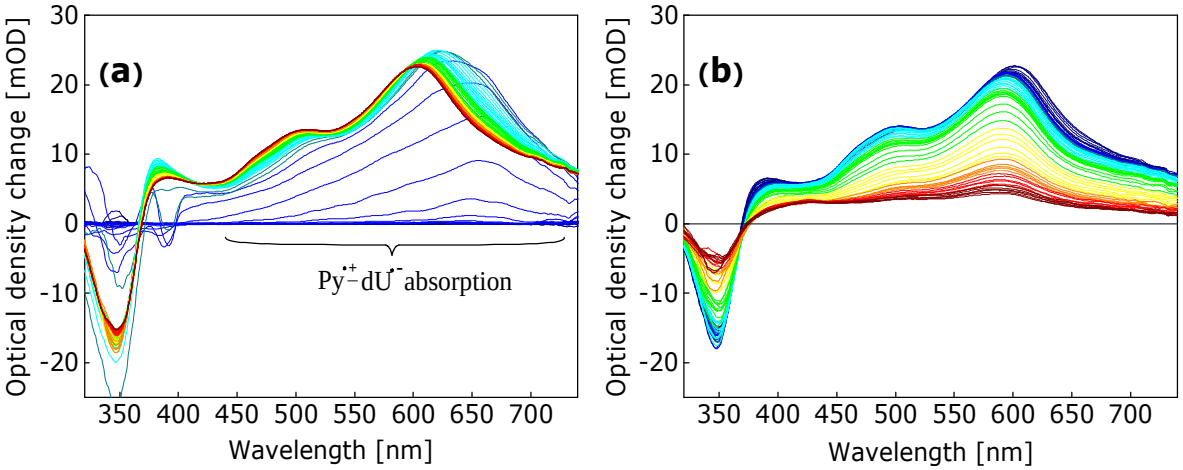

Figure 3.7. *Temporal evolution of the pump-probe spectra of* ***PU1*** *after photo excitation with a femtosecond pulse at 350 nm in two different time ranges: (a) -0.6 – 3 ps, (b) 3 ps - 1400 ps. Spectra at early times are shown in blue, evolving through green, yellow to red/dark red (late time spectra).*

While the rise time of the transient absorption signals in this spectral region is about 2–3 ps (for all five DNA duplexes) the decay times vary in a very broad range depending on the probe wavelength. To obtain more mechanistic insight the time-dependent pump-probe-signal $S_l(t)$ between 350 and 700 nm is analyzed by fitting with three exponential terms functions (Eq. (1)) as described in details in paragraph 2.1.6. The parameters (c_i, t_i , i=0..3 in Eq.(2)) are evaluated by a least-square fitting.

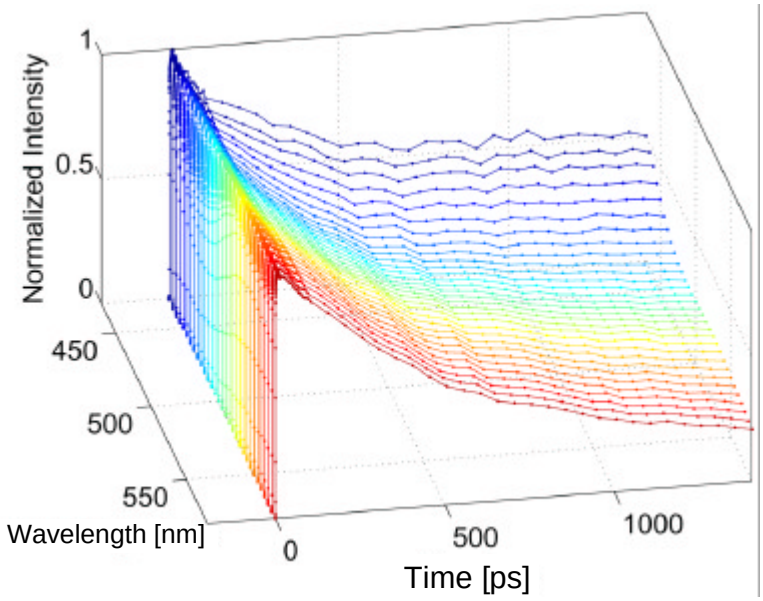

Figure 3.8. *Normalized time-dependent pump-probe signals of PU1 between 450 and 580 nm.*

Figure 3.8 displays the kinetic profiles in the spectral region between 435 and 580 nm. The multi-exponential nature of the signal in this spectral region can be clearly observed. The fastest time component t_1 has been found to be in the range of 1.5 to 8 ps (depending on the probe wavelength as shown on Figure 3.9(a)) and the slow component was fixed at 3 ns. The intermediate time component t_2 varied between 120 and 540 ps (Fig. 3.9 (b)) thereby showing pronounced probe wavelength dependence. The fast decay component t_1 has a large amplitude (c_1) between 570 and 700 nm - the region in which the pronounced spectral blue shift occurs at early time. Since the maximum of the broad band is ~590 nm (after the spectral shift is completed) one observes positive values for c_1 (indicating a decay) for l > 590 nm and negative values (indicating a rise) for l < 590 nm.

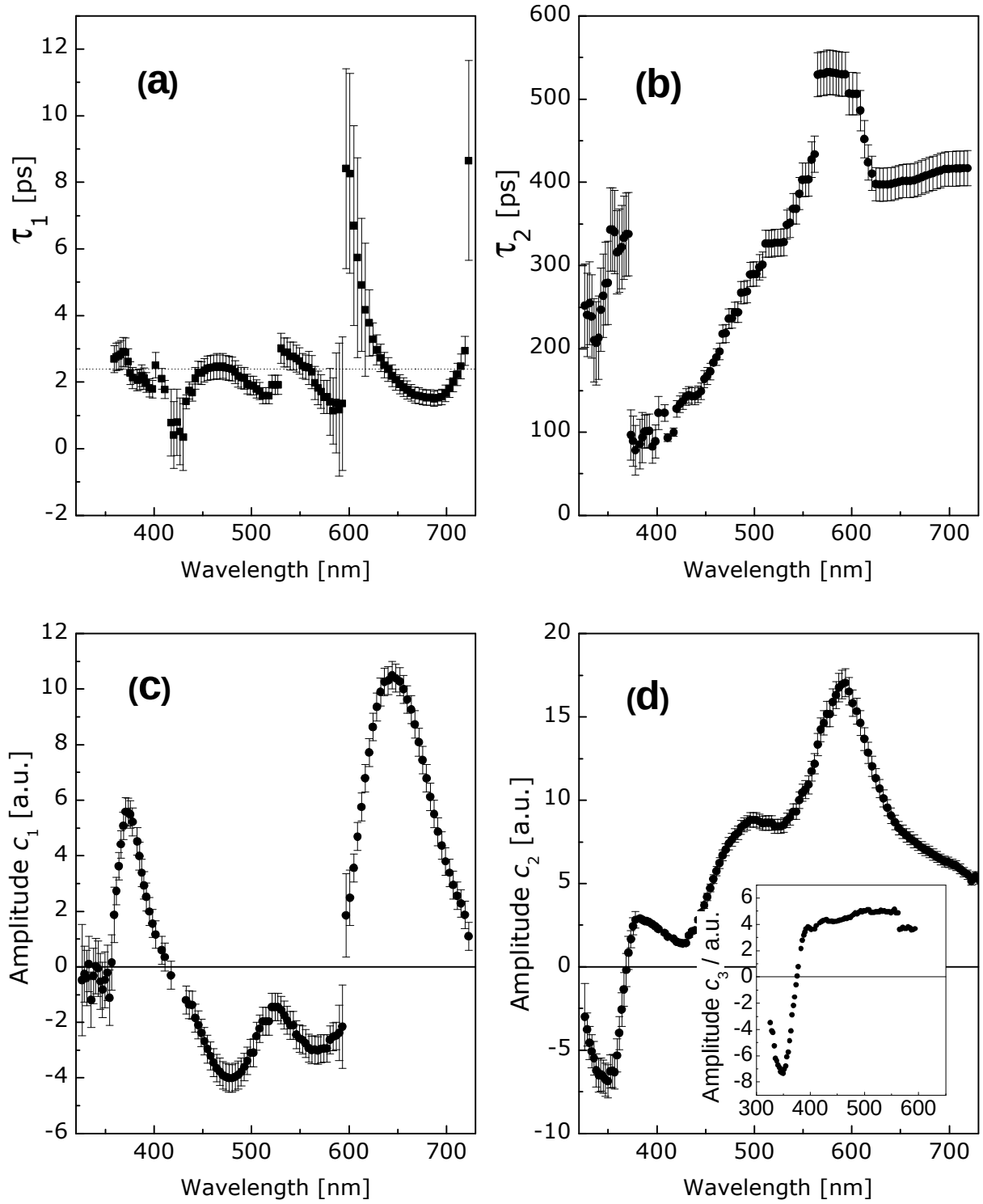

Figure 3.9. ***PU1*** *transient time components and corresponding amplitudes (as obtained from the kinetic analysis) as a function of the probe wavelength. The error bars have been estimated on the basis of least-square fitting results.*

Furthermore, it is interesting to note that t_1 is strongly pronounced around 480 nm (negative peak of c_1). This wavelengths corresponds to the absorption band of the pyrene radical cation (**Py**$^{\bullet+}$). Towards shorter wavelength, c_1 is changing its sign and reaches another maximum around 390 nm (absorption maximum of **Py***), thereby providing direct proof that the initial charge injection occurs with the rate constant t_1. Hence, based on the kinetic analysis which reveals the spectroscopic signatures of **Py**$^{\bullet+}$ and **Py*** in the spectral dependence of c_1 can be concluded that the initial ET takes place in 2.4 ps (dotted horizontal line in Figure 3.9(a)). Figure 3.9 (d) shows the spectral dependence of c_2 indicating that the picosecond component t_2 is clearly present over the entire spectral range. The exact value of the nanosecond component t_3 could not be determined accurately because it is outside of the experimental probing window (up to 1.5 ns). The amplitude $\boldsymbol{c_3}$ is nearly constant between 600 and 400 nm and follows the intensity of the pump-probe spectrum below 400nm (Fig. 3.9 (d) inset).

The initially excited state (**PydU**)* has a broad absorption band between 600 and 700 nm which – upon charge separation – undergoes an ultrafast blue shift, analogue to the well-known dynamical Stokes shift in time-resolved fluorescence experiments. Thus, the process of charge injection into the base stack exhibits great similarity with the classical solvation dynamics in polar solvents. DNA acts as a polar solvent which "responds" to changes in the electron density within the stack by structural adjustments. At the same time, structural fluctuations are "driving" the electron from the donor into the base stack. After ET is completed there are a vast number of states characterized by a broad dispersion of electronic and structural properties. The electronic diversity originates from various degrees of electron transfer within the substates. The thermodynamic driving force for ET in (**PydU**)* is weak ($\Delta G \approx$ -0.1eV) [40] and thus complete ET can only be achieved if the contact ion pair **Py**$^{\bullet+}$**-dU**$^{\bullet-}$ is energetically stabilized by the surrounding DNA environment. Given the manifold of conformational substates prior to photo excitation, the initial conditions for medium-driven

ET exhibit a vast dispersion of energies for the chromophore (**PydU**) which becomes visible when broadband probing techniques are applied. Consequently, one does not observe a single kinetic rate constants for the electron injection but rather a distribution of individual rate constants.

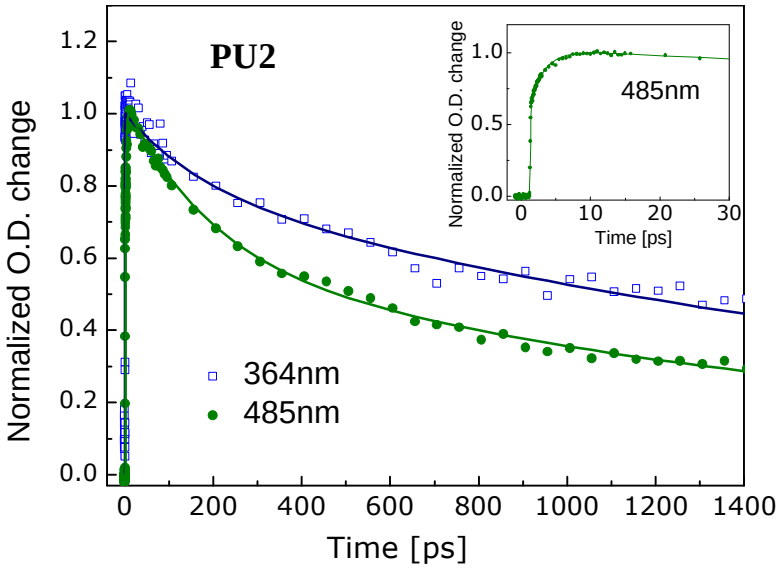

Figure 3.10. *Pump-probe transients of **PU2** at two different probe wavelengths. The ground-state recovery signal at 364 nm (hollow squares) is negative but is inverted to be visually comparable to the (positive) transient absorption of the CIP state at 485 nm (filled circles). The inset displays the 3 ps rise of the 485 nm transient which marks the rate for electron injection.*

To see whether subsequent ET into the base stack competes with charge recombination in the CIP state the repopulation dynamics of the **PydU** ground state was measured. The observed dynamics are very similar in both duplexes, **PU1** and **PU2**. As shown for **PU2** (Figure 3.10), the recovery dynamics of the ground state (530 ps (64%), >2 ns (36%) at 364 nm) does not match the lifetime of the electron injected CIP state (250 ps (55%), >2 ns (45%); rise time 3 ps at 485 nm) thereby suggesting that an additional decay channel (other than charge recombination!) is present from the CIP state. This result suggests that only a fraction of CIP ensembles returns to the ground state and the remaining CIP populations react through a different channel.

3.2.3. Conclusion

The results presented here underline the inevitable need to include conformational substates and fluctuations in the theoretical description of photoinduced processes in DNA. Simple kinetic schemes with well-determined rate constants do not include the complex structural and dynamical landscape in DNA and can therefore provide only an idealized simplistic view.

Several important conclusions emerge from this study:

1) DNA is a flexible medium with a manifold of conformational states exhibiting a wide range of reactivities and rate constants.

2) As expected, the electron-injection process in our functionalized duplexes show only minor variations arising from structural inhomogeneity because it occurs between the covalently connected **Py** and **dU** moieties. Subsequent ET into the base stack is much more sensitive to structural parameters and thereby characterized by a distribution of time rates.

3) It is important to probe both the early time events and the product states for obtaining conclusive mechanistic insight. Since DNA-mediated ET is a multistep process on various time scales, the electron-injection rates may not necessarily correlate with the strand degradation as the chemical result of DNA-mediated ET.

4) The subsequent ET in the base stack occurs on the time scale of several hundred picoseconds, therefore competing with charge recombination in the studied duplexes. It is reasonable to assume that subsequent migration steps will be faster since the Coulomb interaction between the excess electron and $\mathbf{Py}^{\bullet+}$ decreases drastically with separation. Hence, the current results provide a lower limit for the rate of reductive ET between single bases in DNA.

3.3. Local dynamics and flexibility of DNA on the picosecond time scale

3.3.1. Introduction

The results decribed in the previous section show that a proper description of the ET dynamics in DNA must include structural dynamics and inhomogeneity. In the following section a method which allows the probing of local structural DNA dynamics in real-time is presented. Over the last decade the structural [74-84] and electronic [85-91] properties of DNA have been the focus of intense research efforts. DNA is a complex medium with internal dynamics on time scales that span over 15 orders of magnitude (from 10^{-13} s to 10^{2} s).[82, 92] Various techniques have been applied to study DNA dynamics on the time-scales of seconds to milliseconds,[84] nanoseconds and subnanoseconds.[93-95] While slow dynamics are more easily related to biological function, the specific role of local ultrafast motions remains widely unknown. However, their relevance has recently been pointed out in connection with electronic transfer processes, such as oxidative DNA damage.[64, 66]

The experimental methodologies for studying ultrafast conformational changes or reorganization dynamics in DNA are generally based on spectroscopic monitoring of specific chromophores bound to DNA. Berg *et al.* have recently presented an approach [93, 94] which is an analog to the conventional time-resolved experiments for studying solvation dynamics in polar solvents: upon photo excitation a chromophore undergoes an instantaneous change in its permanent electric dipole moment. The polarizibility of the surrounding medium is responding to the change of the dipole moment and the reorientation of the environment can be followed by monitoring the fluorescence Stokes shift as a function of time. From these experiments one can derive an effective polarity of DNA as well as characteristic time scales for reorganization dynamics [93, 94].

In this section we present an alternative approach for measuring ultrafast structural dynamics in DNA. Instead of using a *single* polar CT chromophore which is inserted into the

base stack we utilize *a pair* of interacting chromophores covalently attached to a specific DNA base but located in the major groove. This approach reduces structural perturbations in the base stack which might affect the local dynamics. When the DNA structure and conformation allows that these chromophores get in close contact they can form *excimers* (excited dimers) with characteristic spectral properties.[42, 83, 96-100] Pyrene-labeled oligonucleotides have been employed to probe conformational changes in both RNA and DNA [101-107] and to investigate photoinduced charge transfer between bases in DNA [37, 39, 40, 44, 46, 108, 109] Recently, pairs of ethynylpyrene-labeled bases have been utilized to monitor salt-induced B-Z DNA transitions by steady state spectroscopy.[104]

Previous studies on pyrene directly linked to nucleotides in the base stack revealed evidence for ultrafast electron transfer (with uracil (**dU**) and cytidine (**dC**)) and hole transfer with guanine.[39] However, the free energies for these processes have been estimated to be only around -0.1 to -0.3 eV.[40] Although, an acetylene bridge is a strong mediator for electronic coupling between chromophores, [110-113] the additional separation between **Py** and **dU** should inhibit a complete electron transfer.

The **Py**-≡-**dU**-modified oligonucleotides studied in the current chapter are shown in Figure 3.11. They were synthesized in the group of Dr. Achim Wagenknecht (TUM) by using a semi-automated synthetic strategy using Sonogashira-type cross-coupling conditions on solid-phase [114]. The 1-ethynylpyrene (**Py**-≡-) moiety is covalently attached to the 5-position of Uridine and replaces the methyl group of naturally occurring thymidines and it is expected to be located in the major groove.[115, 116] This assumption is based on similar modifications which revealed that such ethynyl substitutions have only little influence on the stability of the resulting modified DNA duplexes and do not perturb the Watson-Crick base pairing ability.[117, 118]

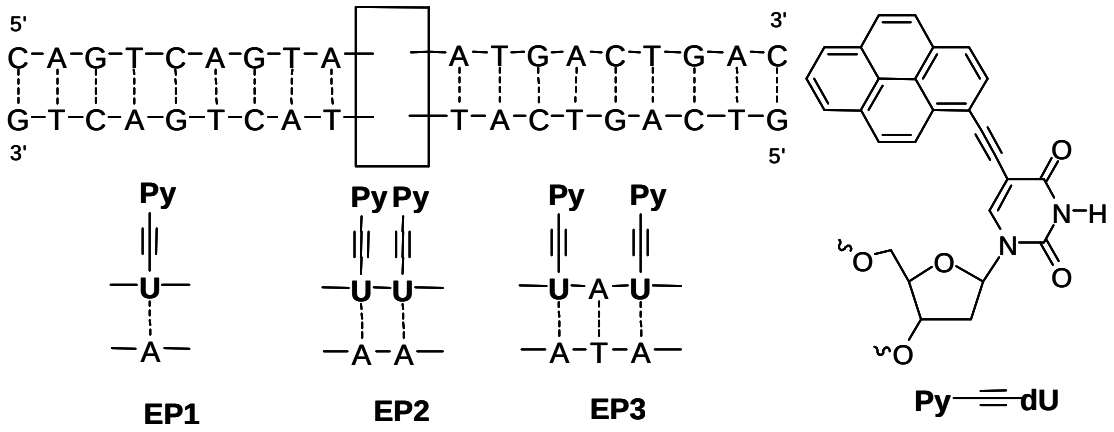

Figure 3.11. *Py-°-dU -modified DNA duplexes EP1 – EP3.*

Using this molecular design, the chromophore does not replace a DNA base or a base pair which would result in an artificially constructed local environment of the chromophore inside the DNA. In the current systems, the **Py-≡-** group merely extends the conjugated planar system of the uridine and thus equips it with optically traceable properties.

3.3.2. Steady state absorption and fluorescence data

Figure 3.12 shows the absorption and fluorescence spectra of all three DNA duplexes (**EP1**-**EP3**) together with the ones of **Py-≡-dU** (in MeOH and MeCN) and **Py-≡-H** (in MeCN). The absorption spectra of **Py-≡-dU** (both in DNA and in organic solvents) are substantially different from that of **Py-≡-H**. The apparent red shift of the long-wavelength absorption band in **Py-≡-H** is caused by a strong enhancement of the $S_0 \rightarrow S_1$ transition in **Py-≡-dU** due to intramolecular electronic coupling between **Py** and **dU**. The absorption spectra clearly indicate that electronic structure of **Py-≡-dU** is delocalized. Hence, even though the pyrene moiety is located in the major groove the optical excitation will spread instantly over the entire molecule and thus into the base stack. In turn, the p -stacking interactions affect the pyrenyl absorption bands as indicated by the pronounced red-shift (~ 10 nm) of the duplexes **EP1**-**EP3,**

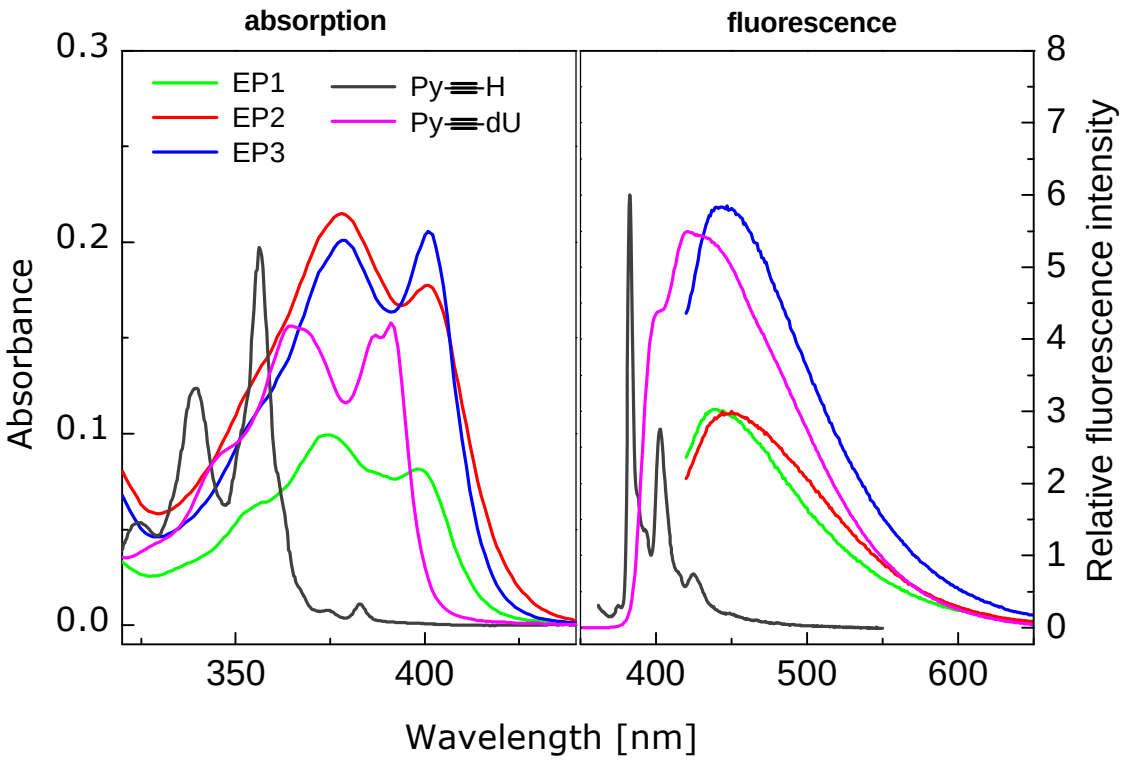

Figure 3.12. *Steady state absorption (left) and fluorescence (right) spectra of EP1 – EP3 along with the spectra of reference systems Py-º-H and Py-º-dU in MeOH .*

with respect to the maxima of **Py-≡-dU** in MeOH and MeCN.

Because of the strong intramolecular coupling the typical pyrenyl-type fluorescence (as observed for **Py-≡-H**) is absent in **Py-≡-dU**. Hence, one cannot expect to find the characteristic redshifted emission, typically observed in pyrene excimers. Instead, the fluorescence spectra of the "dimer" duplexes **EP2** and **EP3** show only a moderate red-shift in their fluorescence spectra.

In addition, all duplexes show a characteristic absorption at ~400 nm due to DNA hybridization [119]. The latter indicates substantial ground state interaction between **Py-º-dU** and adjacent base pairs which are only present in DNA duplexes. The fact, that the 400 nm absorption is not present in oligonucleotides where pyrene is directly linked to **dU** suggests strongly that it originates from specific interactions involving the electronically 'rich' acetylene group rather than the pyrene chromophore itself.

Although **EP2** contains *two* **Py-°-dU** groups, the fluorescence intensity (after excitation at 400 nm) is nearly the same as in **EP1**. This observation indicates that the interaction between **Py-°-dU** and the adjacent base is highly directional and that the concentration of ground state complexes is approximately the same in **EP2** and **EP1**. In **EP3**, both **Py-°-dU** units are flanked by 3' and 5' neighboring bases which allows the formation of twice as many ground state complexes as in **EP1** yielding a two-fold fluorescence intensity compared to **EP1**. Additional evidence for substantial ground state interactions is provided by the excitation wavelength dependence of the fluorescence spectrum of **EP2** (Fig. 3.13).

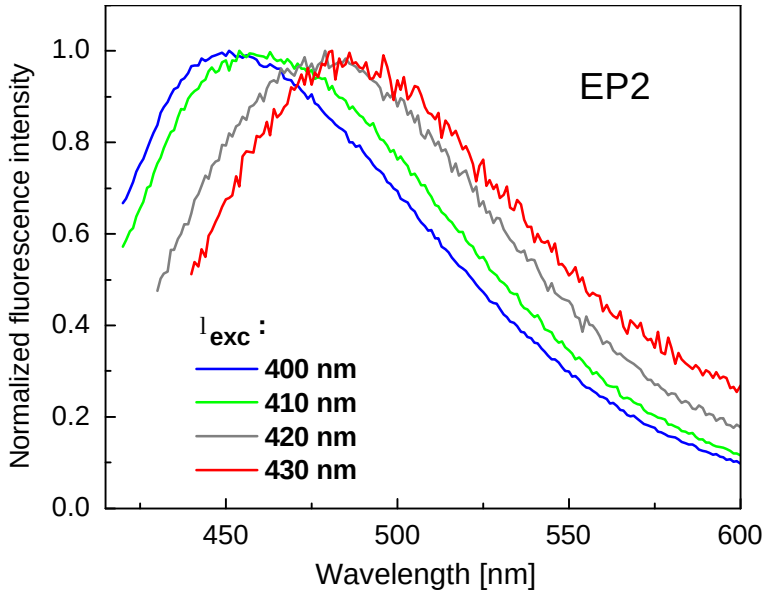

Figure 3.13. *Excitation wavelength dependence of the steady state fluorescence spectrum of* ***EP2***.

Since the focus of the present chapter is not directed towards the ground state interactions between **Py-°-dU** and adjacent bases the excitation wavelength is set to 364 nm, near the maximum of the $S_0 \rightarrow S_1$ absorption of **Py-≡-dU** for the femtosecond pump-probe experiments.

3.3.3. Femtosecond broadband pump-probe results

Figure 3.14 displays the temporal evolution of the pump-probe spectra of **EP1** and **Py-≡-dU** in MeOH within 1 ns after optical excitation. The spectra are dominated by a broad, asymmetric absorption band with a maximum around 700 nm which must be attributed to (**Py-≡-dU**)* absorption. One can observe that **Py-≡-dU** in MeOH and **Py-≡-dU** inserted in the base stack (**EP1**) exhibit very similar spectral dynamics. The onset of relaxation in the excited state

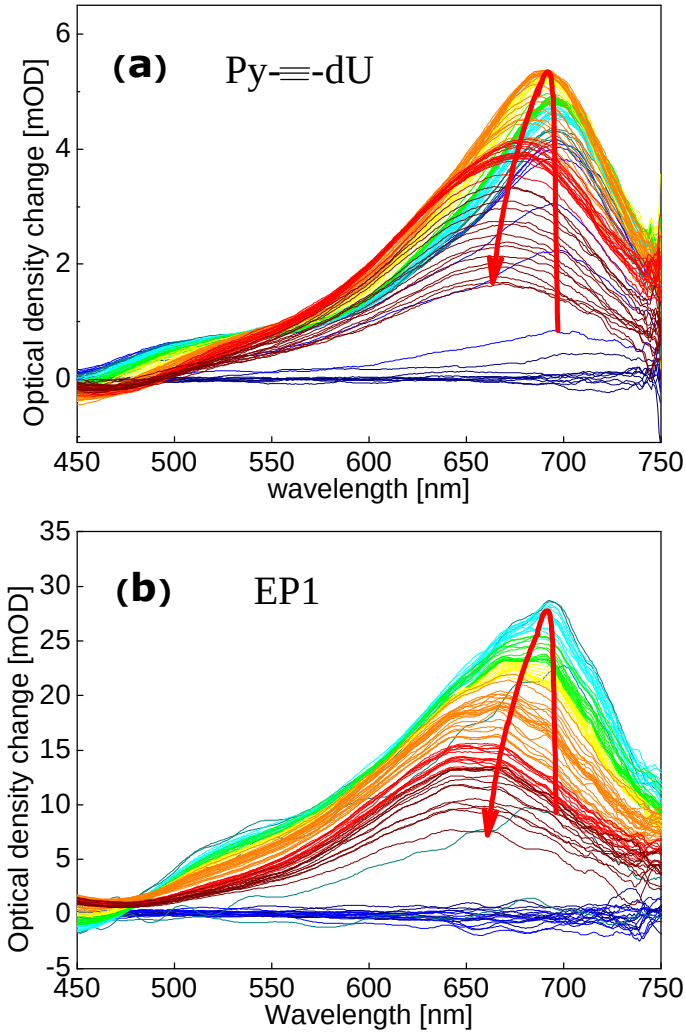

Figure 3.14. *Temporal evolution of the pump-probe spectra of (a)* ***Py-°-dU*** *in MeOH and (b)* ***EP1*** *in the time range between –1 ps and 1 ns after excitation at 364 nm (various step sizes). Early spectra are shown in blue/green and late spectra are shown in red/dark red colors. The arrows trace the time-dependent spectral maxima.*

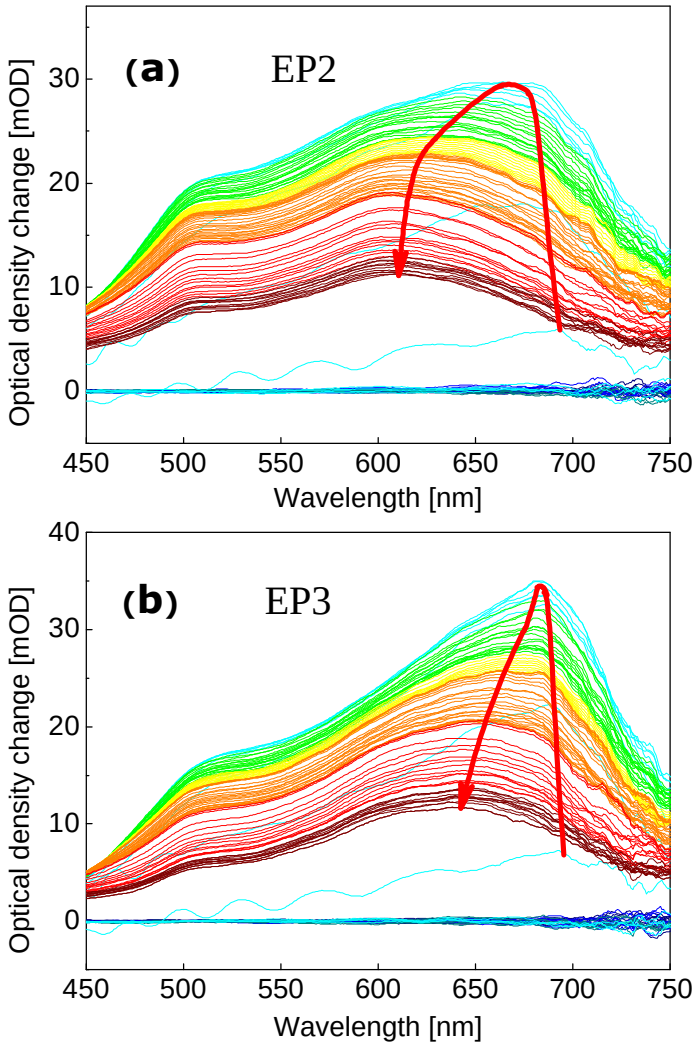

Figure 3.15. *Temporal evolution of the pump-probe spectra of **EP2** (a) and **EP3** (b) in the time range between –1 ps and 1 ns after excitation at 364 nm (various step sizes). Early spectra are shown in blue/green and late spectra are shown in red/dark red colors. The red arrows trace the time-dependent spectral maxima.*

is manifested by a spectral blue shift of the absorption band. The spectral shifting dynamics are continuous, similar to those observed in time-resolved emission studies of CT states in polar solvents.[120, 121] It can be assumed that the latter originates from a solvation process involving rearrangements in the hydrogen bond network. A similar observation has been made for **Py-dU**, where the pyrene and uracil chromophores are directly linked through a covalent bond.[122] The time-resolved pump-probe spectra of the **Py-≡-dU** dimers (**EP2** and **EP3**) in DNA are shown in Figure 3.15. Comparing these spectra with those from the single **Py-≡-dU**

chromophore (Fig. 3.14 (a)) three important differences can be observed: First, an additional absorption band around 500 nm rises within 300 fs. Second, the shifting of the spectral maximum at ~700 nm to shorter wavelengths is more pronounced. Third, the spectra of **EP2** and **EP3** are broader (throughout the entire time range) than the ones of **EP1**.

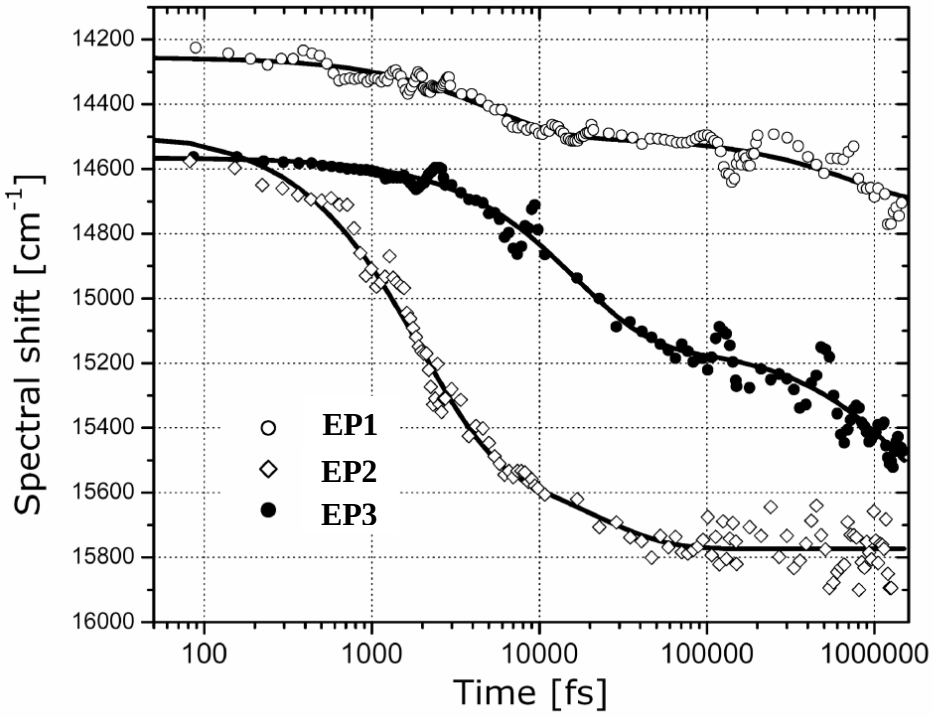

Figure 3.16. *Temporal evolution of the spectral position (in wavenumbers) of the maximum of the IC absorption band for EP1 -EP3.*

	$\Delta\tilde{n}$ (cm^{-1})	t_1 (ps)	t_2 (ps)	A_1 (%)	A_2 (%)
EP1	440	4.6	220	69	31
EP2	1300	1.9	7.6	85	15
EP3	1000	16.4	1860	47	53

Table 3.17.*Biexponetial fit coefficients for the spectral shift of (Py-°-dU)* absorption band maxima in EP1-EP3.*

A quantitative comparison of the spectral shifting dynamics in **EP1** – **EP3** is shown in Figure 3.16 where the spectral position of the maxima of the (**Py-≡-dU**)* absorption band are plotted as a function of time. All peak shift functions have been fitted using biexponentials (Table 3.17). In **EP1**, the (**Py-≡-dU**)* absorption band undergoes a rapid shift with a time constant of 4.6 ps (70%), followed by a slower shift of 220 ps (30%). However, the total magnitude of the shift is only 440 cm^{-1}. In contrast, in **EP2**, the spectral shift is 1300 cm^{-1} with a time constant of ~2 ps for 75%. In **EP3**, one observes almost the same magnitude of spectral shifting (1000 cm^{-1}), however, exhibited on a much longer time scale; approximately 50% of the shift occurs with a 16 ps time constant and 50% on a significantly longer time scale of 1.9 ns.

3.3.4. Discussions

From the temporal evolution of the pump-probe spectra of **EP1**-**EP3** a detailed picture of the spectral and dynamical characteristics of chromophore interactions through DNA bases emerges. The drastic spectral shifts in the broadband excited state absorption spectra of **EP2** and **EP3** (compared to **EP1**) clearly certify dynamic interactions between the two chromophores. The differences in the observed magnitudes of the spectral shifts $\Delta\tilde{n}$ (Table 3.1) suggest that stabilizing chromophore interactions between the two pyrene chromophores are present. It therefore seems reasonable to assume that an excimer-type state is being formed in **EP2** and **EP3.** The (**Py-≡-dU**)* absorption band exhibits a dynamical solvatochromic shift, similar to those observed in time-resolved fluorescence spectroscopy. However, in fluorescence spectroscopy excited state processes (e.g charge transfer) lead to shifts towards longer wavelengths while the opposite behavior (i.e. shifting towards shorter wavelengths) is observed in excited state absorption. In the case of **EP3**, where the pyrene moieties are separated by one intervening **A**-**T** base pair, forming stabilized excimer structure requires

substantial conformational reorganization (Fig. 3.17) involving at least three base pairs, and takes place on the nanosecond time scale. The fact that $\Delta\tilde{n}$ is similar for **EP3** and **EP2** suggests that excimers of similar structure are formed in both duplexes. However, the time scale on which the spectral shift occurs is different. In **EP3**, 50% of the shift takes place with a time constant of 16 ps. The finalization of the shift, however, takes place on a much longer time scale (1.9 ns). In 16 ps, only small structural adjustments of the two chromophores are possible. Since the base-acetylene-pyrene axis is fairly rigid, it is likely that bending motions and partial rotation would have to originate from the base pair. A tightly-bound excimer structure could be achieved by additional local reorganization of the entire duplex. Those 'large-scale' reorientations are likely to take place on the nanosecond time scale.

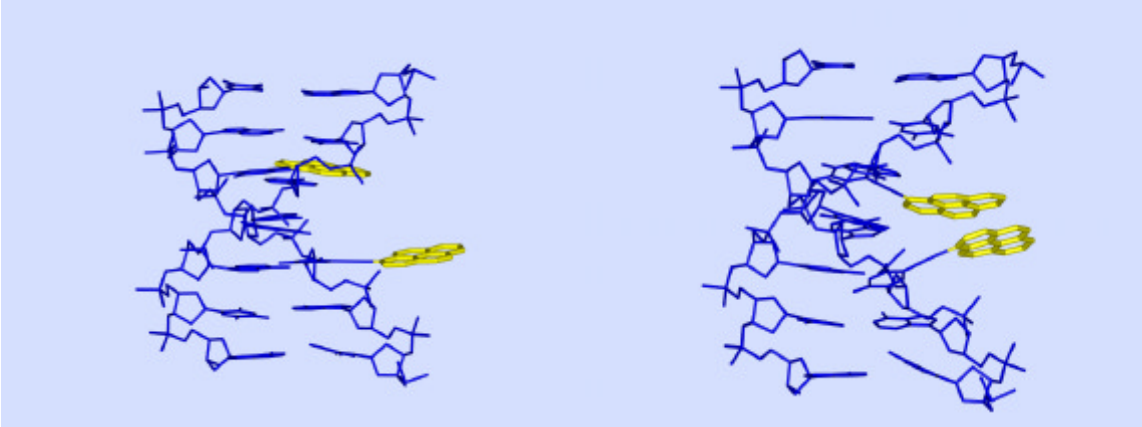

Figure 3.18. *Force field (MM+) optimized structures of **EP3**; equilibrium structure (left) and an 'induced' conformation with strong p-overlap between the two attached pyrene chromophores (right). The structure has been optimized with one negative and one positive charge evenly distributed over the carbon atoms of the two pyrenes.*

Because of the intrinsic asymmetry in the structure of **Py-≡-dU** there are at least two possible relative orientations of the pyrene moieties to be considered. Since both orientations will be present in the ground state, it is expected to have spectral inhomogeneities in the excited state absorption spectrum, and thus broader bands in the case of **EP2** and **EP3** (relative to **EP1**). With one base pair separating the two chromophores, the distance between the pyrene

moieties increases to ~7Å. Moreover, the additional pitch of 36° leads to a vanishing p-overlap in the equilibrium structure (Fig. 3.17, left).

3.3.5. Evidence for ultrafast energy transfer through the base stack

The results shown above clearly indicate the existence of second pathway for excitation energy transfer - *through-base stack* interaction. Since the excitation is delocalized over the **Py-≡-dU** chromophore the optical excitation leads to instant electronic excitation in the base stack. The appearance of the excited state absorption band at 500 nm in both **EP2** and **EP3** (Fig. 3.18 (a)) within 300 fs after optical pumping indicates efficient excitation energy transfer mediated through the intervening **A-T** base pair. The magnitude of the electronic coupling which gives rise to a new absorption band and the ultrafast rate of the process suggests that the energy transfer is mediated through direct p-orbital overlap (as opposed to dipolar Coulomb coupling!).

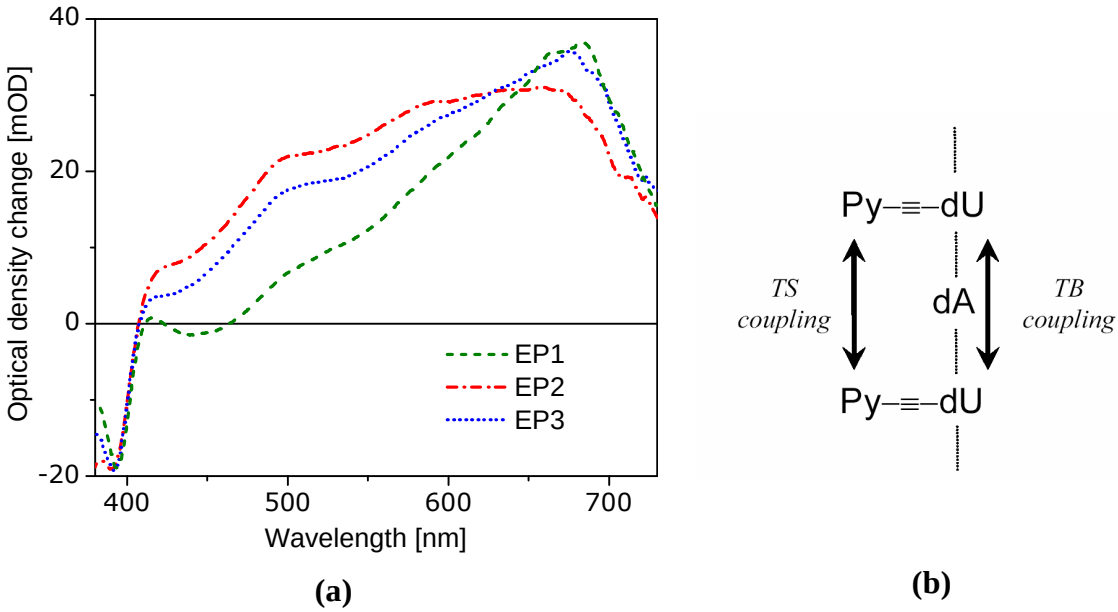

Figure 3.19. *(a) Transient absorption spectra of all three duplexes at delay time 300 fs. (b) Qualitative schematics of the two electronic coupling pathways for excitation energy transfer in EP3 (and EP2): Through-space (TS) and Through-base stack (TB) coupling.*

Finally, it is important to note that both electronic transitions in the dimer systems **EP2** and **EP3** (i.e. the 500 nm and the 700 nm band) must originate from the same excited state since the decay times of both absorption bands are identical within the experimental error. Although through–base mediated transfer is accompanied by very small structural reorganization, in contrast to pyrenyl excimer formation, the electronic nature of both product states must be very similar. Hence, in this measurement simultaneously are probed two different regions of the multidimensional lowest-energy potential energy surface of the system.

3.3.6. Conclusion

Femtosecond broadband pump-probe spectroscopy was applied to monitor local structural dynamics in DNA utilizing two chromophores which were covalently (rigidly) attached to DNA bases but spatially extended into the DNA groove. The results indicate the presence of two electronic coupling pathways. First, a very efficient through-base stack pathway that leads to a new transient absorption band in the dimer systems (**EP2** and **EP3**). The bands rise on the time scale of 300 fs, even in the case when the two chromophores are separated by one **A-T** base pair. Hence it must be concluded that excitation energy can migrate over distances of ~7? . in ~300 fs. Since the ground state structure should not permit direct spatial p -orbital overlap between the chromophores it is likely that the interaction is facilitated through indirect coupling involving excited states of the intervening **A-T** base pair.

The second interaction pathway – which involves direct orbital overlap – has been identified by a pronounced dynamic spectral blue shift. From the analysis of the time-dependent shift is extracted the time scale for local structural motions in DNA. As expected, if the chromophores are in direct contact only minor structural changes are needed to form a stable excimer structure. Hence, the shifting dynamics are completed after 10 ps. In the case where the chromophores were separated by one **A-T** base pair, the overall shifting dynamics

exhibit a long time component of ~ 2ns. This time constant is assigned to local structural motions in DNA involving the reorientation of at least 3 base pairs.

4. Photoinduced processes in artificial multichromophores - Triarylamine redox cascades

4.1. Introduction

The investigations in this chapter are focused on completely artificial light-driven systems based on triarylamines that might be able to induce the long-range separation of opposite charges upon irradiation. The systems of interest are triarylamine cascades in which a hole can be transferred along a redox gradient. The redox centers of these cascades are built up from triarylamines connected by acetylene spacers. Electron transfer or, more precisely, hole transfer processes in triarylamine based systems have thoroughly been investigated in the past.[123-126] Owing to the relatively simple synthetic accessibility and the stability of oxidized triarylamines these units are widely used as hole transport components in optoelectronic devices.[127-132] But also on a molecular level triarylamines have attracted considerable interest: the triarylamine group was used as the charge bearing unit in organic mixed valence compounds for intramolecular ET studies [123-126, 133-137] as well as in organic high spin systems for organic ferromagnets.[138-148] One-dimensional systems with two triarylamine groups have been investigated but also cascades with many triarylamines in a row [149-151] up to polymers [135, 152] and dendrimers.[153-158]

The hole is injected in the cascade by photoinduced electron transfer of an excited acridine chromophore. Triarylamines are used as redox centers for the above mentioned reasons but also because triarylamines possess a relatively low internal reorganization energy.[159, 160] Therefore, HT processes are expected to be rather quick which will favour photoinduced charge separation processes over other competing processes.

The designed cascade structures **A1 – A5** are shown in Figure 4.1 together with the reference systems **A6** – **A8**. The principal features of the cascade systems are the fluorescent donor

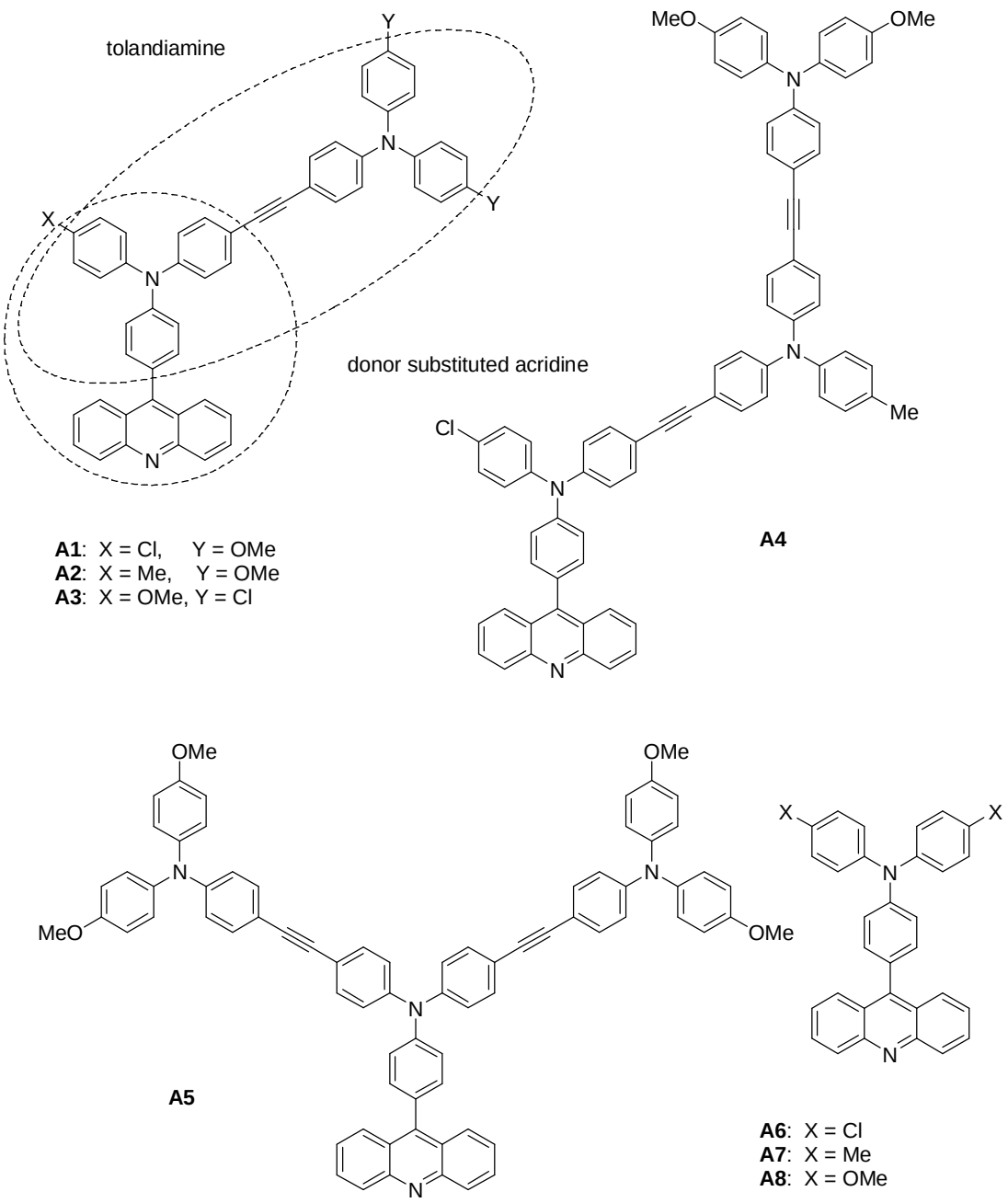

Figure 4.1. *Redox systems A1 - A8.*

substituted acridine chromophore and the triarylamine cascade. The triarylamine units are connected by triple bonds in order to ensure an essentially rigid structure of the whole cascade with fixed HT distances. While the HT distances can be considered as fixed in **A1-A3** and **A5** by the relatively rigid bridge structures, the corresponding distance in **A4** [N(acridin)···N(**TRA**^{3})] can vary between ca. 23 and 29 Å depending on the conformer.

To illustrate the chromophore-bridge cascading approach the redox systems are divided into the following subunits: acridine acceptor (**A**), the first triarylamine attached to the acridine (**TRA**^{1}), the second, and third triarylamine (**TRA**^{2} and **TRA**^{3}) which are farther apart. Two triarylamine groups connected by a triple bond yield a tolandiamine (e.g. **TRA**^{1}=**TRA**^{2}). The donor substituted acridine fluorophore (**A-TRA**^{1}) is a strong oxidizing agent in the first excited charge transfer (CT) singlet state. This locally excited singlet state is expected to oxidize the adjacent triarylamine moiety (**TRA**^{2}) which is attached to the donor substituted acridine by a acetylene spacer.

The photophysics of the donor substituted acridine dyes are are reasonably well understood thanks to the work of Herbich and Kapturkiewicz [161] (HK called in the text of the current chapter). These authors investigated a series of dialkylamino substituted phenylacridines by fluorescence spectroscopy. The local redox potential of the triarylamine units is tuned by substituents (-Cl, -Me, -MeO) in para position of the phenyl rings so as to form two short (**A1, A2**) and one long (**A4**) cascade with downhill hole transport gradient, that is, the triarylamine moiety most apart from the acridine has the lowest redox potential, i.e. it is more easily oxidized than the triarylamine adjacent to the acridine. In a recent study [162] is shown that the redox potentials of triarylamine in tolandiamines may span a range of 400 mV depending on the substituents. For comparison a branched dendrimeric system (**A5**) is also measured as well as a short cascade with uphill redox gradient (**A3**). The photophysical properties of these cascades will be compared with **A-TRA**^{1} subunits **A6-A8.**

4.2. Steady-state optical properties

The absorption spectra of the **A-TRA**^{1} species **A6-A8** show a moderately strong CT band around 25000 cm^{-1} which can be ascribed to a charge transfer from the triarylamine donor to the acridine acceptor [161] (Fig. 4.2). The sharp peaks at ca. 26000, 28000 and 29000 cm^{-1} stem from localized excitations of phenylacridine and the broad and very intense peak at ca. 33000 cm^{-1} is due to a localized triarylamine excitation. The CT bands are somewhat stronger

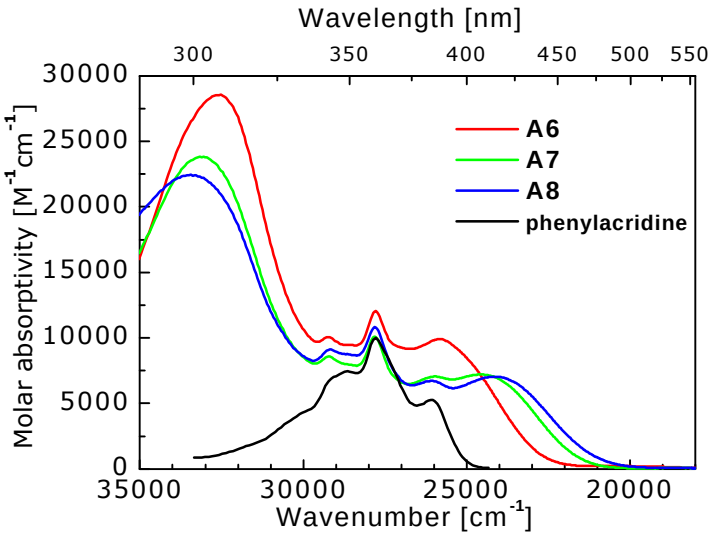

Figure 4.2. *Absorption spectra of A6-A8 and phenylacridine as reference. The solvent is CH_2Cl_2.*

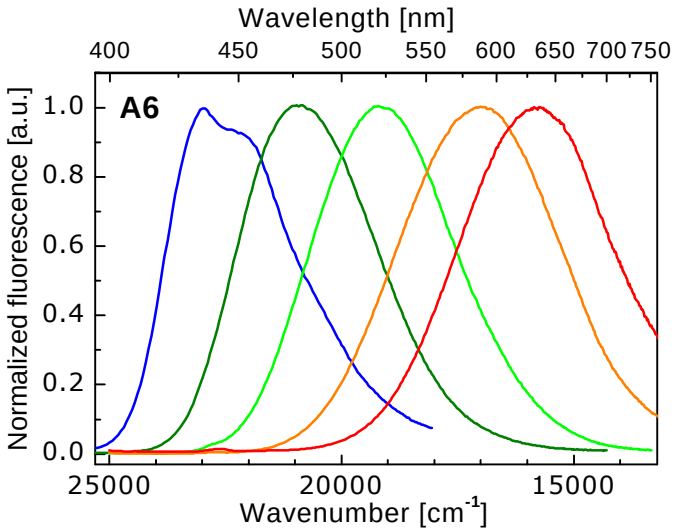

Figure 4.3. *Normalised fluorescence spectra (solid lines) of **A6** from left to right in C_6H_{12}, MTBE, THF, PrCN, DMSO.*

red shifted with MeO substituents than with Me or Cl, that is, the donor strength of the triarylamine unit can be tuned by the *para* substituents attached to the phenyl rings. The absorption CT bands of **A6**-A**8** are moderately positive solvatochromic (e.g. **A6**: 26200 cm^{-1} in C_6H_{12} and 25700 cm^{-1} in DMSO) which indicates an increase in dipole moment upon excitation (the complete data set can be found in [122]. Much in contrast, the fluorescence spectra of **A6**-**A8** are strongly positive solvatochromic and display a huge Stokes shift (see e.g. Figure 4.3 for

the fluorescence spectra of **A6**, the full data set for all compounds can also be found in [122]) which is stronger for **A8** and **A7** than for **A6**. This Stokes shift indicates a major reorganization in the excited state. HK [161] explain this behavior by a solvent depending mixing of a locally excited state and a CT state with a different degree of planarization in the excited state while the ground state is generally nonplanar.

The absorption spectra of the cascades **A1**-**A5** (Figs. 4.4 and 4.5) are much less structured than those of **A6**-**A8** due to severe band overlap. The main feature that is added is a very intense band at ca. 27000 cm^{-1} which is due to the tolandiamine moiety. This band overlaps strongly with the CT band at ca. 25000 cm^{-1} which is only seen as a low-energy tail of the tolan band which prevents a reasonable band deconvolution. From Figure 4.4 it is obvious that the substitution pattern has only a marginal influence on the absorption spectra with exception of the low-energy tail which is more intense in **A3** due to the MeO substituent at **TRA**[1] which makes it a stronger donor compared to **TRA**[1] in **A1** and **A2**. It is also found that the absorption spectra of **A4** and **A5** are quite similar. It is due to the fact that both species have the same number of TRA groups and tolandiamine units. This observation supports the conceptual approach of dividing the cascades into the above mentioned weakly interacting units.

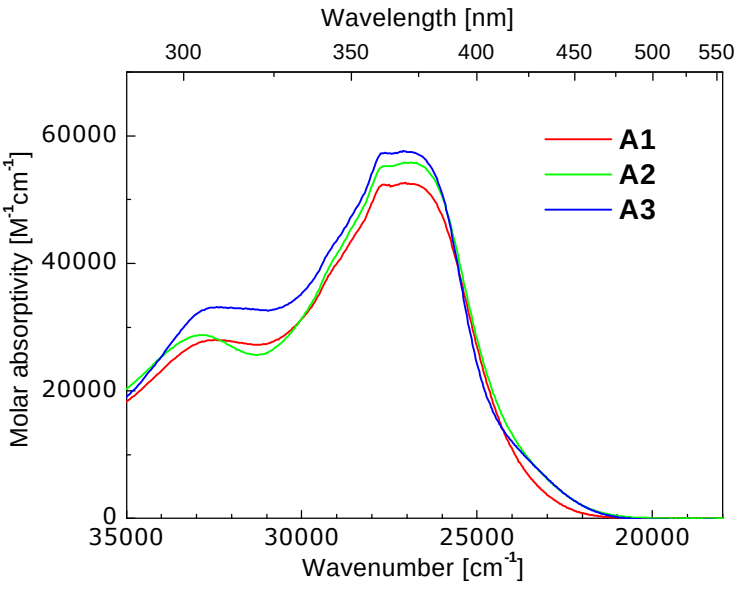

Figure 4.4. *Absorption spectra of **A1**-**A3** in CH_2Cl_2.*

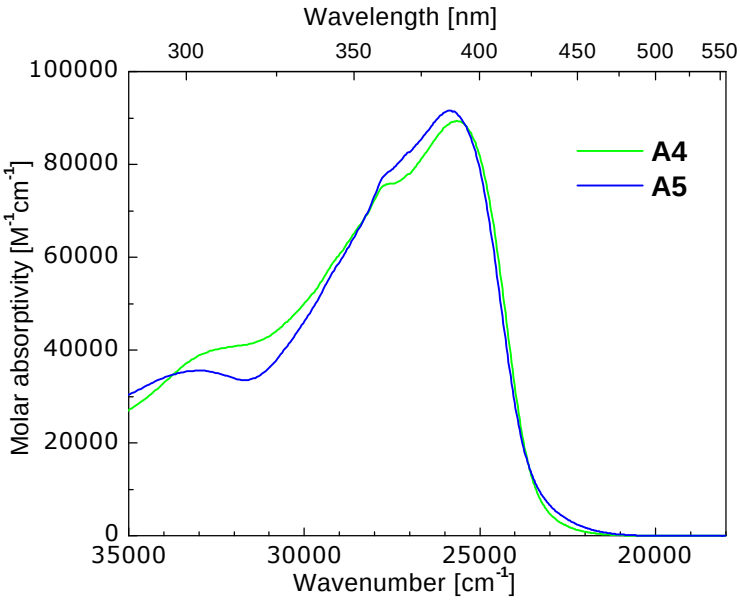

Figure 4.5. *Absorption spectra of **A4** and **A5** in CH_2Cl_2.*

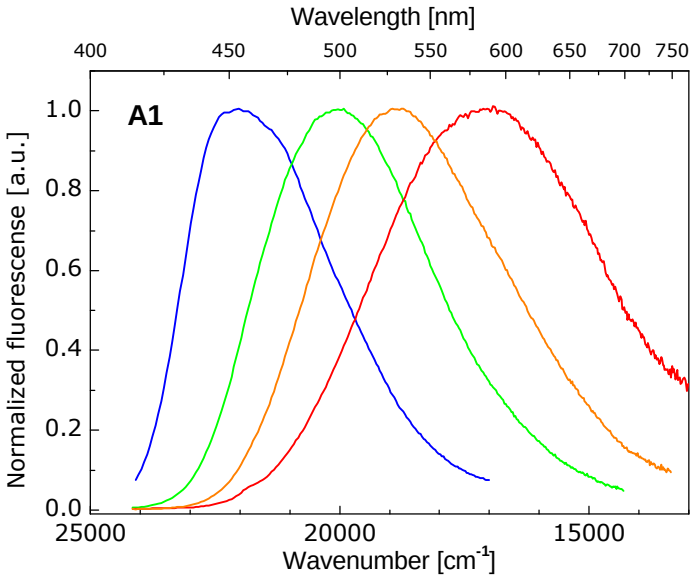

Figure 4.6. *Normalized fluorescence spectra of **A1** from left to right in C_6H_{12}, Bu_2O, Et_2O, THF.*

The fluorescence spectra of **A1-A5** (example **A1** is shown on Fig. 4.6) are all strongly solvatochromic and are very similar in energy and band shape to those of **A6-A8**. However, while there are significant differences in the Stokes shift of **A6-A8** owing to strong substituent effects, the fluorescence energy maxima for **A1-A5** are very similar in a given solvent. Excitation spectra of all compounds are identical to the absorption spectra and show complete energy transfer to the S_1 state.[122] In addition, no fluorescence from the tolan is observed

which should occur between 25000 and 20000 cm^{-1}. Altogether, these features prove that the fluorescent state in the cascades has the same electronic nature as that in the **A-TRA[1]** species **A6-A8**, i.e. all cascades emit from a CT state localized in the **A-TRA[1]** moiety.

4.3. Transient absorption properties

4.3.1. Excited state dynamics in the acridine/triarylamine systems

To elucidate the photophysical mechanisms in the model redox cascades it is crucial to investigate first the dynamics after photoexcitation in the acridine-triarylamine D-A systems without the tolan "antenna". Figure 4.7 shows the temporal evolution of the pump-probe spectra of **A8** measured in three different solvents after excitation at 360 nm. Immediately after excitation there is a broad transient absorption band showing a weak bifurcation with weakly pronounced maxima centered around 610 and 690 nm. This initial spectral distribution which rises within the pulse duration of the experimental setup (~120fs) does not significantly vary with solvent (Fig. 4.7(a)-(c)). After several 100fs, however, the evolution becomes strongly solvent dependent. In acetonitrile (Figure 4.7(a)) the initial two peak distribution gets more pronounced while the band at 690 nm undergoes a shift to 725nm. Reference measurements on the dianisylphenylamine have shown that the lowest excited singlet state of these compounds absorb at ~ 700nm. At the same time dianisylarylamine radical cations absorb at around 730nm.[125] Hence, upon charge transfer in **A8** one would expect to observe a dynamical shift in this spectral region. Acridine radical anions are known to have an absorption band at ~ 600nm.[163] Thus, the temporal evolution of **A8** in acetonitrile reflects an ultrafast *photoinduced* (vs. *optical*) charge transfer from acridine to the triarylamine unit in less than 2ps.

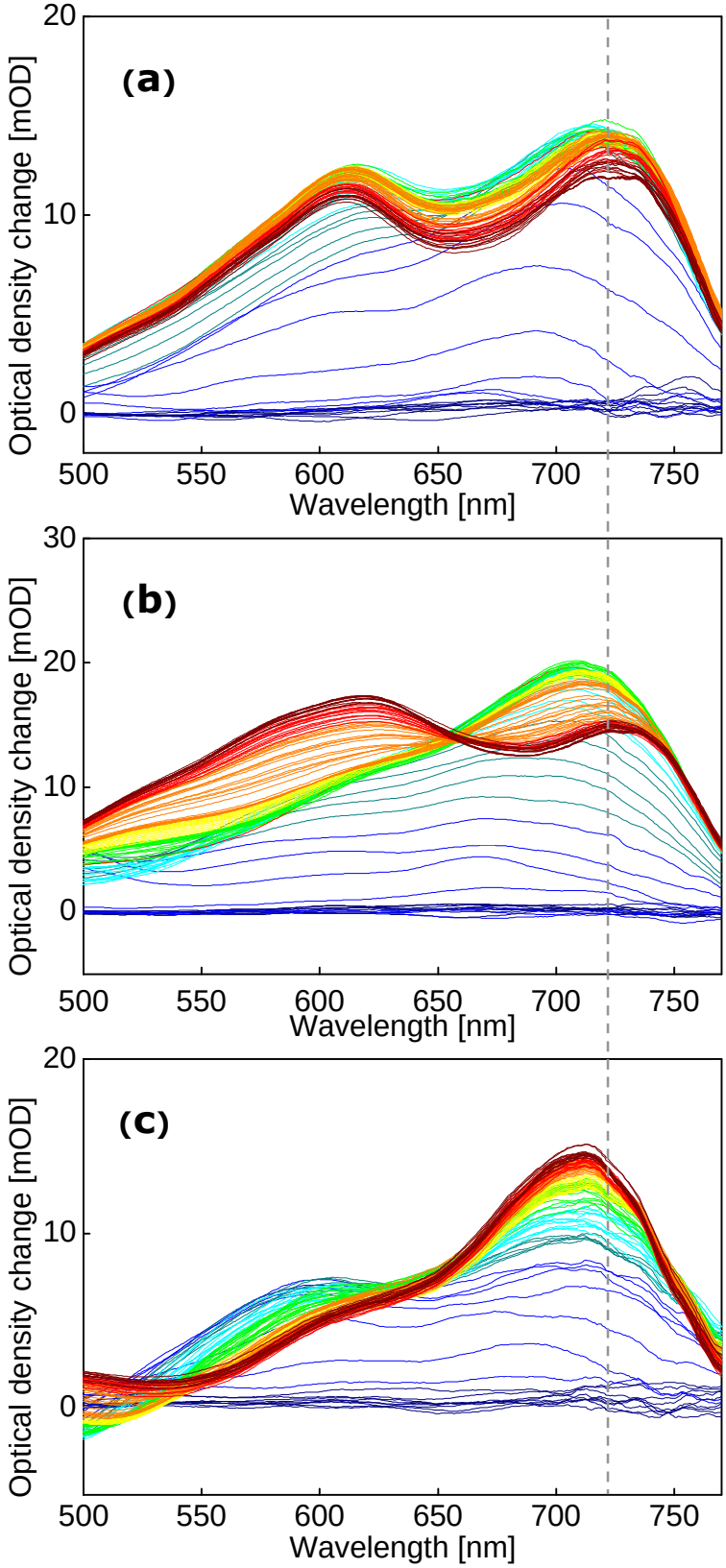

Figure 4.7. *Temporal evolution of the pump-probe spectra of **A8** in different solvents – (a) acetontrile, (b) benzonitrile, (c) MTBE, within the first 20 ps after excitation (various stepsize). Early spectra are shown in blue/green and late spectra are shown orange/red colors.*

In benzonitrile (Fig. 4.7 (b)) the initial spectral bifurcation is merging into a pronounced band at 700nm which reaches its maximum intensity after 500fs. The onset of charge transfer is marked by a spectral shift of the amine radical cation band (accompanied by a drop in intensity) as well as by the rise of the band of the acridine radical anion (610 nm). In contrast to acetonitrile, where the charge transfer process leads to a continuous spectral shift the results in benzonitrile reveal characteristic “two-level” kinetics with a well pronounced isosbestic point at 660nm.

Finally, in MTBE one can observe the rise of the triarylamine excited state absorption band at 710 nm. However, the rise is not followed by a spectral shift towards 730 nm (triarylamine radical cation) and the acridine radical anion band around 610 nm remains absent as well. Consequently, there is no evidence for the population of a strongly dipolar CT state in MTBE.

From the results shown in Figure 4.7 the following mechanistic picture emerges. Excitation of **A8** leads to a largely delocalized excited state with similar electronic (and geometrical) structure in acetonitrile, benzontrile and MTBE. Immediately after excitation, coupling to various nuclear modes (both internal and solvent modes) leads to energy localization on the time scale of 100 fs – 1 ps. The spectroscopic signatures found in the transient absorption spectra suggest that – in all three solvents – a locally excited (LE) triarylamine state is formed shortly after excitation. In the polar acetonitrile, ultrafast energy localization competes with charge transfer which occurs on the same time scale. In benzonitrile, the thermodynamic driving force for CT is much smaller which leads to a reduced CT rate. Hence, energy localization and CT are clearly separable processes. Finally, in MTBE the thermodynamics for CT are highly unfavorable and thus the triarylamine excited state cannot undergo efficient CT.

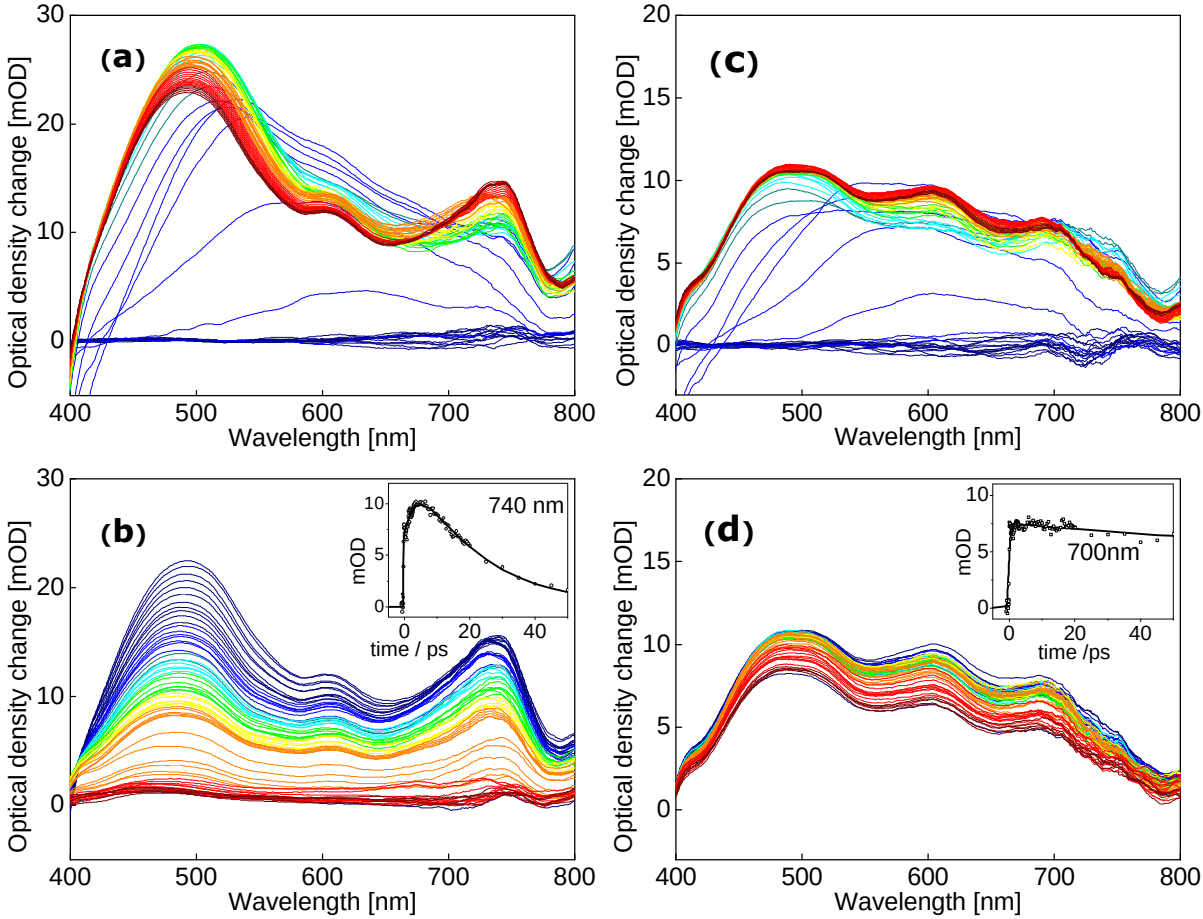

Figure 4.8. *Temporal evolution of the pump-probe spectra of (a),(b)* ***A1*** *and (c),(d.)* ***A3*** *in acetonitrile. The graphs in (a) and (c) represent the dynamics in -0.5 to 3 ps with 60 fs stepsize; (b) and (d) show the interval of 3ps to 150ps after excitation (various step sizes). Early spectra are shown in blue/green and late spectra are shown orange/red colors. The insets show the time-dependent absorption at 740nm and 700nm, respectively*

4.3.2. Charge transfer and effect of driving force in tolan-bridged systems

Photoexcitation of **A1** - **A5** at the pump wavelength (360 nm = 27800 cm^{-1}) initially populates a tolan state (Figure 4.8 shows examples **A1** and **A3**) because this unit has the highest absorptivity at this energy (Figs. 4.4 and 4.5). Hence, the tolan units serve as antenna systems. These tolan states are expected to be the precursor states for ultrafast intramolecular energy transfer to the corresponding charge transfer states. Immediately after photoexcitation of **A1** and **A3** one can observe a broad, structureless absorption band between 500 and 700nm (Fig. 4.8(a) and (b)). This band represents the absorption of the unrelaxed Franck Condon state populations.

After several 100fs there are three main transient absorption bands, the 610nm (acridine radical anion), the 700-740 nm band, and a very intense band at 490 nm which must be assigned excited state absorption of the tolan system. The fact that the tolan band at 500 nm is present throughout the lifetime of the excited states of **A1**-**A5** must be viewed as a clear indication that the transient absorption spectra cannot be reconstructed by (diabatic) mixing of spectral reference components obtained from separate measurements. Hence, the electronic coupling between the chromophores is significant.

The inset in Figure 4.8 b) also displays the time-dependent transient absorption signal of the 740 nm band. In contrast to **A8** (acetonitrile) where this band rises within the time resolution of our experimental setup the rise of this band in **A1** is strongly biexponential, i.e. it shows a rise time of 4ps (40%). This rise time must be interpreted as the hole transfer time from the triarylamine ($\mathbf{TRA^1}$) which is adjacent to the acridine to the terminal amine ($\mathbf{TRA^2}$).

Because of the substitution scheme in **A3** hole transfer between the central and the terminal amine unit is thermodynamically unfavorable. Hence, a charge transfer state of the type $\mathbf{A^-}$–($\mathbf{TRA^1}$)$^+$–$\mathbf{TRA^2}$ is formed. Entirely consistent with this proposal is the fact, that the rise of the 740 nm band in **A3** is not showing a picosecond component (Fig. 4.8 (d) inset).

A comparison of the 740nm transients of **A1** and **A3** (insets of Figure 4.8 (b) and (d)) reveals a significantly longer lifetime of the CT state of **A3**. However, in addition to these differences the intensity ratio reveals also interesting information about the excited state relaxation in **A1** and **A3**. Most obvious is the difference in the relevant contribution of the 610nm band which is significantly stronger in **A3** than in **A1**, suggesting a more localized, twisted acridine radical anion in **A1** than in **A3**. In fact, this interpretation is in agreement with the rest of the data: In **A3** the charge is only being transferred between the acridine and the adjacent $\mathbf{TRA^1}$ unit. In order to establish a large dipole moment the acridine has to twist to electronically decouple from the rest of the aromatic system. This will result in a fairly pure acridine radical anion band. The CT state dipole moment of **A1** is somewhat larger than that of **A3** (the slope of A**1** is larger than A**3** in the Lippert-Mataga plot in [122]), however one has to

bear in mind that the positive charge is delocalized much farther over the second amine unit. Hence, the negative charge on the acridine will also be delocalized. As a result, the radical anion character is “diluted” which is manifested in the reduced 610nm band.

4.3.3. Effect of redox cascade extension.

Figure 4.9 shows the temporal evolution of the pump-probe spectra of **A4** and **A5** in acetonitrile. The insets display the time-dependent transient absorption at 740 nm (triarylamine radical cation band). A comparison of the symmetrical “doubly-branched” system A**5** with its single-branch analogue it becomes clear that the spectral properties are very similar (both in time evolution and in spectral distribution) suggesting that the two tolan branches are acting as independent substituents. Figure 4.9b shows the spectral dynamics in the extended redox system **A4**. Most noticeable is the kinetic behavior (Fig. 4.9 (b) inset) which differs qualitatively and quantitatively from all other systems. The instant rise of the 740nm signal is followed by an ultrafast decay (200-300fs) and then another slow rise with a time constant of 20 ps. These characteristics can be explained by assuming that the signal is composed from two overlapping contributions, i.e. two chromophores with similar absorption properties. Given the structure of **A4** it seems reasonable to propose the following model: Photoexcitation at 360 nm of the tolan units leads to two parallel processes: a direct charge separation from the tolan excited state which yields $\mathbf{A^{-}\text{-}TRA^{1}\text{-}TRA^{2}\text{-}(TRA^{3})^{+}}$ (which occurs in 200-300 fs) and a slower hole transfer from the CT state $\mathbf{A^{-}\text{-}(TRA^{1})^{+}\text{-}TRA^{2}\text{-}TRA^{3}}$ which again leads to $\mathbf{A^{-}\text{-}TRA^{1}\text{-}TRA^{2}\text{-}(TRA^{3})^{+}}$ in 20 ps. The latter process is analogous to the ones observed in the shorter cascades.

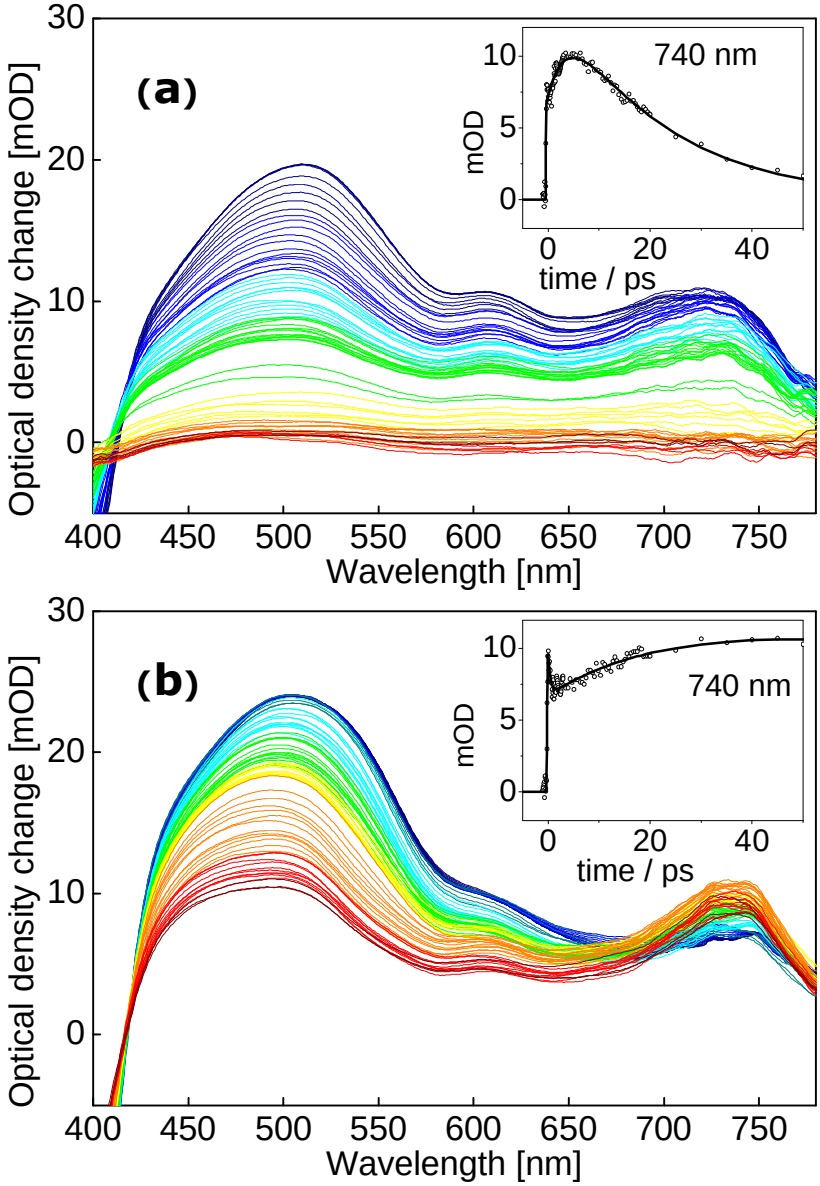

Figure 4.9. *Temporal evolution of the pump-probe spectra of (a)* ***A5*** *and (b)* ***A4*** *in acetonitrile, 2ps to 150ps after excitation (various step sizes). Early spectra are shown in blue/green and late spectra are shown in red/dark red colors. The insets show the time-dependent absorption at 740nm.*

The direct transfer can be rationalized based on the fact that the tetraaryl tolan adjacent to the acridine is actually an electron D/A moiety which can form biradical intermediates. Hence, upon excitation of the tolan system in **A4** there is – dependent on the conformation of the molecule – an initial extent of charge separation which will immediately undergo relaxation towards the final extended charge transfer state within 200-300 fs. The rate constants for HT and charge recombination resulting from spectra deconvolution of the pump-probe measurements for **A1,**

A2, A4 and **A5** in acetonitrile and benzonitrile are collected in Table 4.11. From these data it is apparent that the extension of the cascade (**A4** vs **A1**) slows down both k_{HT} and k_{CR} by one order of magnitude. In the same way replacement of the polar acetonitrile by the less polar benzonitrile slows down both rate constants by one order of magnitude because back electron transfer occurs in the Marcus inverted region. For comparison, the rate constants k_{HT} from fluorescence measurements in CH_2Cl_2 are also given in Table 4.11. The values are still smaller than those obtained in benzonitrile because CH_2Cl_2 is less polar.

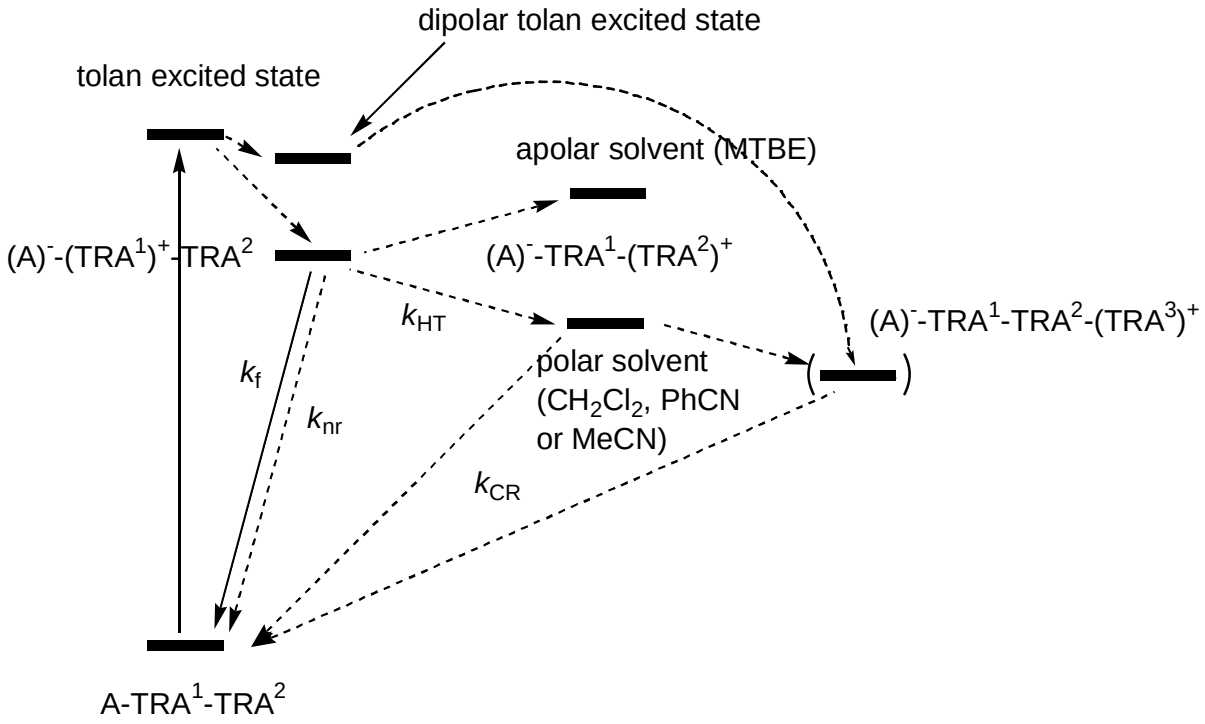

Figure 4.10. *State diagram for **A1**,**A2**, and **A5** (left hand side) and for **A4** (extension right hand side).*

	ACN (TA)				BZN (TA)				CH_2Cl_2 (Ref. [122])
	t_{HT} /ps	(k_{HT}/10^9 s^{-1})	t_{CR}/ps	(k_{CR}/10^9 s^{-1})	t_{HT} /ps	(k_{HT} /10^9 s^{-1})	t_{CR} /ps	(k_{CR}/10^9 s^{-1})	(k_{HT} /10^9 s^{-1})
A1	3.2	(310)	22	(45)	30	(33)	180	(5.5)	(1.2)
A4	20	(50)	410	(2.5)	250	(4)	> 2000	(<0.5)	--
A5	2.3	(440)	23	(44)	28	(36)	480	(2.1)	(0.96)

Table 4.11. *Rise time t_{HT} of the transient absorption peak at ca. 740 nm and k_{HT} as well as life time t_{CR} of the final charge separated state and k_{CR} of the charge recombination.*

5. Ultrafast electron solvation dynamics

5.1. Motivation

The dynamics of chemical reactions in solutions strongly depend on the interactions between the reactants and the solvent molecules. In the last decade particular interest has been developed to ultrafast electron transfer in ionic solutions.[164-167] The most prominent type of electron transfer is the one shown by halide anions in solution. Isolated halides in the gas phase support no bound electronic excited states below the detachment threshold.[168] For a halide anion embedded in a water cluster, the ionization potential increases with the cluster size, due to the solvation induced stabilization of the ground state anion. [169, 170] Consequently, in a bulk solution, these anions show an intense near-UV absorption at energies well below the ionization threshold. Photoexcitation in this absorption band produces a neutral halogen atom and a solvated electron. Therefore this class of intermolecular transitions is called charge-transfer-to-solvent (CTTS). [168] The sensitivity of the CTTS states to the solvent environment makes them ideal candidates for investigating how local solvent structure, solvent-induced radiationless relaxation, and solvation dynamics control electron transfer reactions.

The sub-picosecond electron detachment of aqueous chloride solutions after *two-photon* excitation was examined by Gauduel et al. [166, 171] and other groups.[172, 173] Eisenthal and co-workers carried out a time resolved study of solvated electrons formed after *two and three-photon* excitation of aqueous iodide solutions. [165, 174] The experiments stimulated detailed theoretical studies of Sheu and Rossky.[175, 176] The molecular dynamics (MD) simulations predict two formation channels of the solvated electron after population of a high-lying CTTS-state of the iodide: Direct nonadiabatic electron separation (within 50 fs) or fast relaxation within the CTTS states to the lowest charge transfer state (time constant of 450 fs) and subsequent adiabatic separation of the electron from the iodine. A complex was predicted consisting of an atom, between an electron and a water molecule. The structure obviously

displays spectral features similar to that of a hydrated electron since the first solvation shell of the charge is solely occupied by water molecules. Geminate recombination of the complex was predicted to occur within a few picoseconds, whereas the release of the electron appeared to be unlikely in the computations. The result is not consistent with the large yield of the generated solvated electrons found experimentally.[165, 174]

More recent computations of Staib and Borgis [177, 178] for an aqueous chloride solution arrived at somewhat different conclusions due to the more detailed treatment of the solvent polarization. The results of these authors may be summarized as follows: The initial excitation of the anion in the lowest charge transfer state was considered that leads to an excited state absorption centered at 1.13 µm.[178] Within the first 100 fs the electron separates ~4 Å from the parent chlorine core. In the following first picosecond the system develops a larger chlorine–electron separation of ~6 Å that is accompanied by a continuous shift of the induced absorption from 950 to 720 nm. The calculated free enthalpy *G(r)* of the system exhibits a distinct minimum around r_{min} = 6 Å which lies ΔG = 3 ± 0.5 $k_B T$ below the value for complete detachment. The pair dissociation competes with a nonadiabatic recombination of the electron and chlorine atom. Based on the results of the MD quantum simulations Staib and Borgis proposed a simple kinetic model for the relaxation dynamics after photoexcitation of aqueous chloride. The CTTS excited Cl^-_{aq} is converted into the hydrated (Cl:e^-) pair with a rate $k_{gen} = 2.5$ ps^{-1}.The latter can dissociate ($k_{diss} = 0.031$ ps^{-1}) while the nonadiabatic recombination to a ground state anion Cl^- is slower ($k_{rec} = 0.001$ ps^{-1}).[178]

Bradforth and co-workers recently presented experimental data on aqueous iodide [179-181] at room temperature after one-photon excitation into the lowest CTTS band. Using the discussed kinetic model a formation time of the hydrated *iodine:electron* pair of $k_{gen}^{-1} = 200$ fs as reported.[179] The complex subsequently recombines with a time constant of $k_{rec}^{-1} = 33$ ps or dissociates with a time constant of $k_{diss}^{-1} = 70$ ps. The latter value obviously represents an upper limit and not the relaxation time directly, since geminate recombination of dissociated electrons, i.e., hydrated electrons, was omitted in the analysis. Correspondingly it was shown that the

simple model cannot describe the recombination dynamics for times larger than 100 ps when slow contributions to diffusive recombination appear.[180, 181] Therefore, the long-tail dynamics is analyzed with the help of a diffusion recombination in the absence of an interaction potential. The extracted parameter values, however, of 26 and 24 Å, obtained, respectively, for the initial and recombination distance between the iodine and the electron are not meaningful. Kloepfer et al.[181] also obtained a numerical solution of the partially diffusion-controlled geminate recombination of a pair in the presence of an interaction potential using a code provided by Krissinel and Agmon.[182] The extracted well depth and position of the minimum of the free enthalpy were $\Delta G = 620$ cm^{-1} and $R_0 = 4$ Å , respectively.[181]

The experimental studies support the microscopic picture for the electron detachment of aqueous halides developed from MD simulations. One important aspect of the relaxation dynamics of the *atom:electron* pair however is still missing: experimental information about the lifetime of the hydrated *iodine:electron* pairs. The temperature-dependent observations are intend to provide novel information on the relaxation dynamics of the *atom:electron* pair and give experimental support to the MD prediction of an attractive interaction between the separated electron and the parent atom.

5.2. Temperature-dependent pump-probe data

In this chapter the temperature dependence of the photoionization dynamics is investigated that provides some evidence of the pair dissociation rate. To this end, a series of pump–probe experiments on aqueous I^- is carried out at three temperatures, 25, 50 and 75°C. The relaxation dynamics after single-photon excitation into the first CTTS band is studied with broad-band femtosecond probe pulses in the spectral range 425–1100 nm as described in section 2.1.4. The sample cell, equipped with 1-mm windows of UV grade fused silica, has a thickness of 250 µm and is filled with a circulating solution of NaI (Merck Eurolab, GR for analysis) in de-ionized water at a concentration of about 2.5 mM. In order to maintain a constant sample temperature,

the solution passes a temperature controller right before the sample cell. Because of a sufficiently large quantity of the investigated liquid volume

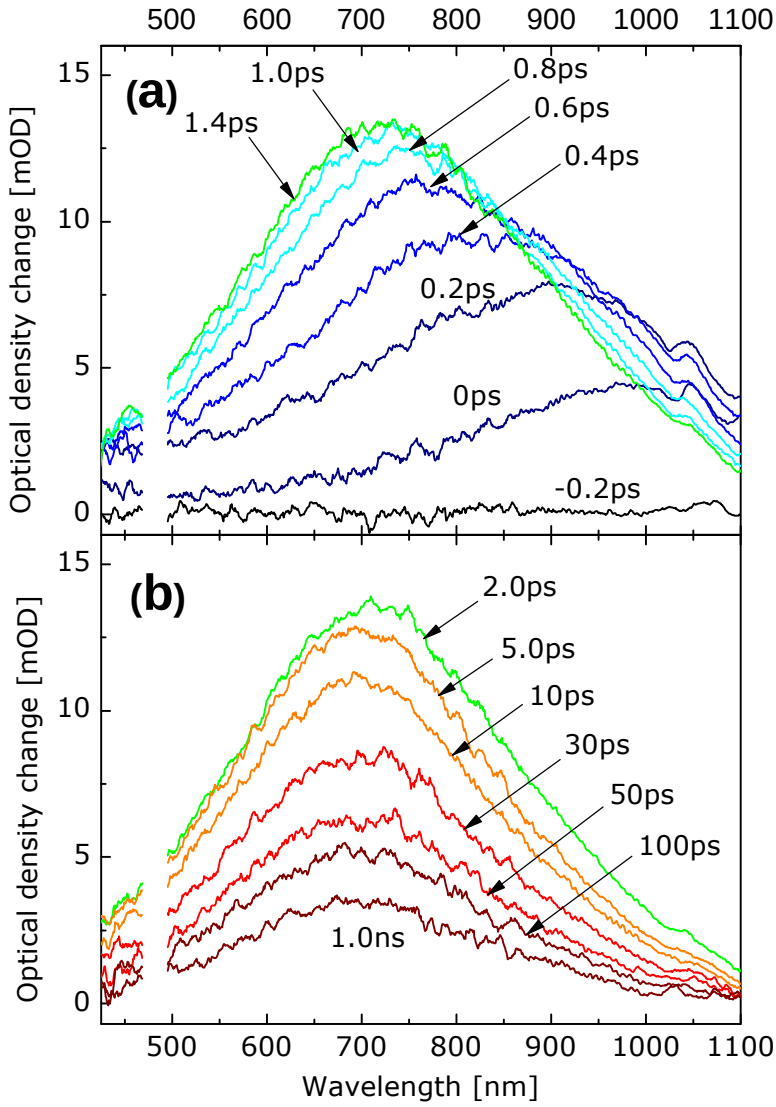

Figure 5.1. *Temporal evolution of the absorption changes of an aqueous NaI solution at 25 °C after excitation at 242 nm; different delay time values are indicated in the inset.*

(900 ml) the concentration of undesired photo-products like I_2 can be neglected.

The measured transient absorption spectra at 25 °C after single-photon excitation at 242 nm are presented in Figure 5.1. Only several representative spectra at selected delay time values are shown. Around 484 nm a gap of the probe data occurs that is due to the partial scattering of pump radiation into the probe beam direction. While no meaningful signal is found at negative delay times (-200 fs), the instantly appearing absorption change is seen at wavelength range 650

to 1000 nm (spectra at time zero t_D = 0 ps in Fig. 5.1(a)). The maximum of this early absorption appears at 1000 nm, but cannot be accurately determined with the available probing range (up to 1100nm). The absorption band grows within the next 200 fs and its maximum shifts to ≈900 nm. Increasing the delay time the maximum of this absorption shifts to shorter wavelengths and is located at ≈760 nm (t_D = 0.6 ps, Figure 5.1a) only 400 fs later. At later delay times the absorption narrows notably and reaches a stable maximum position at ≈720 nm. A spectrum close to that of the equilibrated solvated electron [183] is reached at t_D = 1.4 ps. An isosbestic point is not indicated by the transient spectra of Figure 5.1a. Hence, it is concluded that more than one intermediates are involved in the dynamics.

The measurements for larger delay times up to 1 ns (Figure 5.1b) indicate that the changes in the absorption band shape have terminated approximately 3 ps after the excitation. The agreement with the absorption of the fully solvated electron provides strong evidence that at least the first solvation shell of the separated electron is already fully established at this time. The subsequent relaxation (Fig. 5.1(b)) can be assigned to population decay, i.e., geminate recombination of the photogenerated electron with the parent atom.

For the same experimental conditions, but at higher temperatures of 50 and 75 °C, corresponding measurements were carried out obtaining a similar time evolution of the spectra (data not shown). At longer delay times ($t_D \geq$ 1.5 ps) the absorption band is found to be slightly broadened and red-shifted as compared to the data of Figure 5.1(b). The observed band maxima are located at 750 and 775 nm for 50 and 75 °C, respectively.

This spectral shift is in close agreement with the well-known temperature dependence of the absorption spectrum of the equilibrated solvated electron.[183] Three representative kinetics at 575, 725 and 1075 nm are shown in Figure 5.2. (experimental points, calculated solid lines). The maximal absorbance change measured at the respective probing wavelength for the higher temperatures are normalized to the value at 25 °C for a direct comparison.

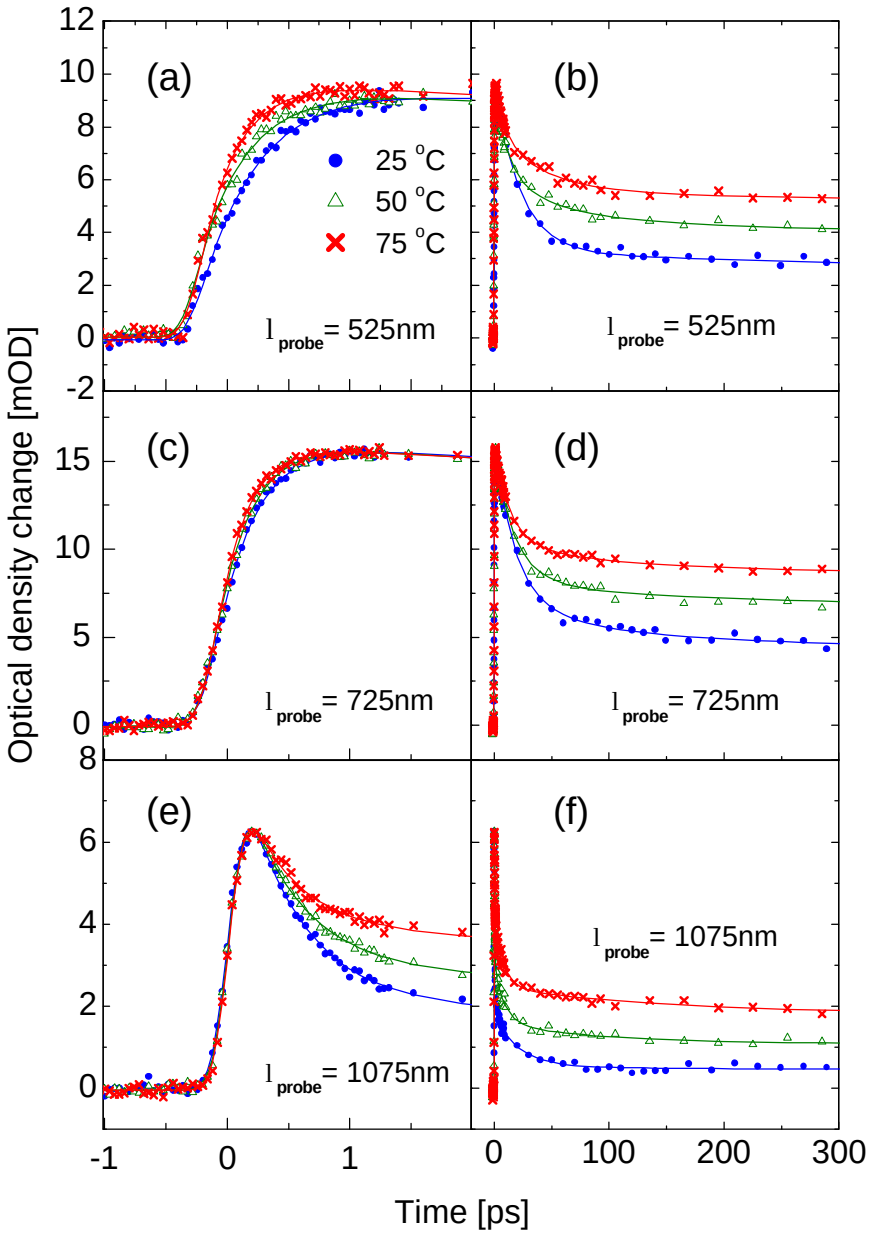

Figure 5.2. *Time evolution of the absorption changes of aqueous iodide after excitation at 242 nm taken at 575, 725 and 1075 nm for temperatures of 25 °C (full points), 50 °C (open triangles) and 75 °C (crosses).The solid lines represent calculated (fitted) data .*

Different delay time intervals are depicted in the left and right panels of the Figure 5.2. The temperature dependence is noteworthy. Especially at 575 nm the induced absorption at 25 °C (full circles in Figure 5.2a) increases more slowly as compared to higher temperatures. The signal reaches a maximum at t_D ~ 1.5 ps. In the near infrared the ultrafast dynamics is almost reversed. The signal transients at 1075 nm (Figure 5.2 (e)) reach a distinct maximum instantaneously (at $t_D \approx 0.2$ ps). The subsequent decay occurs with an effective time constant of

≈0.5–0.7 ps. The measurements for larger delays up to 300 ps (right panels of Fig. 5.2) indicate that after the maxima around $t_D \approx 1.5$ ps the absorption curves decrease to different plateau values, depending on temperature but within time intervals independent of the probing wavelengths. The relaxation profile cannot be fitted by a simple exponential decay. This finding supports the assumption that the long-time dynamics are dominated by diffusion controlled geminate recombination.[181] One can conclude from Figure 5.2 that the fraction of electrons undergoing geminate recombination in the aqueous iodide solution obviously decreases as the temperature rises.

A similar dependence was reported for the photoionization of aqueous hydroxide[184] and pure water.[185] But the exact values for the survival probability of the hydrated electrons reported for the latter solutions are different from that of aqueous iodide.[185]

We finally mention that measurements of a pure water sample under the same excitation conditions show no measurable effect within experimental accuracy (data not shown). Therefore, a contribution of photoionization of the solvent to the signal transients is negligible.

5.3. Data analysis

According to the arguments in section 5.1 the initially excited lowest charge transfer (LCT) state undergoes a decay with a time constant t_1. The followed electron separation is accounted for by a discrete precursor state $(I{:}e^-)_{non\text{-}eq}$. Subsequently, a quasi-equilibrated hydrated *halogen:electron* pair $(I{:}e^-)_{hyd}$ is formed, representing a further intermediate state. The formation and solvent relaxation of the pair takes a time constant t_2 that is the decay time of the precursor $(I{:}e^-)_{non\text{-}eq}$. The relaxation of the weakly bound *atom:electron* pair $(I{:}e^-)_{hyd}$ may be described by three-dimensional diffusion of the particles in the presence of a radially symmetric potential

$$U(r) = \Delta G\{1 - \exp[-b(r - R_0)]\}^2 \qquad (15)$$

Here ΔG is the depth of the potential well. r and R_0, respectively, denote the particle separation and minimum position. The scaling factor b accounts for the potential width. The

relaxation of the pair in this potential is governed by the spherically symmetric Debye–Smoluchowski equation. [186]

A method for a numerical solution of this equation is based on the detailed-balance approximation.[187] A brief description of the used numerical algorithm will be given. It begins with a discretization of the radial coordinate r, from contact radius r_c (i = 0) between atom and electron to some maximum value r_{max} (i = m). Hereby i represent the number of the corresponding layer (Fig. 5.3). The resulting radial layers are accounted for by separate states with populations equal to the average population density of the layers. In this approximation a population exchange exists just between adjacent layers, while the exchange rates depend on the interaction potential.

The transition rate Ω from a state $|j\rangle$ to a neighboring state $|i\rangle$ ($i = j \pm 1$) is given in [187]:

$$\Omega(i|j) = (D/\Delta r^2)(r_i/r_j)\exp[-(V(r_i) - V(r_j))/2] \qquad (16)$$

Here $D = D_{Io} + De^-_{aq}$ is a mutual diffusion coefficient, and $V(r) = U(r)/k_BT$ is the normalized potential depending on temperature. The equilibrated *iodine:electron* pair is generated at distance $r = R_0$ with rate $1/t_2$, while the backward reaction leading to the ground state anion occurs simultaneously at the contact distance $r = r_c$ (absorbing boundary condition).

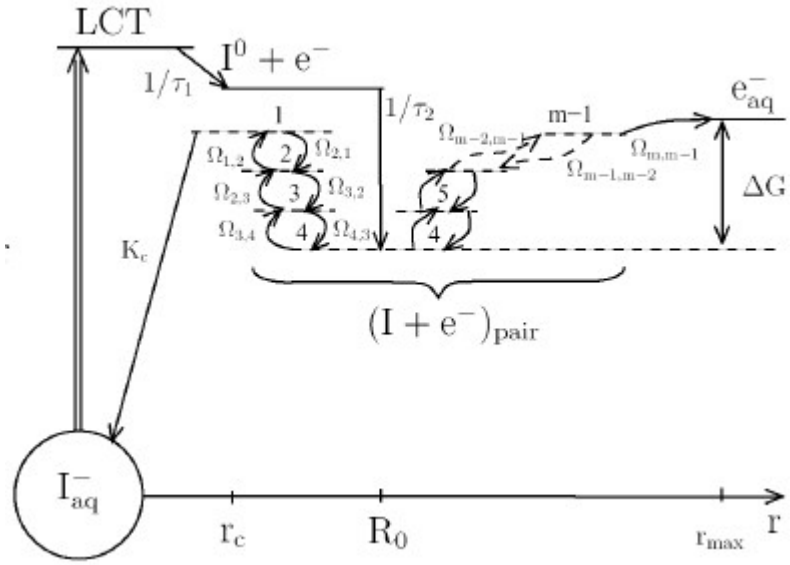

Figure 5.3. *Energy level scheme used to account for the measured dynamics during the photodetachment of electrons from aqueous iodide solution.*

On the other hand r_{max} is taken large enough (>15 Å), so that the gradient of the potential curve is negligible. At these distances the electron is expected to be fully solvated and quasi-stable so that the recombination rate vanishes. The terminating level is the equilibrated, hydrated electron e^-_{aq}.Consistent with the MD results and the data of Figure 5.1b), it was assumed that the spectral properties of the hydrated pair in the probing range are constant during the dissociation process and agree with the absorption of the solvated electron. This spectral similarity supports the assumption that the $(I:e^-)_{hyd}$ is assembled from a solvation configuration with an iodine an electron and a water molecule in between. The microscopic picture provides the possibility to estimate the I–e^- distance to be R_0 = 6.1 Å as the sum of the iodine–oxygen distance ($R_{I–O}$ = 3 Å) [188] and the radius of the first solvation shell of the electron ($R_{O–e^-}$=3.1 Å) [189] distances in aqueous solution. The mutual diffusion coefficient at room temperature was estimated to be D = 0.56 Å^2/ps from the reported numbers D_{I^0} = 0.1 Å^2/ps [190] and $D_{e^-_{aq}}$ =0.46 Å^2/ps [191] for the components. The values of D at 50 and 75 °C were treated as fitting parameters. The free parameters of the model (relaxation rates, potential constants, extinction coefficients, etc.) are obtained by fitting the calculated curves (solid lines in Figure 5.2) to the measured signal transients using Powell's method.[192]

5.4. Discussions

The results of the data analysis are graphically represented in Figure 5.4 and are summarized in Table 5.5. After population of the LCT state of the iodide by a 5.1 eV photon, a broad absorption appears in the near-infrared with a maximum close to 1000 nm at all three temperatures. The excited state absorption of LCT (filled squares and dotted lines on Figure 5.4) may be assigned to transitions to higher lying CTTS levels. The relaxation of LCT assigned to the escape of the electron from the parent solvent cavity is found to occur with time constants t_1 = 220–180 fs, going from 25 to 75 °C (Table 5.5).

An important property of the solvated electron is the high sensitivity of its absorption spectrum to the local environment.[193] Thus the rapid development of the transient absorption spectra observed within the first 1 ps (Fig. 5.1(a)) supports the conclusion that the initial

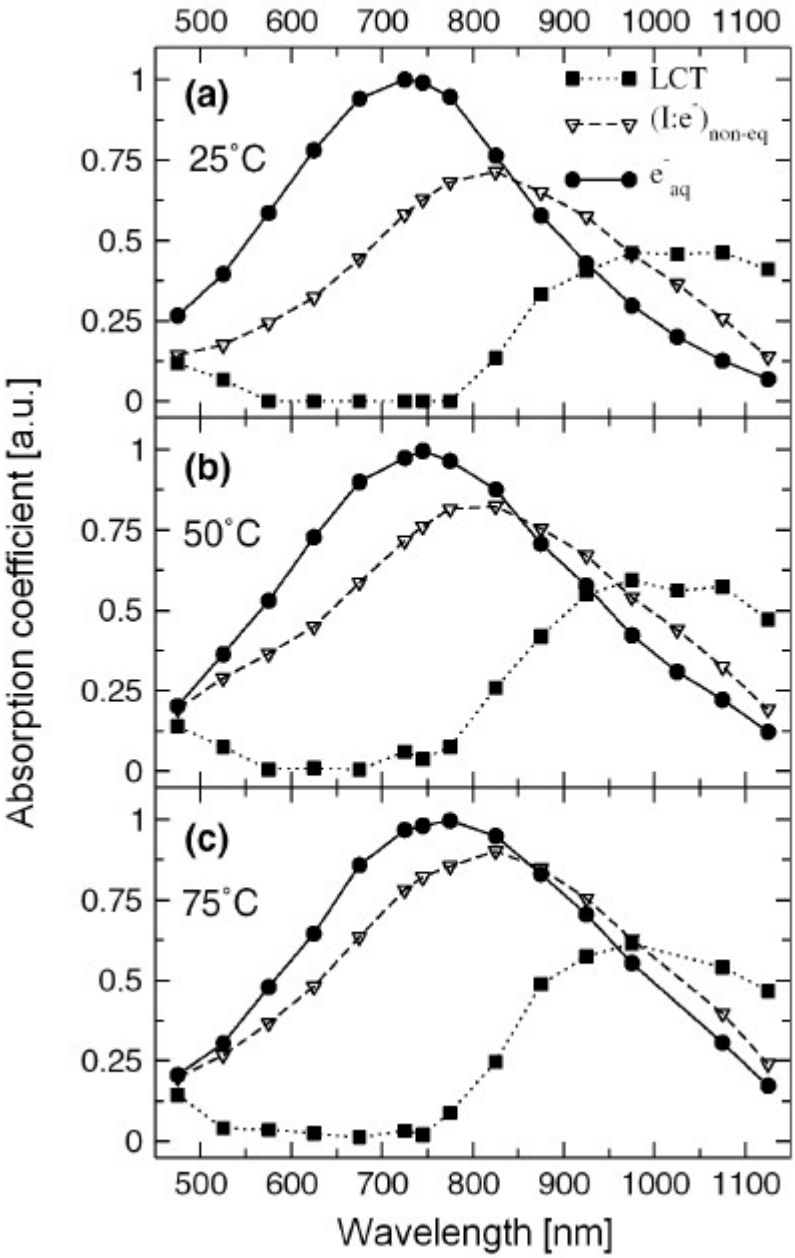

Figure 5.4. *Molar absorption coefficients of the observed intermediates assigned to the initially excited LCT state (filled squares), the transient* $(I{:}e^-)_{non\text{-}eq}$ *state (hollow triangles), together with that of the final product: equilibrated solvated electron (filled circles). The points are obtained by fitting the theoretical model to the experimental data shown in Figures 5.1 and 5.2. The points are interconnected with lines for easy viewing.*

relaxation dynamics is accompanied by a continuous reorganization of the electron solvation cavity. The argument is in accordance with the MD prediction for the separation of the electron from the parent halogen.[178] Because of different time scales involved in the electron detachment and as is discussed above, the process is divided in the model into two steps. A first intermediate of the pair is formed that is assigned to an *atom:electron* pair in a yet non-equilibrated solvent configuration $(I{:}e^-)_{non\text{-}eq}$. The experimental data support this picture. The intermediate is characterized by a broad absorption band centered at 825 nm (hollow triangles and dashed lines in Figure 5.4). The spectral profile of the intermediate and its built-up rate $1/t_1$ are only weakly temperature dependent in the investigated range. The finding suggests that increasing the solution temperature the relaxation pathway remains unchanged. The further separation of the excess electron from the iodine atom and organization of the new solvation layer leads to the hydrated *atom:electron* pair $(I{:}e^-)_{hyd}$. This complex shows an absorption spectrum similar to that of e^-_{aq} (Fig. 5.1). For the formation of the $(I{:}e^-)_{hyd}$ the time constant t_2 is found to vary from 700 to 540 fs for temperatures from 25 to 75 °C.

	25° C	50°C	75°C	Ref. [25]	Cl^-_{aq}, Ref. [15]
t_1 [fs]	220 ± 50	200 ± 50	180 ± 50	200	100
t_2 [fs]	700 ± 50	650 ± 50	540 ± 50	–	400
D_0 [Å^2/ps]	0.58	0.95 ± 0.1	1.35 ± 0.1	0.8	0.78
r_c [Å]	5.0 ± 0.1	(5.0 ± 0.1)	(5.0 ± 0.1)	4.0	–
R_0 [Å]	6.1	(6.1)	(6.1)	4.0	6.0
b [Å^{-1}]	0.68 ± 0.05	0.80 ± 0.05	0.93 ± 0.05	1.1	–
ΔW [Å]	2.6 ± 0.2	2.2 ± 0.2	2.0 ± 0.2	–	3
ΔG [cm^{-1}]	850 ± 100	830 ± 100	860 ± 100	620	620 ± 100
h	0.25 ± 0.02	0.39 ± 0.02	0.53 ± 0.02	0.25	0.75
t_{pair} [ps]	21 ± 2	17.5 ± 3	16 ± 2	22	32

Table 5.5. *Summary of the relaxation times and fitting parameters for photoelectron geminate recombination with iodine at 25°C, 50°C and 75°C. The values in brackets are input parameters taken from 25 °C measurement.*

The rise of the formation rate may be attributed to the higher mobility of the water molecules at increased solvent temperature. The hydrated complex $(I:e^-)_{hyd}$ is stabilized by an attractive interaction described by a Morse potential. The extracted well depth ΔG = 850 ± 100 cm^{-1} remain unaffected by temperature variation (as shown in Table 5.5). The contact distance r_c at which the recombination between the excess electron and the parent occurs, is fitted to be 5.0 ± 0.1 Å. The numbers for R_0, and r_c at 25 °C are assumed to depend only weakly on temperature and used as input parameters in the analysis of the dynamics at the higher temperatures. For the Morse constant the numbers seem to increase from ß = 0.68 ± 0.05 to 0.93 ± 0.05 $Å^{-1}$ going from 25 to 75 °C. The corresponding full half width ΔW of the potential curve decreases from 2.6 ± 0.2 Å at 25 °C to 2.0 ± 0.2 Å at 75 °C. Adopting the above developed microscopic picture the faster decrease of the iodine–electron attraction may be related to the higher vibrational energy of the water molecules in the solvation layer of the *atom:electron* pair with rising temperature. From the description of the measured long-time dynamics (right panels in Figure 5.2) the effective lifetime t_{pair} of $(I:e^-)_{hyd}$ can be determined with a simple exponential fit. The experimental data show that this time constant decreases from t_{pair} = 21 ± 2 ps to 16 ± 2 ps going from 25 to 75 °C. The results for the mutual diffusion coefficient D_0 are 0.95 ± 0.1 and 1.35 ± 0.1 $Å^2$/ps at 50 and 75 °C, respectively. The values are consistent with the well-known temperature dependence of $D_{e\text{-}aq}$.[191] The strong temperature dependence of the diffusion coefficient reflects the corresponding variation of the quantum yield h for generating fully solvated electrons. The data show (Table 5.4) that 1 ns after the optical excitation the ratio of fully solvated electrons to the *atom:electron* pairs at t_D = 1.5 ps increases from h = 0.25 ± 0.02 to 0.53 ± 0.02 in the range 25–75 °C. These numbers are smaller than those measured for aqueous F^- at room temperature, where h = 0.77 ± 0.03.[167] Taking into account the similar diffusion coefficient, D_F = 0.33 $Å^2$/ps,[190] this variation shows the strong influence of the halogen atom on the ps relaxation dynamics, i.e., gives some experimental support to the existence of *atom:electron* pair.

For comparison the room temperature results of Kloepfer et al. are listed in the 5th column of Table 5.5.[179, 181] The result for the decay time t_{pair} of the LCT agrees well with their result. The build-up time t_2 of the quasi-equilibrated *atom:electron* species was not reported by these authors. The value determined from the model for ΔG is somewhat greater than reported by Kloepfer et al. It should be noted that the investigated temperature dependence of the present work provides sensitive information on the attractive interaction of the pair. A significant difference in the analysis of Kloepfer et al. [181] is the very small value of the I–e^- distance of R_0 = 4 Å, as compared to the iodine–oxygen distance (3 Å)[194] and the radius of the first solvation shell of the electron (3.1 Å).[189]

5.5. Conclusion

The fs-broadband pump-probe study of the temperature dependent electron photodetachment in iodide solution shows several important points:

- The initially excited LCT state shows a broad absorption in the NIR with a maximum around 1000 nm at all three bulk temperatures. As concluded from the measured LCT relaxation the released electron escapes the anion solvation shell with a time constant t_1 = 220–180 fs going from 25 to 75 °C. The separation of the excess electron from the iodine atom and the assembling of a new solvation configuration take 700–540 fs in the mentioned temperature interval. To account for the two time constants two intermediates are introduced that are assigned to an *atom:electron* pair in a non-equilibrated solvation structure and a quasi-equilibrated, hydrated pair.

- The former precursor, $(I{:}e^-)_{non\text{-}eq}$ is characterized by an absorption spectrum centered at 825 nm that is only weakly affected by the temperature variation in the investigated range. The finding suggests that increasing the solution temperature the relaxation pathway remains unchanged. The absorption band of the second intermediate which appears within the first 2 ps cannot be distinguished from that of the solvated electron. It is assigned to a solvated *atom:electron* pair $(I{:}e^-)_{hyd}$. The subsequent slower dynamics indicated by an absorption

decrease is strongly temperature-dependent and explained by a competition between pair dissociation and geminate recombination.

- The relaxation dynamics is described by diffusion of the particles in the presence of an attractive interaction described by a Morse potential with depth of about 850 ± 100 cm^{-1}. The extracted full halfwidth of the potential well decreases from 2.6 Å at 25 °C to 2.0 Å at 75 °C.

6. Femtosecond circular dichroism spectroscopy

6.1. Introduction

Biological function results from the unique entanglement of structure and dynamics. Thus, any methodology that can probe both structural and dynamical properties of biopolymers will be valuable to understand how nature functions on the molecular level. Time-resolved spectroscopic methods are well suited to probe the dynamics of various molecular processes on time scales down to femtosecond.[195-197] Consequently, there is a variety of techniques using both linear and non-linear optical detection schemes to measure molecular dynamics in real-time. However, the structural details, including the direction, amplitude, and time-scale of functionally important motions in biomolecules are usually immeasurable in direct way.

Currently, x-ray diffraction and absorption, including synchrotron radiation have been used to study picosecond [198] transient structures in proteins. Ultrafast electron diffraction (UED) has emerged as a competitive technique to probe structural dynamics both on solid surfaces and in the gas phase.[199] Although, far less popular, ultrafast time-resolved circular dichroism spectroscopy is an additional method to obtain structural information about evolving molecular systems (e.g. a folding protein).[200, 201]

Circular dichroism spectroscopy has been widely applied as a tool in material sciences, chemistry, biology and physics.[202] Molecules, that are optically active (chiral) exhibit *circular dichroism* (CD), i.e. a difference in extinction for left- and right-circularly polarized light: $\Delta\varepsilon = \varepsilon_L - \varepsilon_R$. The CD effect originates from the fact that electric and magnetic transition dipole moments are not perpendicular to each other (which results in a helical net electron displacement during excitation). While chirality is necessary for observing a CD spectrum, the molecules (i.e. chromophores) do not have to be chiral to show a CD signal if they are spatially oriented to form a chiral array as typically found in biopolymers like folded proteins or nucleic

acids. The latter case is commonly described as exciton-coupled (EC) CD spectroscopy and has been advanced by Harada and Nakanishi.[203, 204]

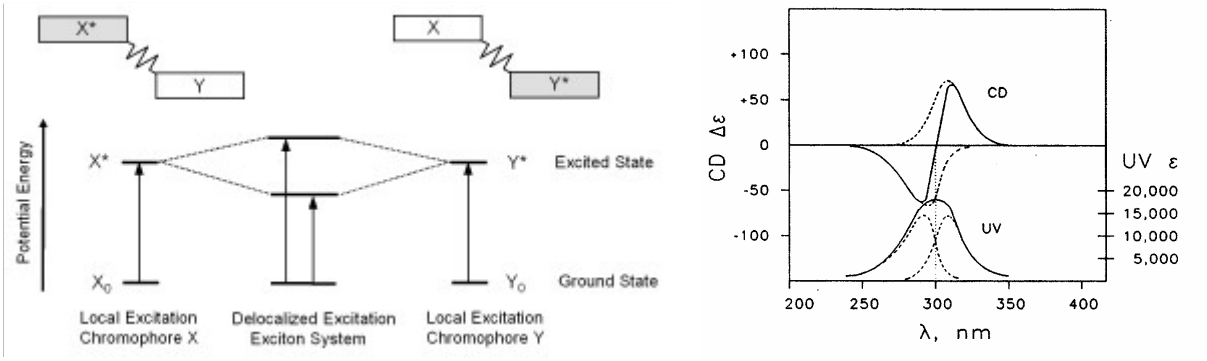

Figure 6.1. *Left: Basic interaction scheme between two chromophores. If the interaction between X and Y is negligible, the excitation will remain completely localized. If X and Y are coupled a delocalized exciton state will be formed. Right: The effect of the interaction on the absorption and CD spectrum. The figure is taken from Ref. [204]*

The observed signals depend strongly on the orientation of the chromophores to each other. To illustrate the principle of EC-CD one should consider two identical, achiral, weakly-coupled (dipole-dipole interaction) chromophores. As shown in Figure 6.1 the coupling of degenerate transitions on these chromophores will lead to two CD bands of opposite signs which are spectrally located slightly above and slightly below the transition of the isolated chromophore. If the interaction between the chromophores is time-dependent – due to structural dynamics in the system – The CD spectrum will also be time-dependent. In fact, it will depend on the relative orientation of the two chromophores to each other and the vector connecting them.

There are two main approaches utilized to measure CD spectra. In *ellipsometric* CD measurements the change in the ellipticity of a highly elliptically polarized light beam upon its passage through a circularly dichroic sample is detected. Any polarization state of light can be viewed as a superposition of circularly left and right polarization with certain amplitude and phase. Passing through dichroic (or birefringent) materials will induce changes of the relative amplitudes (and phase) of left and right circular polarization. Hence, the ellipticity of the input beam polarization is changed too. By measuring these changes for both left and right elliptically

polarized probe beams, it is possible to determine both the sign and magnitude of the CD. Although successfully applied in many nanosecond time-resolved CD measurements, the ellipsometric approach has inherent drawbacks.[200, 205] Any circular and linear birefringence of the sample, sample cell, or optical elements in the beam path can generate artifacts which could be on same order or even higher than the expected CD signal.

The second approach (which is used in modern commercial steady state CD spectrometers) is based on the *direct measurement of the differential absorption* of right and left circular polarized light, using polarization modulation and phase-locked detection techniques to increase the signal-to-noise ratio. The basic schematic of a CD instrument using this absorptive method is shown on Figure 6.2.

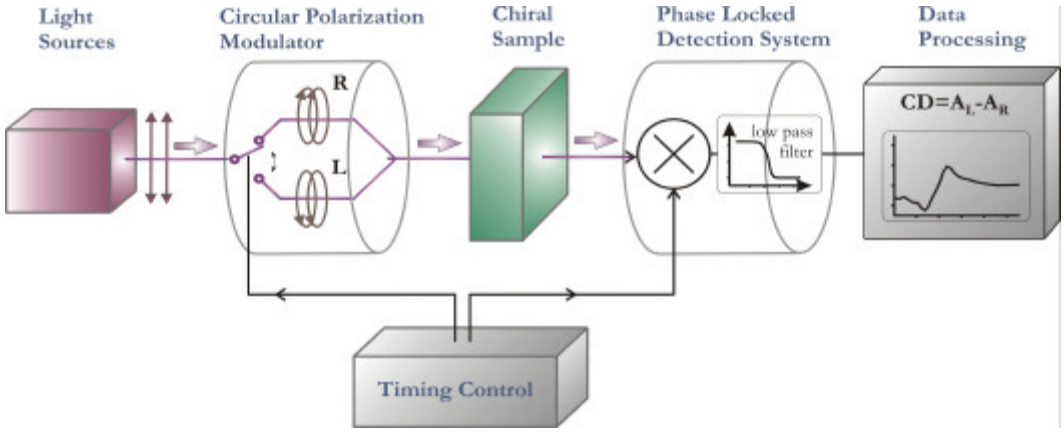

Figure 6.2. *A basic schematic of a CD instrument which measures directly the differential absorption of right and left circular polarized light.*

A monochromatic linearly polarized light beam passes through a piezo-optic modulator in which the polarization state of the beam is switched between right and left circular polarization. This modulated light beam is directed through a sample, and subsequently processed by a phase locked detector (referenced at the modulation frequency). Hence this technique eliminates the need for analyzing the polarization state of the beam after passing through the sample. As a result the direct absorptive approach is less prone to polarization artifacts. The implementation

of phase locked detection provides high signal-to-noise measurements, which is critical for using this approach since the differential absorptions are small (typically in the range of 0.01 to 0.1 mOD). On the other hand the time resolution of this method is limited to several periods of the modulation frequency. The current technology of photo-elastic and electro-optic modulators produces a limit for the time resolution which is in the millisecond and microsecond range, respectively. Therefore a main disadvantage of the described method is its technological restriction for ultrafast time resolved CD measurements.

The principle of time resolved CD spectroscopy is to measure CD spectra as a function of time after *rapid initiation* of the dynamics of interest.[202] Initial attempts of time resolved CD measurements used kinetic techniques such as stopped flow,[206] temperature jump,[207] and flash photolysis [208] measurements in combination with the standard absorptive CD technique. The time resolution of those instruments was limited to milliseconds or microsecond.

The existing methodology for picosecond time-resolved [200, 209] CD is closely related to conventional pump-probe detection schemes and can generally be extended to the femtosecond time range. There are two laser pulses (pump and probe) with a variable time delay between each other. The first pulse initiates a dynamical process (e.g. chemical reaction) by photoexciting a chromophore in the sample while the second pulse is probing the CD spectrum after the system has evolved in time. The probe laser beam is generated by a tunable picoseconds laser. Before entering the sample the probe beam polarization is modulated using an acousto-optical or electro-optical modulator just like in a conventional CD spectrometer (Fig. 6.2). In addition the modulator controls the Q-switch in the laser oscillator in a way that successive probe laser pulses only pass through the modulator when certain amplitudes for "+" "-"quarter wave retardation are being applied. The modulation frequency of the probe polarization is on the order of several hundred Hz.[200] This is about one order of magnitude slower than the pulse repetition rate of the tunable laser output.

This arrangement makes direct absorptive CD measurements at *fixed* wavelength feasible. Kinetics (i.e. time-dependent transient signals) are recorded by varying the time delay between

pump and probe pulse. Obtaining the entire CD spectrum requires the tuning of the wavelength of the probe laser beam over the whole spectral range of interest. This procedure is complicated, laborious and simply impractical for broadband CD detection. In this respect monitoring the temporal evolution of the CD signal simultaneously over the entire spectral range would provide a more complete data set for the CD dynamics which in turn would allow a more detailed interpretation of the CD measurements in terms of structural and conformational changes.

6.2. Generation and characterization of circularly polarized white light continuuum

From the earliest years of WLG has been discovered it was believed that the polarization is the same as that of incident laser pulse. Until now investigations of polarization state of WLG are made either integrally over the whole spectrum [210] or only over a very narrow spectral range close to the pump wavelength.[211] However, the amplitude dynamic range of WLG signal is changed by several orders of magnitude along the spectrum. This may lead to a fallacy in the characterization of white-light polarization properties. For instance, the broad blue-shifted wing - which is of most practical use - has an amplitude of several order of magnitude smaller (10^{-3}, 10^{-4}) than the amplitude around the seed wavelength.

The clarification of the spectral distribution of the polarization state of the WLG is a crucial point for the proposed new technology of broadband fs-CD spectroscopy. In addition it will have a profound impact on the applications of the WLG as a tool for other femtosecond spectroscopic techniques.

The preliminary results provide a new insight into the polarization phenomena occurring upon WL generation in isotropic condensed media. In the cases of linear and circular polarization of the incident laser beam one can observe that in certain spectral regions of the generated continuum the polarization state is preserved whereas for other spectral regions the continuum does not inherit the seed pulse polarization. It is determined that there is an optimum in the energy of the incident beam at which the intensity and the degree of preservation of the polarization in the region of the blue shifted spectrum reach their maximum.

A schematic of the white-light continuum generator (WLG) and experimental setup is shown in Figure 6.3. It is based on the experimental setup described in details in section 2.1.2. The polarization state of the input beam and the WL is controlled by Glan polarizers PG1, PG2 and quarter retardations wave plates QR1 and QR2 respectively. Monitoring of the output WL spectra is done with the commercial fiber coupled spectrograph and pico-joule energy meter.

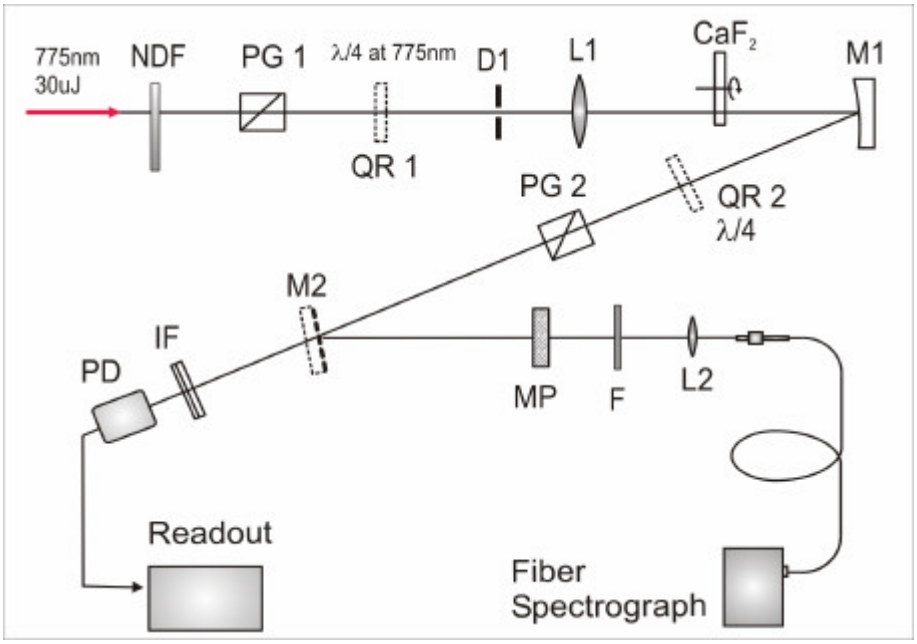

Figure 6.3. *Schematic representation of the optical setup for white light continuum generation and characterization.*

In order to measure the WL intensity more precisely in the spectral area where its intensity is three to five orders of magnitude lower a high-pass filter F is used. It reduces the spectral intensity around the input pulse wavelength. The white light spectrum is characterized by a relatively symmetric broadening of 2000-3000 cm^{-1} around the seed pulse wavelength, and a broad blue shifted pedestal with a relatively constant intensity (Fig. 6.4, inset). The blue cut-off wavelength depends on the material.[212] For the used CaF_2 crystal, pumped at 775 nm the spectrum covers the range down to 320 nm.

The polarization properties of WL in the case of circular polarized input pulses are observed when the zero-order quarter waveplate at 775 nm – QR1 was placed after the polarizer PG1. The plate is oriented so that the beam after it is precisely circularly polarized.

The measured degree of preservation of the circular polarization is determined by the degree to which the zero-order quarter waveplate QR2 can transform the WL polarization back to linear polarization. The passed through QR2 continuum light is analyzed using a second calcite Glan-Taylor polarization prism PG2. Measured are the two orthogonal components – parallel polarized intensity $I_{PAR}(l)$ and perpendicular polarized intensity $I_{PERP}(l)$ when PG2 is oriented parallel and perpendicular to PG1 respectively. The obtained wavelength dependent polarization ratio is defined as $r(l) = I_{PAR}(l)/I_{PERP}(l)$ and is shown in Figure 6.4.

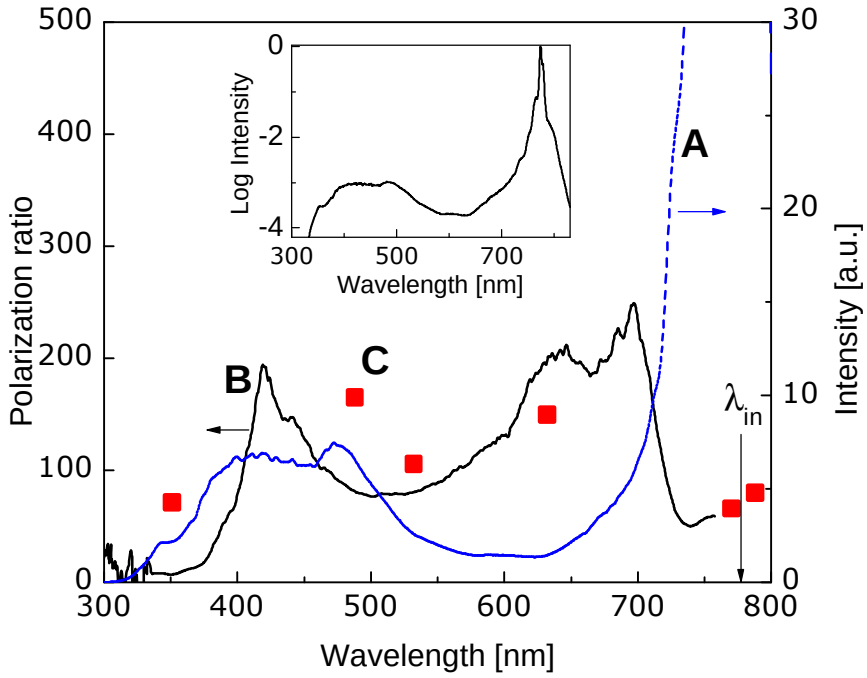

Figure 6.4. *Spectrum (**A**) and polarization ratio (**B**) of white-light continuum generated with circularly polarized pump pulses. The insets show the entire spectra in logarithmic scale. The red squares (**C**) represent the polarization ratio of the WLC obtained by using a zero-order* $l/4$ *plates and corresponding interference bandpass filters at 351, 488, 532, 628, 770 and 788nm.*

The red squares represent the measured values of $r(l)$ when quarter zero-order wave plates at selected wavelengths are used. For all six wavelengths a corresponding bandpass interference

filter is used and the relative intensities are measured by the pJ meter. The black solid line in Figure 6.4 shows the outcome when a broad band quarter wave plate in the 460-650 nm region is used. The deterioration of the circular polarization degree of preservation of the generated continuum on the edge of the blue shifted wing is mostly due to the deterioration of the quarter wave plate properties.

6.3. A new methodology for transient circular dichroism measurement

In this chapter the focus is placed on design and construction of a broadband femtosecond time-resolved circular dichroism spectrometer with the capability of simultaneously acquiring data over a large spectral region (ultraviolet to near infrared).

A schematic of the designed femtosecond white light based CD spectrometer is shown on Figure 6.5. It is based on the pump-probe transient spectrometer described in section 2.1. The main difference is introducing polarization control in the femtosecond white light generator. The The key function of the WLG is to perform a computer-controlled switching between left and right circular polarization of the WL. This is achieved by controlling the polarization of the input seed laser pulse using an electro-optical modulator. As a modulator is used a plane-parallel longitudinal Pockels Cell (PKC) made of a DKDP optical crystal. In this scheme, it alternates between plus/minus quarter wave of retardation of a linear polarized input beam by applying a high voltage on cell electrodes. The high voltage switch supplies externally synchronized bipolar voltage swings in the kilovolt range on PKC electrodes. The precision of the output voltage determines the precision of the polarization state of the generated WL and therefore the "polarizational resolution" of the measurement.

The voltage exhibits a very steep slope with a subsequent plateau and the frequency of modulation may be varied and it considerably lower than the repetition rate of the femtosecond pulses of the probe which is 1 kHz. The optical shutter system consists of a shutter and controller and is synchronized with the high voltage pulses. Consequently, it is possible to use an approach of noise reduction, similar to the one used in the pump-probe transient absorption

measurements described in section 2.1.3. Distinctive features of the new detection method are: First, each measurement cycle has two phases which only differ in the polarization of the probe beam. Second, choosing a modulation frequency for the polarization which is smaller than the repetition rate of the laser pulses permits many pump/probe pulses per modulation cycle.

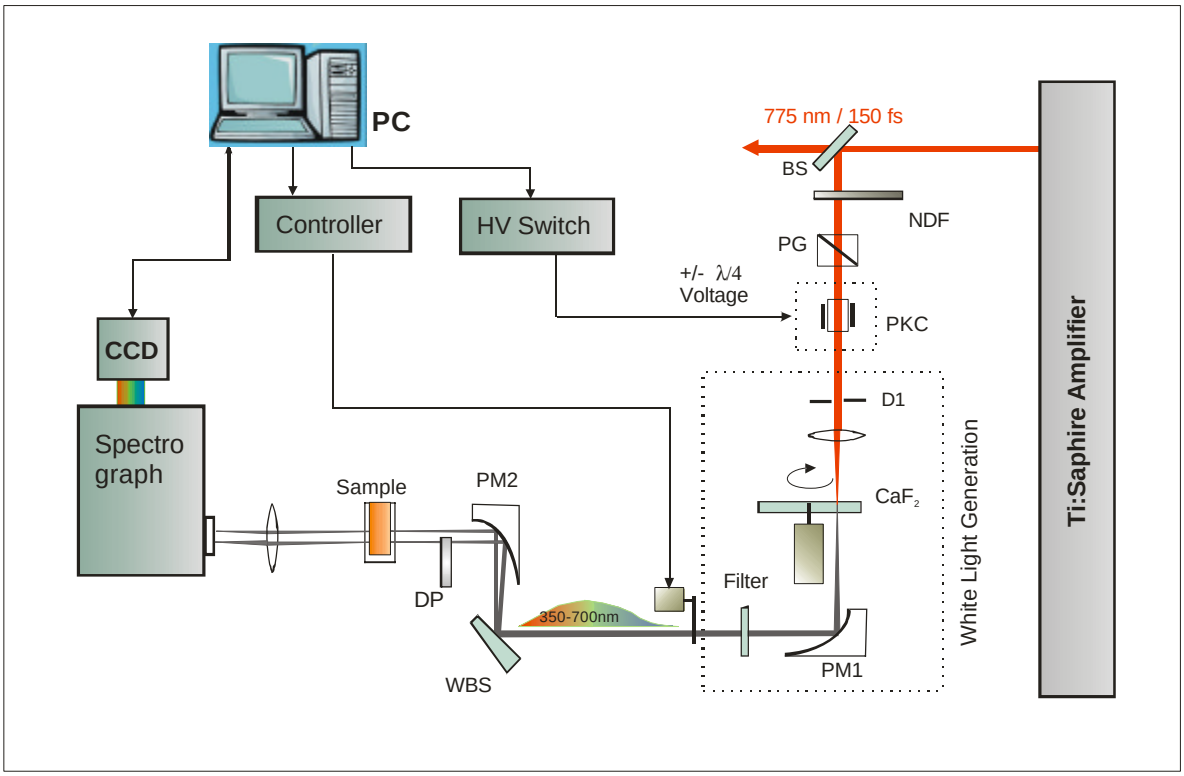

Figure 6.5. *Shematic layout of the broadband circular dichroism spectrometer.*

The digital lock-in detection made possible with this arrangement improves the signal-to-noise ratio substantially; Third, a two probe beam geometry has to be used to eliminate the artifacts caused by the birefringence and dichroism of the optical elements in the optical path of the probe beam. Using the beamsplitter WBS the probe beam is split into two approximately equal beams (channels) before entering the sample. Both optical beams pass through the optically active volume of the sample. The polarization of the second (reference) beam has to be "scrambled". This is accomplished by using an calcite polarization scrambler DP. The consequent detection and processing of the signals are identical of these, described in chapter 2. The recorded signals at each step will result from averaging, typically for several 100 laser pulses.

6.4. Implementation of femtosecond white light for steady state CD measurements.

Finally, shown is a comparison between the steady state CD spectrum of optically pure Λ - enantiomer of $[Ru(bpy)_3]PF_6$ solution in acetonitrile obtained with the prototype setup to the corresponding CD spectrum measured by a commercial spectrometer (Fig. 6.6).

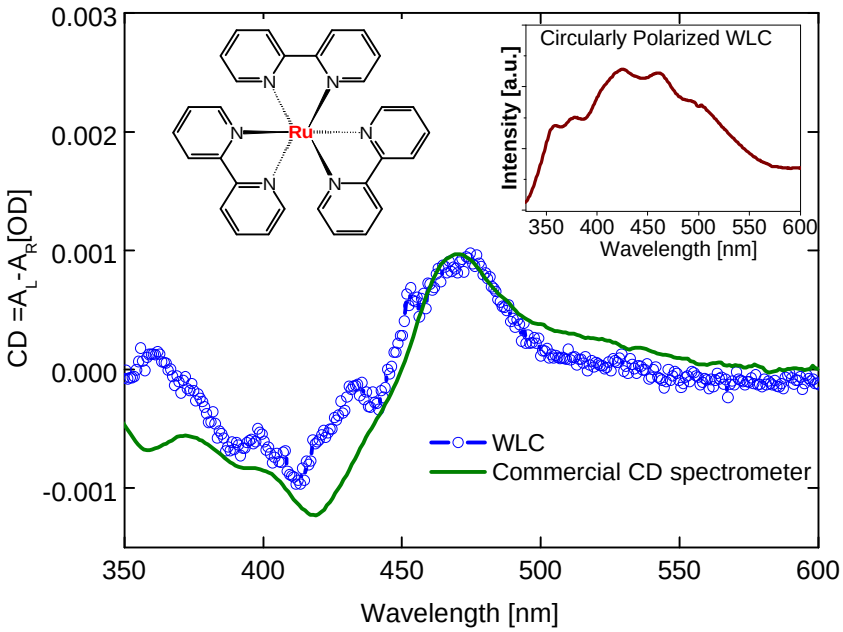

Figure 6.6. *Comparison of the steady state CD spectrum of optically pure Λ - $[Ru(bpy)_3]^{2+}$: The preliminary results vs. the spectrum obtained with commercial CD spectrometer (Jasco).*

The preliminary results clearly document that polarization control acrros a broad fs-white light spectrum is technically possible. Further steps to optimize the signal-to-noise ratio are currently being undertaken. First attempts to measure time-dependent excited state CD spectra will be starting shortly in the new laboratory of Prof. Fiebig at Boston College.

References

[1] Martinez, O. E.; Gordon, J. P.; Fork, R. L. *Opt. Lett.*, **1984**, *1*, 1003.

[2] Wurzer, A. J.; Lochbrunner, S.; Riedle, E. *Appl. Phys. B*, **2000**, *71*, *3*, 405-409.

[3] Albrecht, T. F.; Seibert, K.; Kurz, H. *Opt. Commun.*, **1991**, *84*, *5-6*, 223-227.

[4] Tokunaga, E.; Terasaki, A.; Kobayashi, T. *Opt. Lett.*, **1993**, *18*, 370.

[5] Fork, R. L.; Shank, C. V.; Hirlimann, C.; Yen, R.; Tomlinson, W. J. *Opt. Lett.*, **1983**, *8*, 1.

[6] Kovalenko, S. A.; Dobryakov, A. L.; Ruthmann, J.; Ernsting, N. P. *Phys. Rev. A*, **1999**, *59*, 2369.

[7] Ekvall, K.; Meulen, P. v. d.; Dhollande, C.; Berg, L.-E.; Pommeret, S.; Naskrecki, R.; Mialocq, J.-C. *J. Appl. Phys.*, **2000**, *87*, *5*, 2340-2352.

[8] Lorenc, M.; Ziolek, M.; Naskrecki, R.; Karolczak, J.; Kubicki, J.; Maciejewski, A. *Appl. Phys. B*, **2002**, *74*, *1*, 19-27.

[9] Raytchev, M.; Pandurski, E.; Buchvarov, I.; Modrakowski, C.; Fiebig, T. *J. Phys. Chem. A*, **2003**, *107*, 4592-4600.

[10] Kelley, S. O.; Barton, J. K. *Science*, **1999**, *283*, *5400*, 375-381.

[11] Nordlund, T. M.; Andersson, S.; Nilsson, L.; Rigler, R.; Graslund, A.; McLaughlin, L. W. *Biochemistry*, **1989**, *28*, *23*, 9095-9103.

[12] Sowers, L. C.; Fazakerley, G. V.; Eritja, R.; Kaplan, B. E.; Goodman, M. F. *Proc. Natl. Acad. Sci. USA*, **1986**, *83*, *15*, 5434-5438.

[13] McLaughlin, L. W.; Feong, T.; Benseler, F.; Piel, N. *Nucleic Acids Res.*, **1988**, *16*, 5631-5644.

[14] Broo, A. *J. Phys. Chem. A*, **1998**, *102*, *3*, 526-531.

[15] Nikolov, I.; Popmintchev, T.; Trifonov, A.; Buchvarov, I. *Proc. of SPIE*, **2002**, *5226.*

[16] Honninger, C.; Paschotta, R.; Morier-Genoud, F.; Moser, M.; Keller, U. *J. Opt. Soc. Am. B*, **1999**, *16*, *1*, 46-56.

[17] Agnesi, A.; Pennacchio, C.; Reali, G. C.; Kubecek, V. *Opt. Lett.*, **1997**, *22*, *21*, 1645-1647.

[18] Magni, V. *Appl. Optics*, **1986**, *25*, *1*, 107-117.

[19] Hua, R. Z.; Wada, S.; Tashiro, H. *Appl. Optics*, **2001**, *40*, *15*, 2468-2474.

[20] Cerullo, G.; Desilvestri, S.; Monguzzi, A.; Segala, D.; Magni, V. *Opt. Lett.*, **1995**, *20*, *7*, 746-748.

[21] Couderc, V.; Louradour, F.; Barthelemy, A. *Opt. Commun.*, **1999**, *166*, 103-111.

[22] Keller, U.; Weingarten, K. J.; Kartner, F. X.; Kopf, D.; Braun, B.; Jung, I. D.; Fluck, R.; Honninger, C.; Matuschek, N.; derAu, J. A. *IEEE J. Sel. Top. Quantum Electron.*, **1996**, *2*, *3*, 435-453.

[23] Laporta, P.; Brussard, M. *IEEE J. Quantum Electron.*, **1991**, *27*, *10*, 2319-2326.

[24] Chen, Y. F.; Liao, T. S.; Kao, C. F.; Huang, T. M.; Lin, K. H.; Wang, S. C. *IEEE J. Quantum Electron.*, **1996**, *32*, *11*, 2010-2016.

[25] Innocenzi, M. E.; Yura, H. T.; Fincher, C. L.; Fields, R. A. *Appl. Phys. Lett.*, **1990**, *56*, *19*, 1831-1833.

[26] Agnesi, A.; Dell'Acqua, S.; Reali, G. C.; Gobbi, P. G.; Ragazzi, D. *Appl. Optics*, **1997**, *36*, *3*, 597-601.

[27] Kogelnik, H.; Li, T. *Appl. Optics*, **1966**, *5*, *10*, 1550.

[28] Stankov, K. A.; Jethwa, J. *Opt. Commun.*, **1988**, *66*, *1*, 41-46.

[29] Stankov, K. A. *Appl. Phys. Lett.*, **1991**, *58*, *20*, 2203-2204.

[30] Mayer, J. M. *Annu. Rev. Phys. Chem.*, **2004**, *55*, 363-390.

[31] Pal, S. K.; Zewail, A. H. *Chem. Rev.*, **2004**, *104*, *4*, 2099-2123.

[32] Waluk, J. *Acc. Chem. Res.*, **2003**, *36*, *11*, 832-838.

[33] Chang, C. J.; Chang, M. C. Y.; Damrauer, N. H.; Nocera, D. G. *Biochim. Biophys. Acta-Bioenerg.*, **2004**, *1655*, *1-3*, 13-28.

[34] Okamura, M. Y.; Paddock, M. L.; Graige, M. S.; Feher, G. *Biochim. Biophys. Acta-Bioenerg.*, **2000**, *1458*, *1*, 148-163.

[35] Cukier, R. I. *J. Phys. Chem.*, **1996**, *100*, 15428-15443.

[36] Cukier, R. I.; Nocera, D. G. *Annu. Rev. Phys. Chem.*, **1998**, *49*, 337-369.

[37] Amann, N.; Pandurski, E.; Fiebig, T.; Wagenknecht, H.-A. *Angew. Chem.-Int. Edit.*, **2002**, *41*, 2978-2980.

[38] Steenken, S. *Biol. Chem.*, **1997**, *378*, *11*, 1293-1297.

[39] Huber, R.; Fiebig, T.; Wagenknecht, H.-A. *Chem. Commun.*, **2003**, *15*, 1878-1879.

[40] Raytchev, M.; Mayer, E.; Amann, N.; Wagenknecht, H.-A.; Fiebig, T. *ChemPhysChem*, **2004**, *5*, *5*, 706-712.

[41] Kaden, P.; Mayer, E.; Trifonov, A.; Fiebig, T.; Wagenknecht, H.-A. *Angew. Chem.-Int. Edit.*, **2005**, *44*, *11*, 1637-1639.

[42] Paris, P. L.; Langenhan, J. M.; Kool, E. T. *Nucleic Acids Res.*, **1998**, *26*, *16*, 3789-3793.

[43] Netzel, T. L.; Zhao, M.; Nafisi, K.; Headrick, J.; Sigman, M. S.; Eaton, B. E. *J. Am. Chem. Soc.*, **1995**, *117*, 9119-9128.

[44] Netzel, T. L.; Nafisi, K.; Headrick, J.; Eaton, B. E. *J. Phys. Chem.*, **1995**, *99*, 17948-17955.

[45] Giese, B. *Annu. Rev. Biochem.*, **2002**, *71*, 51-70.

[46] Amann, N.; Pandurski, E.; Fiebig, T.; Wagenknecht, H.-A. *Chem. Eur. J.*, **2002**, *8*, *21*, 4877-4883.

[47] Kubota, T.; Kano, K.; Konse, T. *Bull. Chem. Soc. Jpn.*, **1987**, *60*, 3865-3877.

[48] Fiebig, T.; Wan, C.; Zewail, A. H. *ChemPhysChem*, **2002**, *3*, *9*, 781-788.

[49] Ottolenghi, M. *Acc. Chem. Res.*, **1973**, *6*, *5*, 153-160.

[50] Pandurski, E.; Fiebig, T. *Chem. Phys. Lett.*, **2002**, *357*, 272-278.

[51] Post, M. F. M.; Langelaar, J.; Voorst, J. D. W. V. *Chem. Phys. Lett.*, **1971**, *10*, *4*, 468-472.

[52] Mank, D.; Raytchev, M.; Amthor, S.; Lambert, C.; Fiebig, T. *Chem. Phys. Lett.*, **2003**, *376*, *1-2*, 201-206.

[53] Steenken, S. *Free Radic. Res. Commun.*, **1992**, *16*, *6*, 349-379.

[54] Eigen, M. *Angew. Chem.-Int. Edit.*, **1964**, *3*, *1*, 1-19.

[55] Wagenknecht, H.-A. *Angew. Chem.-Int. Edit.*, **2003**, *42*, *22*, 2454-2460.

[56] Reviews:. *Top. Curr. Chem.*, **2004**, *236 and 237*.

[57] Cai, Z. L.; Sevilla, M. D. *Top. Curr. Chem.*, **2004**, *237*, 103-127.

[58] Haas, C.; Kraling, K.; Cichon, M.; Rahe, N.; Carell, T. *Angew. Chem.-Int. Edit.*, **2004**, *43*, *14*, 1842-1844.

[59] Giese, B.; Carl, B.; Carl, T.; Carell, T.; Behrens, C.; Hennecke, U.; Schiemann, O.; Feresin, E. *Angew. Chem.-Int. Edit.*, **2004**, *43*, *14*, 1848-1851.

[60] Ito, T.; Rokita, S. E. *Angew. Chem.-Int. Edit.*, **2004**, *43*, *14*, 1839-1842.

[61] Lewis, F. D.; Liu, X.; Miller, S. E.; Hayes, R. T.; Wasielewski, M. R. *J. Am. Chem. Soc.*, **2002**, *124*, 11280-11281.

[62] Wagner, C.; Wagenknecht, H.-A. *Chem.-Eur. J.*, **2005**, *11*, *6*, 1871-1876.

[63] Wan, C.; Fiebig, T.; Kelley, S. O.; Treadway, C. R.; Barton, J. K.; Zewail, A. H. *Proc. Natl. Acad. Sci. USA*, **1999**, *96*, 6014-6019.

[64] Berlin, Y. A.; Burin, A. L.; Siebbeles, L. D. A.; Ratner, M. A. *J. Phys. Chem. A*, **2001**, *105*, *23*, 5666 – 5678.

[65] Renger, T.; Marcus, R. A. *J. Phys. Chem. A*, **2003**, *107*, *41*, 8404-8419.

[66] O'Neill, M. A.; Becker, H. C.; Wan, C. Z.; Barton, J. K.; Zewail, A. H. *Angew. Chem.-Int. Edit.*, **2003**, *42*, *47*, 5896-5900.

[67] O'Neill, M. A.; Barton, J. K. *J. Am. Chem. Soc.*, **2004**, *126*, *41*, 13234-13235.

[68] Rivera, E.; Schuler, R. H. *J. Phys. Chem.*, **1983**, *87*, *20*, 3966-3971.

[69] Sugiyama, H.; Tsutsumi, Y.; Saito, I. *J. Am. Chem. Soc.*, **1990**, *112*, *18*, 6720-6721.

[70] Cook, G. P.; Greenberg, M. M. *J. Am. Chem. Soc.*, **1996**, *118*, *42*, 10025-10030.

[71] Tashiro, R.; Sugiyama, H. *J. Am. Chem. Soc.*, **2003**, *125*, *50*, 15282-15283.

[72] Steenken, S.; Telo, J. P.; Novais, H. M.; Candeias, L. P. *J. Am. Chem. Soc.*, **1992**, *114*, 4701-4709.

[73] Mayer, E.; Valis, L.; Huber, R.; Amann, N.; Wagenknecht, H.-A. *Synthesis*, **2003**, *15*, 2335-2340.

[74] Alam, T. M.; Drobny, G. P. *Chem. Rev.*, **1991**, *91*, 1545-1590.

[75] Perkins, T. T.; Smith, D. E.; Chu, S. *Science*, **1994**, *264*, *5160*, 819-822.

[76] Gmeiner, W. H. *Curr. Med. Chem.*, **1998**, *5*, *2*, 115-135.

[77] Naimushin, A. N.; Fujimoto, B. S.; Schurr, J. M. *Biophys. J.*, **2000**, *78*, *3*, 1498-1518.

[78] Schuster, G. B. *Acc. Chem. Res.*, **2000**, *33*, 253-260.

[79] Smith, B. L. *Prog. Biophys. Mol. Biol.*, **2000**, *74*, *1-2*, 93-113.

[80] O'Neill, M. A.; Barton, J. K. *J. Am. Chem. Soc.*, **2002**, *124*, *44*, 13053-13066.

[81] Bansal, M. *Curr. Sci.*, **2003**, *85*, 1556.

[82] Millar, D. P. *Curr. Opin. Struct. Biol.*, **1996**, *6*, *3*, 322-326.

[83] Balakin, K. V.; Korshun, V. A.; Mikhalev, II; Maleev, G. V.; Malakhov, A. D.; Prokhorenko, I. A.; Berlin, Y. A. *Biosens. Bioelectron.*, **1998**, *13*, *7-8*, 771-778.

[84] Okonogi, T.; Reese, A. W.; Alley, S. C.; Hopkins, P. B.; Robinson, B. H. *Biophys. J.*, **1999**, *77*, *6*, 3256-3276.

[85] Shipway, A. N.; Willner, I. *Chem. Commun.*, **2001**, *20*, 2035-2045.

[86] Sponer, J.; Leszczynski, J.; Hobza, P. *Biopolymers*, **2001**, *61*, *1*, 3-31.

[87] Cui, D. X.; Gao, H. J. *Biotechnol. Prog.*, **2003**, *19*, 683.

[88] Robertson, N.; McGowan, C. A. *Chem. Soc. Rev.*, **2003**, *32*, *2*, 96-103.

[89] Endres, R. G.; Cox, D. L.; Singh, R. R. P. *Rev. Mod. Phys.*, **2004**, *76*, *1*, 195-214.

[90] Gao, H. J.; Kong, Y. *Ann. Rev. Mater. Res.*, **2004**, *34*, 123-150.

[91] Iguchi, K. *Int. J. Mod. Phys. B*, **2004**, *18*, *13*, 1845-1910.

[92] Cheatham, I., Thomas E. *Curr. Opin. Struct. Biol.*, **2004**, *14*, *3*, 360-367.

[93] Somoza, M. M.; Andreatta, D.; Murphy, C. J.; Coleman, R. S.; Berg, M. A. *Nucleic Acids Res.*, **2004**, *32*, *8*, 2494-2507.

[94] Brauns, E. B.; Madaras, M. L.; Coleman, R. S.; Murphy, C. J.; Berg, M. A. *J. Am. Chem. Soc.*, **1999**, *121*, *50*, 11644-11649.

[95] Brauns, E. B.; Madaras, M. L.; Coleman, R. S.; Murphy, C. J.; Berg, M. A. *Phys. Rev. Lett.*, **2002**, *88*, *15*, 158101.

[96] Dioubankova, M. N.; Malakhov, A. D.; Stetsenko, D. A.; Gait, M. J.; Volynsky, P. E.; Efremov, R. G.; Korshun, V. A. *Chembiochem*, **2003**, *4*, *9*, 841-847.

[97] Yamana, K.; Takei, M.; Nakano, H. *Tetrahedron Lett.*, **1997**, *38*, *34*, 6051-6054.

[98] Christensen, U. B.; Pedersen, E. B. *Helv. Chim. Acta*, **2003**, *86*, *6*, 2090-2097.

[99] Lewis, F. D.; Zhang, Y. F.; Letsinger, R. L. *J. Am. Chem. Soc.*, **1997**, *119*, *23*, 5451-5452.

[100] Hrdlicka, P. J.; Babu, B. R.; Sorensen, M. D.; Wengel, J. *Chem. Commun.*, **2004**, *13*, 1478-1479.

[101] Korshun, V. A.; Pestov, N. B.; Birikh, K. R.; Berlin, Y. A. *Bioconjugate Chem.*, **1992**, *3*, *6*, 559-562.

[102] Kool, E. T. *Chem. Rev.*, **1997**, *97*, *5*, 1473-1487.

[103] Beuck, C.; Singh, I.; Bhattacharya, A.; Heckler, W.; Parmar, V. S.; Seitz, O.; Weinhold, E. *Angew. Chem.-Int. Edit.*, **2003**, *42*, *33*, 3958-3960.

[104] Okamoto, A.; Ochi, Y.; Saito, I. *Chem. Commun.*, **2005**, *9*, 1128-1130.

[105] Prokhorenko, I. A.; Korshun, V. A.; Petrov, A. A.; Gontarev, S. V.; Berlin, Y. A. *Bioorg. Med. Chem. Lett.*, **1995**, *5*, *18*, 2081-2084.

[106] Korshun, V. A.; Balakin, K. V.; Proskurina, T. S.; Mikhalev, II; Malakhov, A. D.; Berlin, Y. A. *Nucleos. Nucleot.*, **1999**, *18*, *11-12*, 2661-2676.

[107] Mann, J. S.; Shibata, Y.; Meehan, T. *Bioconjugate Chem.*, **1992**, *3*, *6*, 554-558.

[108] Manoharan, M.; Tivel, K. L.; Zhao, M.; Nafisi, K.; Netzel, T. L. *J. Phys. Chem.*, **1995**, *99*, *48*, 17461-17472.

[109] Netzel, T. L.; Nafisi, K.; Zhao, M.; Lenhard, J. R.; Johnson, I. *J. Phys. Chem.*, **1995**, *99*, *51*, 17936-17947.

[110] Hwang, G. T.; Seo, Y. J.; Kim, B. H. *J. Am. Chem. Soc.*, **2004**, *126*, *21*, 6528-6529.

[111] Thoresen, L. H.; Jiao, G. S.; Haaland, W. C.; Metzker, M. L.; Burgess, K. *Chem.-Eur. J.*, **2003**, *9*, *19*, 4603-4610.

[112] Hurley, D. J.; Tor, Y. *J. Am. Chem. Soc.*, **2002**, *124*, *44*, 13231-13241.

[113] Jiao, G. S.; Kim, T. G.; Topp, M. R.; Burgess, K. *Org. Lett.*, **2004**, *6*, *11*, 1701-1704.

[114] Rist, M.; Amann, N.; Wagenknecht, H.-A. *Org. Chem Eur. J.*, **2003**, *13*, 2498-2504.

[115] Barnes, T. W.; Turner, D. L. H. *J. Am. Chem. Soc.*, **2001**, *123*, *37*, 9186-9187.

[116] Znosko, B. M.; Barnes, T. W.; Krugh, T. R.; Turner, D. H. *J. Am. Chem. Soc.*, **2003**, *125*, *20*, 6090-6097.

[117] Freier, S. M.; Altmann, K. H. *Nucleic Acids Res.*, **1997**, *25*, *22*, 4429-4443.

[118] Demesmaeker, A.; Haner, R.; Martin, P.; Moser, H. E. *Acc. Chem. Res.*, **1995**, *28*, *9*, 366-374.

[119] Mayer, E.; Valis, L.; Wagner, C.; Rist, M.; Amann, N.; Wagenknecht, H.-A. *Chembiochem*, **2004**, *5*, *6*, 865-868.

[120] Barbara, P.; Jarzeba, W. In *Advances in Photochemistry*, Klaus Gollnick, ed.; Wiley, **1990**; Vol. *15*, pp. 1.

[121] Maroncelli, M. *J. Mol. Liq.*, **1993**, *57*, 1-37.

[122] Lambert, C.; Schelter, J.; Fiebig, T.; Mank, D.; Trifonov, A. *J. Am. Chem. Soc.*, **2005**, *in press.*

[123] Lambert, C.; Noll, G.; Schelter, J. *Nature Materials*, **2002**, *1*, *1*, 69-73.

[124] Lambert, C.; Noll, G. *Chem.-Eur. J.*, **2002**, *8*, *15*, 3467-3477.

[125] Lambert, C.; Noll, G. *J. Am. Chem. Soc.*, **1999**, *121*, *37*, 8434-8442.

[126] Lambert, C.; Amthor, S.; Schelter, J. *J. Phys. Chem. A*, **2004**, *108*, *31*, 6474-6486.

[127] Zhao, H. D.; Tanjutco, C.; Thayumanavan, S. *Tetrahedron Lett.*, **2001**, *42*, *27*, 4421-4424.

[128] Fujikawa, H.; Tokito, S.; Taga, Y. *Synth. Met.*, **1999**, *91*, 161-162.

[129] Thayumanavan, S.; Barlow, S.; Marder, S. R. *Chem. Mater.*, **1997**, *9*, *12*, 3231-3235.

[130] Koene, B. E.; Loy, D. E.; Thompson, M. E. *Chem. Mater.*, **1998**, *10*, *8*, 2235-2250.

[131] Weiss, D. S.; Cowdery, J. R.; Young, R. H. *Wiley-VCH: Weinheim*, **2001**, *5*, 379-471.

[132] Thelakkat, M. *Macromol. Mater. Eng.*, **2002**, *287*, *7*, 442-461.

[133] Lambert, C.; Noll, G. *Synth. Met.*, **2003**, *139*, *1*, 57-62.

[134] Lambert, C.; Noll, G.; Hampel, F. *J. Phys. Chem. A*, **2001**, *105*, *32*, 7751-7758.

[135] Lambert, C.; Noll, G.; Zabel, M.; Hampel, F.; Schmalzlin, E.; Brauchle, C.; Meerholz, K. *Chem.-Eur. J.*, **2003**, *9*, *17*, 4232-4239.

[136] Bonvoisin, J.; Launay, J. P.; Verbouwe, W.; VanderAuweraer, M.; DeSchryver, F. C. *J. Phys. Chem.*, **1996**, *100*, *42*, 17079-17082.

[137] Bonvoisin, J.; Launay, J. P.; Vanderauweraer, M.; Deschryver, F. C. *J. Phys. Chem.*, **1994**, *98*, *19*, 5052-5057.

[138] Wienk, M. M.; Janssen, R. A. J. *J. Am. Chem. Soc.*, **1997**, *119*, *19*, 4492-4501.

[139] Blackstock, S. C.; Selby, T. D. In *Magnetic Properties of Organic Materials*, P. M Lahti, ed.; Marcel Dekker: New York, **1999**, pp. 165-178.

[140] Bushby, R. J. In *Magnetism Molecules to Materials, II*, Drillon M., ed.; Wiley-VCH: Weinheim, Germany, **2001**, pp. 149-187.

[141] Hauck, S. I.; Lakshmi, K. V.; Hartwig, J. F. *Org. Lett.*, **1999**, *1*, *13*, 2057-2060.

[142] Ito, A.; Urabe, M.; Tanaka, K. *Angew. Chem.-Int. Edit.*, **2003**, *42*, *8*, 921-+.

[143] Michinobu, T.; Takahashi, M.; Tsuchida, E.; Nishide, H. *Chem. Mater.*, **1999**, *11*, *8*, 1969-+.

[144] Selby, T. D.; Blackstock, S. C. *Org. Lett.*, **1999**, *1*, *13*, 2053-2055.

[145] Selby, T. D.; Blackstock, S. C. *J. Am. Chem. Soc.*, **1999**, *121*, *30*, 7152-7153.

[146] Selby, T. D.; Stickley, K. R.; Blackstock, S. C. *Org. Lett.*, **2000**, *2*, *2*, 171-174.

[147] Stickley, K. R.; Blackstock, S. C. *J. Am. Chem. Soc.*, **1994**, *116*, *25*, 11576-11577.

[148] Stickley, K. R.; Blackstock, S. C. *Tetrahedron Lett.*, **1995**, *36*, *10*, 1585-1588.

[149] Selby, T. D.; Kim, K. Y.; Blackstock, S. C. *Chem. Mater.*, **2002**, *14*, *4*, 1685-1690.

[150] Kim, K. Y.; Hassenzahl, J. D.; Selby, T. D.; Szulczewski, G. J.; Blackstock, S. C. *Chem. Mater.*, **2002**, *14*, *4*, 1691-1694.

[151] Plater, M. J.; Jackson, T. *Tetrahedron*, **2003**, *59*, *25*, 4687-4692.

[152] Ohsawa, Y.; Ishikawa, M.; Miyamoto, T.; Murofushi, Y.; Kawai, M. *Synth. Met.*, **1987**, *18*, *1-3*, 371-374.

[153] Louie, J.; Hartwig, J. F.; Fry, A. J. *J. Am. Chem. Soc.*, **1997**, *119*, *48*, 11695-11696.

[154] Katsuma, K.; Shirota, Y. *Adv. Mater.*, **1998**, *10*, *3*, 223.

[155] Wu, I. Y.; Lin, J. T.; Tao, Y. T.; Balasubramaniam, E. *Adv. Mater.*, **2000**, *12*, *9*, 668-+.

[156] Chen, C. H.; Shi, J.; Tang, C. W. *Macromol. Symp.*, **1997**, *125*, Jan-48.

[157] Selby, T. D.; Blackstock, S. C. *J. Am. Chem. Soc.*, **1998**, *120*, *46*, 12155-12156.

[158] Bronk, K.; Thayumanavan, S. *J. Org. Chem.*, **2003**, *68*, *14*, 5559-5567.

[159] Eberson, L. *Springer: Berlin (Germany)*, **1987**.

[160] Lin, B. C.; Cheng, C. P.; Lao, Z. P. M. *J. Phys. Chem. A*, **2003**, *107*, *26*, 5241-5251.

[161] Herbich, J.; Kapturkiewicz, A. *J. Am. Chem. Soc.*, **1998**, *120*, *5*, 1014-1029.

[162] Lambert, C.; Noll, G. *J. Chem. Soc.-Perkin Trans. 2*, **2002**, *12*, 2039-2043.

[163] Shida, T. In *Electronic Absorption Spectra of Radical Ions*; Elsevier: Amsterdam, **1988**.

[164] Barthel, E. R.; Martini, I. B.; Schwartz, B. J. *J. Chem. Phys.*, **2000**, *112*, *21*, 9433-9444.

[165] Long, F. H.; Lu, H.; Eisenthal, K. B. *Chem. Phys. Lett.*, **1990**, *169*, 165.

[166] Gauduel, Y.; Galabert, H.; Ashokkumar, M. *Chem. Phys.*, **1995**, *197*, 167.

[167] Iglev, H.; Laenen, R.; Laubereau, A. *Chem. Phys. Lett.*, **2004**, *389*, *4-6*, 427-432.

[168] Blandamer, M. J.; Fox, M. F. *Chem. Rev.*, **1970**, *70*, 59.

[169] Markovich, G.; Pollak, S.; Giniger, R.; Cheshnovsky, O. *J. Chem. Phys.*, **1994**, *101*, 9344.

[170] Baik, J.; Kim, J.; Majumdar, D.; Kim, K. S. *J. Chem. Phys.*, **1999**, *110*, 9116.

[171] Gauduel, Y.; Pommeret, S.; Antonetti, A. *J. Phys. Condens. Matter*, **1990**, *2*, 171.

[172] Assel, M.; Laenen, R.; Laubereau, A. *Chem. Phys. Lett.*, **1998**, *289*, 267.

[173] Lu, H.; Long, F. H.; Eisenthal, K. B. *J. Opt. Soc. Am. B*, **1990**, *7*, 1511.

[174] Long, F. H.; Shi, X.; Lu, H.; Eisenthal, K. B. *J. Phys. Chem.*, **1994**, *98*, 7252.

[175] Sheu, W. S.; Rossky, P. J. *Chem. Phys. Lett.*, **1993**, *202*, 186.

[176] Sheu, W. S.; Rossky, P. J. *J. Phys. Chem.*, **1996**, *100*, 1295.

[177] Borgis, D.; Staib, A. *J. Phys. Condens. Matter*, **1996**, *8*, 9389.

[178] Staib, A.; Borgis, D. *J. Chem. Phys.*, **1996**, *104*, 9027.

[179] Kloepfer, J. A.; Vilchiz, V. H.; Lenchenkov, V. A.; Bradforth, S. E. *Chem. Phys. Lett.*, **1998**, *298*, *1-3*, 120-128.

[180] Kloepfer, J. A.; Vilchiz, V. H.; Lenchenkov, V. A.; Germaine, A. C.; Bradforth, S. E. *J. Chem. Phys.*, **2000**, *113*, *15*, 6288-6307.

[181] Kloepfer, J. A.; Vilchiz, V. H.; Lenchenkov, V. A.; Chen, X. Y.; Bradforth, S. E. *J. Chem. Phys.*, **2002**, *117*, *2*, 766-778.

[182] Krissinel, E. B.; Agmon, N. *J. Comput. Chem.*, **1996**, *17*, 1085.

[183] Jou, F. Y.; Freeman, G. R. *J. Phys. Chem.*, **1979**, *83*, 2383.

[184] Crowell, R. A.; Lian, R.; Shkrob, I. A.; Bartels, D. M.; Chen, X. Y.; Bradforth, S. E. *J. Chem. Phys.*, **2004**, *120*, *24*, 11712-11725.

[185] Madsen, D.; Thomsen, C. L.; Thogersen, J.; Keiding, S. R. *J. Chem. Phys.*, **2000**, *113*, 1126.

[186] Debye, P.; Edwards, J. O. *J. Chem. Phys.*, **1952**, *20*, 236.

[187] Pines, E.; Huppert, D.; Agmon, N. *J. Chem. Phys.*, **1988**, *88*, 5620.

[188] Bressler, C.; Saes, M.; Chergui, M.; Grolimund, D.; Abela, R.; Pattison, P. *J. Chem. Phys.*, **2002**, *116*, 2955.

[189] Kevan, L. *Ace. Chem. Res.*, **1981**, *14*, 138.

[190] Koneshan, S.; Rasaiah, J. C.; Lynden-Bell, R. M.; Lee, S. H. *J. Phys. Chem. B*, **1998**, *102*, 4193.

[191] Schmidt, K. H.; Han, P.; Bartels, D. M. *J. Phys. Chem.*, **1995**, *99*, 10530.

[192] Press, W. H.; Flannery, B. P.; Teukolsky, S. A.; Vetterling, W. T. *Numerical Recipes, Cambridge University Press*, **1986**.

[193] DeBiase, R.; Elliot, J. D.; Hartnett, T. E. *Petroleum-Derived Carbons, ACS Symposium Series*, **1986**, *303*, 155.

[194] Bressler, C.; Saes, M.; Chergui, M.; Grolimund, D.; Abela, R.; Pattison, P. *J. Chem. Phys.*, **2002**, *116*, *7*, 2955-2966.

[195] Fleming, G. R. *Chemical Applications of Ultrafast Spectroscopy*, Oxford University Press: New York **1986**.

[196] Castleman, A. W. J.; Sundstrom, V. eds. *special issue on Ten Years of Femtochemistry, J. Phys. Chem. A 102, 4021 (1998)***1998**.

[197] Zewail, A. H. *J. Phys. Chem. A*, **2000**, *104*, 5660-5694.

[198] Schotte, F.; Lim, M. H.; Jackson, T. A.; Smirnov, A. V.; Soman, J.; Olson, J. S.; Phillips, G. N.; Wulff, M.; Anfinrud, P. A. *Science*, **2003**, *300*, *5627*, 1944-1947.

[199] Ihee, H.; Lobastov, V. A.; Gomez, U. M.; Goodson, B. M.; Srinivasan, R.; Ruan, C. Y.; Zewail, A. H. *Science*, **2001**, *291*, *5503*, 458-462.

[200] Lewis, J. W.; Goldbeck, R. A.; Kliger, D. S.; Xie, X.; Dunn, R. C.; Simon, J. D. *J. Phys. Chem.*, **1992**, *96*, 5243-5254.

[201] Goldbeck, R. A.; Kim-Shapiro, D. B.; Kliger, D. S. *Annu. Rev. Phys. Chem.*, **1997**, *48*, 453-479.

[202] Berova, N.; Nakanishi, K.; Woody, R. W. eds. *Circular Dichroism - Principles and Applications*, Wiley-VCH: New York\ **2000**.

[203] Harada, N.; Nakanishi, K. *Circular Dichroic Spectroscopy - Exciton Coupling in Organic Stereochemistry*, University Science Books **1983**.

[204] Lightner, D. A.; Gurst, J. E. In *Organic Conformational Analysis and Stereochemistry from Circular Dichroism Spectroscopy*; Wiley-VCH: New York, **2000**, pp. 423-456.

[205] Bjorling, S. C.; Goldbeck, R. A.; Milder, S. J.; Randall, C. E.; Lewis, J. W.; Kliger, D. S. *J. Phys. Chem.*, **1991**, *95*, *12*, 4685-4694.

[206] Beychok, J. L. S. *Science*, **1978**, *199*, *4327*, 425-426.

[207] Michael Anson, S. R. M., and Peter M. Bayley. *Rev. Sci. Instrum.*, **1977**, *48*, *8*, 953-962.

[208] Ferrone, F. A.; Hopfield, J. J.; Schnatterly, S. E. *Rev. Sci. Instrum.*, **1974**, *45*, *11*, 1315-1481.

[209] Xie, X. L.; Simon, J. D. *Rev. Sci. Instrum.*, **1989**, *60*, *8*, 2614-2627.

[210] Alfano, R. R. *Springer, New York*, **1989**.

[211] Midorikawa, K.; Kawano, H.; Suda, A.; Nagura, C.; Obara, M. *Appl. Phys. Lett.*, **2002**, *80*, *6*, 923-925.

[212] Brodeur, A.; Chin, S. L. *Phys. Rev. Lett.*, **1998**, *80*, *20*, 4406-4409.

Acknowledgements

I would like to warmly thank to all who have contributed to the successful completion of this work and to the accompanying projects during its time.

I give my special thanks to:

Prof. Dr. Torsten Fiebig for the opportunity to do such a great research in his group, for his creativity in solving any problem, for his endless enthusiasm through all these years and for his outstanding openness to interesting new ideas.

Prof. Ivan Buchvarov for his self sacrificing support and thrust, for his enormous creativity and excitement in doing optical science, for his understanding, ever helpful advice and stimulating discussions.

Prof. Dr Wolfgang Domcke for his everlasting availability for any kind of help and support.

Prof. Dr. Maria-Elisabeth Michel-Beyerle for her impressible support and for giving me the opportunity to work in her labs.

Prof. Dr. Hans-Achim Wagenknecht for his preparation of the samples of chromophore-labeled DNA duplexes and for the very successful collaboration.

Dr. Hristo Iglev for his enthusiasm in our joint work and his everlasting ability to generate brilliant ideas.

Dr. Gagik Gurzadyan and Dr. Till fon Feilitzch for their friendly support in the field of science.

Sotir Chervenkov, Dr. Ivan Kondov, Rossen Karaminkov, Stoian Georgiev and Milen Raytchev for giving me generous assistance in solving a huge amount of everyday problems.

Appendix A - List of abbreviations

t	life time
l	wavelength
°C	degree Celsius
A	acceptor
A	adenine/adenosine
Å	Ångström
BBO	beta barium borate
Br-dU	5-bromo-2'-deoxyuridine
C	cytosine/cytidine
CCD	charge-coupled device
CD	circular dichroism
CIP	contact ion pair
cm	centimeter(s)
CT	charge transfer
CTTS	charge transfer to solvent
D	donor
dC	deoxycytidine
dG	deoxyguanosine
DMF	dimethylformamide
DMSO	dimethylsulfoxide
DNA	deoxyribonucleic acid
DPSSL	diode pumped solid state laser
dU	deoxyuridine
e.g.	for example (exempli gratia)
EP	Py-=-dU modified DNA duplex
ET	electron transfer
fs	femtosecond(s)
FWHM	full width at half maximum
g	gram(s)
G	guanine/guanosine
h	hour(s)

HOMO	highest occupied molecular orbital
HT	hole transfer
i. e.	that is (id est)
IC	internal conversion
IC	inter-chromophore
IRF	instrumental response function
l	liter(s)
KTP	potassium titanyl phosphate
LBO	lithium triborate
LCT	local charge transfer
LUMO	lowest unoccupied molecular orbital
MD	molecular dynamics
MeOH	methanol
MeCN	acetonitrile
ml	milliliter(s)
mM	millimolar
mm	millimeter(s)
mOD	milli-optical density
ms	millisecond(s)
MTBE	tert-butyl-ethyl-ether
Nd:YVO_4	neodimium-doped yttrium vanadate
NLM	non-linear mirror
nm	nanometer(s)
NHE	normal hydrogen electrode
NOPA	noncolinear optical parametric amplifier
OD or O.D.	optical density
PCET	proton-coupled electron transfer
PCI	peripheral component interconnect
pK_a	acid ionization constant
ps	picosecond(s)
PT	proton transfer
PU	PydU-modified DNA duplex
Py	pyrene
Py-=-dU	5-(1-pyrenylethynyl)-2’-deoxyuridine

Py-≡-H	1-ethynyl-pyrene
PydU	5-(pyren-1-yl)-2’-deoxyuridine
r	distance
RCT	reversed charge transfer
R.T.	room temperature
S0	ground state
S1	lowest excited singlet state
S2	excited singlet state
sec	second(s)
SESAM	semiconductor saturable absorber mirror
SHG	second harmonic generation
T	thymin/thymidin
TCSPC	time correlated single photon counting
TEC	thermo electrical cooling
TRA	triarylamine
UV	ultra violet
W	Watt
WLC	white light continuum
WLG	white light generator
XPM	cross-phase modulation

Appendix B - Contribution to journals

1. **Photoionization Dynamics of an Aqueous Iodide Solution: the Temperature Dependence**

   H. Iglev, A. Trifonov, A. Thaller, I. Buchvarov, T. Fiebig, A. Laubereau
   Chemical Physics Letters 2005, 403, 198 – 204

2. **Real-Time Spectroscopic and Chemical Probing of Reductive Electron Transfer in DNA.**

   P. Kaden, E. Mayer-Enthart, A. Trifonov, T. Fiebig, H.-A. Wagenknecht
   Angewandte Chemie International Edition 2005, 44, 1636 – 1639

3. **Real-Time Observation of Hydrogen Bond-Assisted Electron Transfer to a DNA Base**

   A. Trifonov, I. Buchvarov, H.-A. Wagenknecht, T. Fiebig
   Chemical Physics Letters 2005, 409, 277 – 280

4. **Photoinduced Charge Transfer Processes along Triarylamine Redox Cascades**

   C. Lambert, J. Schelter, T. Fiebig, D. Mank, A. Trifonov
   Journal of American Chemical Society 2005, 127, 10600 – 10610

5. **Ultrafast Energy Transfer and Structural Dynamics in DNA**

   A. Trifonov, M. Raytchev, I. Buchvarov, M. Rist, J. Barbaric, H-A. Wagenknecht, T. Fiebig
   Journal of Physical Chemistry B accepted for publication

Available online at www.sciencedirect.com
SCIENCE DIRECT®
Chemical Physics Letters 403 (2005) 198–204
CHEMICAL PHYSICS LETTERS
www.elsevier.com/locate/cplett

Photoionization dynamics of an aqueous iodide solution: the temperature dependence

H. Iglev [a,*], A. Trifonov [b], A. Thaller [a], I. Buchvarov [c], T. Fiebig [b], A. Laubereau [a]

[a] Physik-Department E11, Technische Universität München, James-Frank-Strasse, 85748 Garching, Germany
[b] Eugene F. Merkert Chemistry Center, Boston College, Chestnut Hill, 02467 MA, USA
[c] Department of Quantum Electronics, Faculty of Physics, University of Sofia, 5 J. Bouchier Blvd. 1164 Sofia, Bulgaria

Received 1 December 2004; in final form 21 December 2004
Available online 18 January 2005

Abstract

We report on the electron photodetachment dynamics after excitation at 242 nm of the lowest charge transfer state of aqueous I^- at solution temperatures of 25, 50 and 75 °C. A first intermediate is observed that builds up with a time constant of 220–180 fs in the investigated temperature interval and is assigned to an iodine:electron pair in a transient solvent configuration. Subsequent solvent reorganization leads to a quasi-equilibrated hydrated atom:electron pair $(I{:}e^-)_{hyd}$ that builds up with a time constant of 700–540 fs at 25–75 °C. The following relaxation seems to be governed by partially diffusion-controlled recombination of the electron in the presence of an attraction potential well with depth of about 850 cm^{-1}.

1. Introduction

In the past decade particular interest was devoted to ultrafast charge transfer in ionic solutions [1–4]. A prominent type of electron transfer is that shown by halide anions revealing the strong influence of solvent–solute interaction. Ionization of isolated halides in the gas phase does not involve bound electronic states below the detachment threshold [5]. For a halide anion embedded in a water cluster, the ionization energy increases with the cluster size, due to the solvent-induced stabilization of the anion [6,7]. The correspondingly high ionization threshold in bulk solution allows for the appearance of a neighboring band of levels called charge-transfer-to-solvent states (CTTS) [5], since photoexcitation in this band produces a neutral halogen atom and a solvated electron.

The sub-picosecond electron detachment of aqueous chloride solutions after two-photon excitation was examined by Gauduel et al. [3,8] and other groups [9,10]. Eisenthal and co-workers carried out a time-resolved study of solvated electrons formed after two and three-photon excitation of aqueous iodide solutions [2,11]. The experiments stimulated detailed theoretical studies of Sheu and Rossky [12,13]. The molecular-dynamics (MD) simulations predict two formation channels of the solvated electron after population of a high-lying CTTS-state of the iodide: Direct nonadiabatic electron separation (within 50 fs) or fast relaxation within the CTTS states to the lowest charge transfer state (time constant of 450 fs) and subsequent adiabatic separation of the electron from the iodine. A complex was predicted consisting of an atom, between an electron and a water molecule. The structure obviously displays spectral features similar to that of a hydrated electron since the first solvation shell of the charge is solely occupied by water molecules. Geminate recombination of the complex was predicted to occur within a few

* Corresponding author. Fax: +49 89 289 12842.
E-mail address: higlev@ph.tum.de (H. Iglev).

0009-2614/$ - see front matter © 2005 Elsevier B.V. All rights reserved.
doi:10.1016/j.cplett.2005.01.014

picoseconds, whereas the release of the electron appeared to be unlikely in the computations. The result is not consistent with the large yield of the generated solvated electrons found experimentally [2,11].

More recent computations of Staib and Borgis [14,15] for an aqueous chloride solution arrived at somewhat different conclusions due to the more detailed treatment of the solvent polarization. The results of these authors may be summarized as follows: The initial excitation of the anion in the lowest charge transfer state was considered that leads to an excited state absorption centered at 1.13 μm [15]. Within the first 100 fs the electron separates ≈4 Å from the parent chlorine core. In the following first picosecond the system develops a larger chlorine–electron separation of ≈6 Å that is accompanied by a continuous shift of the induced absorption from 950 to 720 nm. The calculated free enthalpy $G(r)$ of the system exhibits a distinct minimum around $r_{min} = 6$ Å which lies $\Delta G = 3 \pm 0.5 k_B T$ below the value for complete detachment. The pair dissociation competes with a nonadiabatic recombination of the electron and chlorine atom. Based on the results of the MD quantum simulations Staib and Borgis proposed a simple kinetic model for the relaxation dynamics after photoexcitation of aqueous chloride. The CTTS excited Cl^-_{aq} is converted into the hydrated (Cl:e^-) pair with a rate $k_{gen} = 2.5\ ps^{-1}$. The latter can dissociate ($k_{dis} = 0.031\ ps^{-1}$) while the nonadiabatic recombination to a ground state anion Cl^- is slow ($k_{rec} = 0.001\ ps^{-1}$) [15].

Bradforth and co-workers recently presented experimental data on aqueous iodide [16–18] at room temperature after one-photon excitation into the lowest CTTS band. Using the discussed kinetic model a formation time of the hydrated iodine:electron pair of $k_{gen}^{-1} = 200$ fs was reported [16]. The complex subsequently recombines with a time constant of $k_{rec}^{-1} = 33$ ps or dissociates with a time constant of $k_{dis}^{-1} = 70$ ps. The latter value obviously represents an upper limit and not the relaxation time directly, since geminate recombination of dissociated electrons, i.e., hydrated electrons, was omitted in the analysis. Correspondingly it was shown that the simple model cannot describe the recombination dynamics for times larger than 100 ps when slow contributions to diffusive recombination appear [17,18].

Therefore, the long-tail dynamics is analyzed with the help of a diffusion recombination in the absence of an interaction potential. The extracted parameter values, however, of 26 and 24 Å, obtained, respectively, for the initial and recombination distance between the iodine and the electron are not meaningful. Kloepfer et al. [18] also obtained a numerical solution of the partially diffusion-controlled geminate recombination of a pair in the presence of an interaction potential using a code provided by Krissinel and Agmon [19]. The extracted well depth and position of the minimum of the free enthalpy were $\Delta G = 620\ cm^{-1}$ and $R_0 = 4$ Å, respectively [18].

The experimental studies support the microscopic picture for the electron detachment of aqueous halides developed from MD simulations. One important aspect of the relaxation dynamics of the atom:electron pair however is still missing: experimental information about the lifetime of the hydrated iodine:electron pairs. In this paper the temperature dependence of the photoionization dynamics is investigated that provides some evidence of the pair dissociation rate. To this end, a series of pump–probe experiments on aqueous I^- is carried out at three temperatures, 25, 50 and 75 °C. The relaxation dynamics after single-photon excitation into the first CTTS band is studied with broad-band femtosecond probe pulses in the spectral range 400–1100 nm. The temperature-dependent observations provide novel information on the relaxation dynamics of the atom:electron pair and give experimental support to the MD prediction of an attractive interaction between the separated electron and the parent atom.

2. Experimental

The femtosecond spectrometer used to study the electron photodetachment is based on a commercial Ti:sapphire amplifier system generating 150-fs pulses of 800 μJ and 1 kHz repetition rate at 775 nm. A portion of the pulse is used to pump a first two-stage noncollinear optical parametric amplifier (VIS NOPA, see Fig. 1). Tunable pulses between 450 and 700 nm with energies of 7–20 μJ are obtained after passing a two-prism compressor. For the UV excitation process the output of the NOPA tuned to 484 nm is frequency-doubled in a

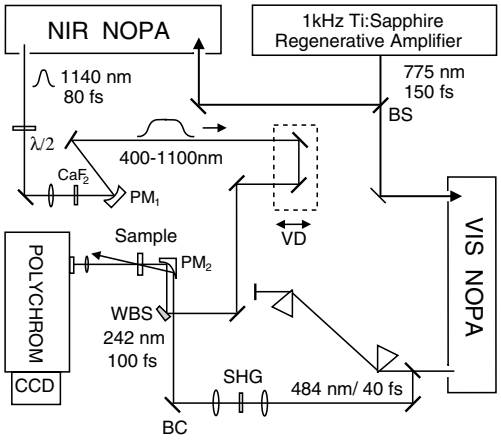

Fig. 1. Schematic diagram of the experimental setup. The following abbreviations are used: BS, beam splitter; a λ/2 plate; CaF_2, calcium fluoride plate; $PM_{1,2}$, 30° and 90° off-axis parabolic mirrors; VD, variable delay line; BC, beam coupler; WBS, wedged beam splitter.

100-μm BBO-crystal providing pulses at 242 nm with energies of 1 μJ and a duration of 100 fs.

For probing purposes a second NOPA (NIR NOPA, see Fig. 1) generates 80-fs pulses at 1140 nm that produce a white light continuum (WLC) by focusing into a 3-mm thick rotating CaF_2 plate. The applicable wavelength range of the WLC extends from 400 to 1100 nm. Using a wedged beam splitter the continuum is split into two parts for probing and reference measurements. The reference radiation is directed through a sample volume that is not affected by the pump pulse. The relative polarizations of the pump and the probe beams are set to the magic angle 54.7° for rotation-free observation. The probe and reference spectra are detected independently and simultaneously behind the sample, using an imaging polychromator and a CCD array cooled to −20 °C.

Due to the monotonous frequency chirp of the WLC emission [20], the radiation can be represented as a superposition of delayed femtosecond pulses close to the Fourier transform limit, centered at a series of frequencies. The relationship between the frequency position and time delay of the constituents is described by a chirp function. The time evolution of the pulses at various wavelengths was determined by cross-correlation measurements in a 100 μm BBO crystal with a test-pulse of 35 fs at 675 nm from the VIS NOPA. The measured pulse durations of the spectral components varied between 90 and 110 fs.

The sample cell, equipped with 1-mm windows of UV grade fused silica, has a thickness of 250 μm and is filled with a circulating solution of NaI (Merck Eurolab, GR for analysis) in de-ionized water at a concentration of about 2.5 mM. In order to maintain a constant sample temperature, the solution passes a temperature controller right before the sample cell. The experiments are performed at three different temperatures, 25, 50 and 75 °C, respectively. Because of a sufficiently large quantity of the investigated liquid volume (900 ml) the concentration of undesired photo-products like I_2^- can be neglected.

At all wavelengths a coherent artifact is observed around zero delay time, possibly due to cross-phase modulation (XPM) between the intensive pump and weak probe pulses [21]. The phenomenon manifests itself by rapid, small changes of the probe transmission at zero delay time. In order to enlarge the XPM signal the 242 nm excitation pulse was replaced by 15 μJ 484-nm pulse, by substitution of the 100 μm BBO crystal by fused silica specimen with the same optical path. Since the different spectral components of the probing continuum traverse the sample at different delay times, the coherent artifact provides a convenient way for in situ determinations of the zero delay time setting at the respective probing wavelengths with an accuracy of ±20 fs.

3. Spectroscopic data

Examples for the measured transient absorption spectra at 25 °C after single-photon excitation at 242 nm are presented in Fig. 2. The data extend over the range 425–1100 nm. Only selected delay time values are presented. Around 484 nm a gap of the probe data occurs that is due to the deflection of pump radiation into the probe beam direction. While no transmission effect is found at −200 fs, a small absorption change is already seen at delay time zero that increases from 650 to 1000 nm (see Fig. 2a). The maximum of this early absorption appears at 1000 nm (t_D = 0 ps), but cannot be accurately determined with the available probing range. The spectral feature grows within the first 200 fs and develops to a broad band centered at ≈900 nm. Increasing the delay time the maximum of this absorption shifts to shorter wavelengths and only 400 fs later (t_D = 0.6 ps, see Fig. 2a) it is located at ≈760 nm. At later delay times the absorption narrows notably and reaches a stable maximum position at ≈720 nm. A spectrum close to that of the equilibrated solvated electron [22] is reached at t_D = 1.4 ps. An isosbestic point is not indicated by the transient spectra of Fig. 2a. It is concluded that more than one intermediate is involved in the dynamics.

The measurements for larger delay times up to 1 ns (see Fig. 2b) indicate that the changes in the absorption band shape have terminated ≈3 ps after the photode-

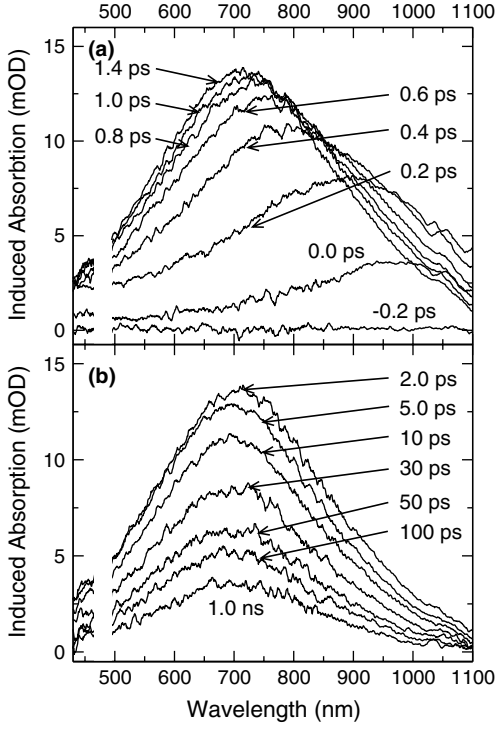

Fig. 2. Temporal evolution of the absorption changes of an aqueous NaI solution at 25 °C after excitation at 242 nm; different delay time values indicated in the inset.

tachment process. The agreement with the absorption of the fully solvated electron provides strong evidence that at least the first solvation shell of the separated electron is already fully established at this time. The subsequent relaxation (see Fig. 2b) can be assigned to population decay, i.e., geminate recombination of the photogenerated electron with the parent atom.

For the same experimental conditions, but at higher temperatures of 50 and 75 °C corresponding measurements were carried out obtaining a similar time evolution of the spectra (data not shown). At longer delay times ($t_D \geqslant 1.5$ ps) the transient absorption was found to be slightly broadened and red-shifted as compared to the data of Fig. 2b. The observed band maxima are located at 750 and 775 nm for 50 and 75 °C, respectively. This spectral shift is in close agreement with the well-known temperature dependence of the absorption spectrum of the equilibrated solvated electron [22].

Some results for the signal transients deduced from the transient spectra are depicted in Fig. 3. Three selected wavelengths of 575, 725 and 1075 nm are considered (experimental points, calculated solid lines). The maximal absorbance change measured at the respective probing wavelength for the higher temperatures are normalized to the value at 25 °C for a direct comparison. Different delay time intervals are depicted in the left and right hand parts of the figure. The temperature dependence is noteworthy. Especially at 575 nm the induced absorption at 25 °C (see full circles in Fig. 3a) increases more slowly as compared to higher temperatures. The signal curves reach a maximum at $t_D \sim 1$–1.5 ps. In the near infrared the observed dynamics is obviously faster. The signal transients at 1075 nm (Fig. 3e) reach a distinct maximum already at ≈0.2 ps, shortly after the peak of the UV pulse. The subsequent decay occurs with an effective time constant of ~0.5–0.7 ps.

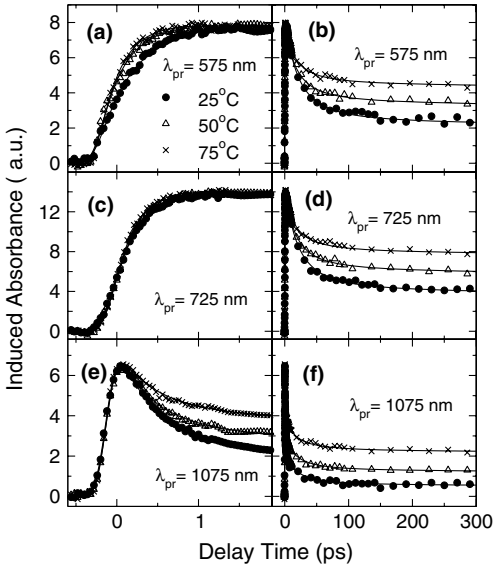

Fig. 3. Transient absorption changes of aqueous iodide after excitation at 242 nm measured at 575, 725 and 1075 nm for the solution temperature of 25 °C (full points), 50 °C (open triangles) and 75 °C (crosses); experimental points, calculated solid lines.

The measurements for larger delay up to 300 ps (see r.h.s. of Fig. 3) indicate that after the maxima around $t_D \sim 1.5$ ps the absorption curves decrease to different plateau values, dependent on temperature but within time intervals independent of the probing wavelengths (note different ordinate scales). The relaxation profile cannot be fitted by a simple exponential decay. The finding supports the assumption that the long-time dynamics are dominated by diffusion-controlled geminate recombination [18]. Inspection of Fig. 3 reveals that the fraction of electrons undergoing geminate recombination in the aqueous iodide solution obviously decreases as the temperature rises. A similar dependence was recently reported for the photoionization of aqueous hydroxide [23] and neat water [24]. But the exact values for the survival probability of the hydrated electrons reported for the latter solutions are different from that of aqueous iodide (see below).

We finally mention that measurements of a neat water sample under the same excitation conditions show no measurable effect within experimental accuracy (data not shown). Therefore, a contribution of photoionization of the solvent to the signal transients presented here is negligible.

4. Data analysis

According to the arguments in Section 1 the initially excited lowest charge transfer (LCT) state decays with a time constant τ_1. The followed electron separation is accounted for by a discrete precursor state $(I{:}e^-)_{non\text{-}eq}$. Subsequently, a quasi-equilibrated hydrated halogen:electron pair $(I{:}e^-)_{hyd}$ is formed, representing a further intermediate in our model. The formation and solvent relaxation of the pair takes a time constant τ_2 that is introduced in our model as the decay time of the precursor $(I{:}e^-)_{non\text{-}eq}$. The relaxation of the weakly bound atom:electron pair $(I{:}e^-)_{hyd}$ may be described by three-dimensional diffusion of the particles in the presence of a radially symmetric potential $U(r) = \Delta G\{1 - \exp(-\beta(r - R_0))\}^2$. Here ΔG is the depth of the potential well. r and R_0, respectively, denote the particle separation and minimum position. The scaling factor β accounts for the potential width. The relaxation of the pair in this potential is governed by the spherically symmetric Debye–Smoluchowski equation [25]. An elegant method for a numerical solution of this equation is based on the detailed-balance approximation [26]. The numerical algorithm begins with a discretization of the radial coordinate r, from contact radius r_c ($i = 0$) between atom

and electron to some maximum value, r_{max} ($i = m$). The resulting radial layers are accounted for by separate states with populations equal to the average population density of the layers. In this approximation a population exchange exists just between direct neighbor layers, while the exchange rates depend on the interaction potential. The transition rate Ω from a state $|j\rangle$ to a neighboring state $|i\rangle$ ($i = j \pm 1$) is given by: $\Omega(i|j) = (D/\Delta r^2)(r_i/r_j)\exp\{-(V(r_i) - V(r_j))/2\}$ [26]. Here $D = D_{I^0} + D_{e^-_{aq}}$ is a mutual diffusion coefficient, and $V(r) = U(r)/k_BT$ is the normalized potential depending on temperature. The equilibrated iodine:electron pair is generated at distance $r = R_0$ with rate $1/\tau_2$, while the backward reaction leading to the groundstate anion occurs simultaneously at the contact distance $r = r_c$ (absorbing boundary condition). r_{max}, on the other hand, is taken large enough (>15 Å), so that the gradient of the potential curve is negligible. At these distances the electron is expected to be fully solvated and quasi-stable so that the recombination rate vanishes. The terminating level is the equilibrated, hydrated electron e^-_{aq}.

Consistent with the MD results and the data of Fig. 2b, it was assumed that the spectral properties of the hydrated pair in the probing range are constant during the dissociation process and agree with the absorption of the solvated electron. This spectral similarity supports the assumption that the $(I{:}e^-)_{hyd}$ is assembled from a solvation configuration with an iodine an electron and a water molecule in between. The microscopic picture provides the possibility to estimate the I–e^- distance to be $R_0 = 6.1$ Å as the sum of the iodine–oxygen distance ($R_{I-O} = 3$ Å) [27] and the radius of the first solvation shell of the electron (R_{O-e^-}=3.1 Å) [28] distances in aqueous solution. The mutual diffusion coefficient at room temperature was estimated to be $D = 0.56$ Å^2/ps from the reported numbers $D_{I^0} = 0.1$ Å^2/ps [29] and $D_{e^-_{aq}} = 0.46$ Å^2/ps [30] for the components. The values of D at 50 and 75 °C were treated as fitting parameters. The free parameters of the model (relaxation rates, potential constants, extinction coefficients, etc.) are obtained by fitting the calculated curves (note solid lines in Fig. 3) to the measured signal transients using Powell's method [31].

5. Results and discussion

The results of the data analysis are summarized in Table 1 and in Fig. 4. After population of the LCT state of the iodide by a 5.1 eV photon, a broad absorption shows up in the near-infrared with a maximum close to 1000 nm at all three solution temperatures. The excited state absorption of LCT (filled squares and dotted lines on Fig. 4) may be assigned to transitions to higher-lying CTTS levels. The relaxation of LCT assigned to the escape of the electron from the parent solvent cavity is found to occur with time constants $\tau_1 = 220$–180 fs, going from 25 to 75 °C (see Table 1).

An important property of the solvated electron is the high sensitivity of its absorption spectrum to the local environment [32]. Thus the rapid development of the transient absorption spectra observed within the first 1 ps (see Fig. 2a) supports the conclusion that the initial relaxation dynamics is accompanied by a continuous reorganization of the electron solvation cavity. The argument is in accordance with the MD prediction for the separation of the electron from the parent halogen [15]. Because of different time scales involved in the electron detachment and as is discussed above, the process is divided in our model into two steps. A first intermediate of the pair is formed that is assigned to an atom:electron pair in a yet non-equilibrated solvent configuration $(I{:}e^-)_{non\text{-}eq}$. The experimental data support this picture. The intermediate is characterized by a broad absorption band centered at 825 nm (hollow triangles and dashed lines in Fig. 4). The spectral profile of the intermediate and its built-up rate $1/\tau_1$ are only weakly temperature dependent in the investigated range. The finding suggests that increasing the solution temperature the relaxation pathway remains unchanged.

Table 1
Relaxation times and fitting parameters: R_0 and D' at 25 °C are input parameters taken from the literature

	25 °C	50 °C	75 °C	Refs. [16,18]	Cl^-_{aq}, Ref. [15]
τ_1 (fs)	220 ± 50	200 ± 50	180 ± 50	200	100
τ_2 (fs)	700 ± 50	650 ± 50	540 ± 50	–	400
D' (Å^2/ps)	0.58	0.95 ± 0.1	1.35 ± 0.1	0.8	0.78
r_c (Å)	5.0 ± 0.1	(5.0 ± 0.1)	(5.0 ± 0.1)	4.0	–
R_0 (Å)	6.1	(6.1)	(6.1)	4.0	6.0
β (Å^{-1})	0.68 ± 0.05	0.80 ± 0.05	0.93 ± 0.05	1.1	–
ΔW (Å)	2.6 ± 0.2	2.2 ± 0.2	2.0 ± 0.2	–	3
ΔG (cm^{-1})	850 ± 100	830 ± 100	860 ± 100	620	620 ± 100
η	0.25 ± 0.02	0.39 ± 0.02	0.53 ± 0.02	0.25	0.75
τ_{pair} (ps)	21 ± 2	17.5 ± 3	16 ± 2	22	32

The values in brackets are input parameter taken from 25 °C measurement. For comparison the room temperature data of Kloepfer et al. [16,18] and results from MD simulations for aqueous Cl^- [15] are also displayed.

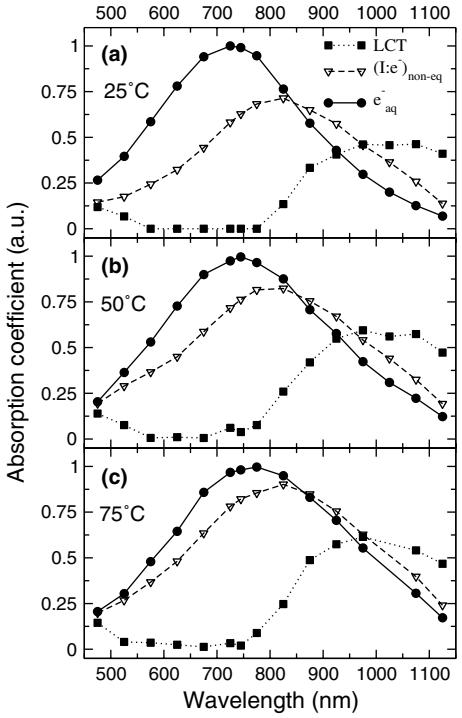

Fig. 4. Molar absorption coefficients of the observed intermediates assigned to the initially excited LCT state (filled squares), the transient $(I:e^-)_{non\text{-}eq}$ state (hollow triangles), together with that of the final product: equilibrated solvated electron (filled circles). The points are obtained by fitting the theoretical model to the experimental data shown in Figs. 2 and 3.

The further separation of the excess electron from the iodine atom and organization of the new solvation layer leads to the hydrated atom:electron pair $(I:e^-)_{hyd}$. This complex shows an absorption spectrum similar to that of e^-_{aq} (see Fig. 2). For the formation of the $(I:e^-)_{hyd}$ the time constant τ_2 is found to vary from 700 to 540 fs for temperatures from 25 to 75 °C. The rise of the formation rate may be attributed to the higher mobility of the water molecules at increased solvent temperature.

The hydrated complex $(I:e^-)_{hyd}$ is stabilized by an attractive interaction described by a Morse potential. The extracted well depth $\Delta G = 850 \pm 100\ cm^{-1}$ remain unaffected by temperature variation (see Table 1). The contact distance r_c at which the recombination between the excess electron and the parent occurs, is fitted to 5.0 ± 0.1 Å. The numbers for R_0, and r_c at 25 °C are assumed to depend only weakly on temperature and used as input parameters in the analysis of the dynamics at the higher temperatures. For the Morse constant the numbers seem to increase from $\beta = 0.68 \pm 0.05$ to $0.93 \pm 0.05\ Å^{-1}$ going from 25 to 75 °C. The corresponding full halfwidth ΔW of the potential curve decreases from 2.6 ± 0.2 Å at 25 °C to 2.0 ± 0.2 Å at 75 °C. Adopting the above developed microscopic picture the faster decrease of the iodine–electron attraction may be related to the higher librational energy of the water molecules in the solvation layer of the atom:electron pair with rising temperature. Describing the measured long-time dynamics (see r.h.s. of Fig. 3) with a simple exponential fit we can determinate the effective lifetime τ_{pair} of $(I:e^-)_{hyd}$. The experimental data show that this time constant decreases from $\tau_{pair} = 21 \pm 2$ ps to 16 ± 2 ps going from 25 to 75 °C.

The results for the mutual diffusion coefficient D' are 0.95 ± 0.1 and $1.35 \pm 0.1\ Å^2$/ps at 50 and 75 °C, respectively. The values are consistent with the well-known temperature dependence of $D_{e^-_{aq}}$ [30]. The strong temperature dependence of the diffusion coefficient reflects the corresponding variation of the quantum yield η for generating fully solvated electrons. Our data show (see Table 1) that 1 ns after the optical excitation the ratio of fully solvated electrons to the atom:electron pairs at $t_D = 1.5$ ps increases from $\eta = 0.25 \pm 0.02$ to 0.53 ± 0.02 in the range 25–75 °C. These numbers are smaller than the measured for aqueous F^- at room temperature, where $\eta = 0.77 \pm 0.03$ [4]. Taking into account the similar diffusion coefficient, $D_F = 0.33 Å^2$/ps, [29] this variation shows the strong influence of the halogen atom on the ps relaxation dynamics, i.e., gives some experimental support to the existence of atom:electron pair.

For comparison the room temperature results of Kloepfer et al. are listed in the 5th column of Table 1 [16,18]. Our numbers for the decay time τ_1 of the LCT agree well with their result. The build-up time τ_2 of the quasi-equilibrated atom:electron species was not reported by these authors. Our value for ΔG is somewhat greater than reported by Kloepfer et al. It is felt that the investigated temperature dependence of the present work provides sensitive information on the attractive interaction of the pair. A significant difference in the analysis of Kloepfer et al. [18] is the amazingly small value of the I–e^--distance of $R_0 = 4$ Å, as compared to the iodine–oxygen distance (3 Å) [27] and the radius of the first solvation shell of the electron (3.1 Å) [28].

6. Summary

We report on the photodetachment of electrons in a 2.5 mM iodide solution at temperature values of 25, 50 and 75 °C. After one-photon excitation by a 100 fs-pulse at 242 nm into the lowest CTTS band, the dynamics are studied with 100 fs probe radiation in the spectral range of 400–1100 nm. The initially excited LCT state shows a broad absorption in the NIR with a maximum around 1000 nm at all three bulk temperatures. As concluded from the measured LCT relaxation the released electron escapes the anion solvation shell with a time constant $t_1 = 220$–180 fs going from 25 to 75 °C. The separation of the excess electron from the iodine atom and the assembling of a new solvation configuration takes 700–540 fs in the mentioned temperature interval. To account for the two time scales two intermediates are

introduced that are assigned to an atom:electron pair in a non-equilibrated solvation structure and a quasi-equilibrated, hydrated pair. The former precursor, $(I{:}e^-)_{non\text{-}eq}$ is characterized by an absorption spectrum centered at 825 nm that is only weakly affected by the temperature variation in the investigated range. The finding suggests that increasing the solution temperature the relaxation pathway remains unchanged. The absorption band of the second intermediate showing up within the first 2 ps cannot be distinguished from that of the solvated electron. It is assigned to a solvated atom:electron pair $(I{:}e^-)_{hyd}$. The subsequent slower dynamics indicated by an absorption decrease is found strongly temperature-dependent and explained by a competition of pair dissociation and geminate recombination. The relaxation dynamics is described by diffusion of the particles in presence of attractive interaction described by a Morse potential with depth of about $850 \pm 100\ cm^{-1}$. The extracted full halfwidth of the potential well decrease from 2.6 Å at 25 °C to 2.0 Å at 75 °C.

References

[1] E.R. Barthel, I.B. Martini, B.J. Schwartz, J. Chem. Phys. 112 (2000) 9433.
[2] F.H. Long, H. Lu, K.B. Eisenthal, Chem. Phys. Lett. 169 (1990) 165.
[3] Y. Gauduel, H. Galabert, M. Ashokkumar, Chem. Phys. 197 (1995) 167.
[4] H. Iglev, R. Laenen, A. Laubereau, Chem. Phys. Lett. 389 (2004) 427.
[5] M.J. Blandamer, M.F. Fox, Chem. Rev. 70 (1970) 59.
[6] G. Markovich, S. Pollak, R. Giniger, O. Cheshnovsky, J. Chem. Phys. 101 (1994) 9344.
[7] J. Baik, J. Kim, D. Majumdar, K.S. Kim, J. Chem. Phys. 110 (1999) 9116.
[8] Y. Gauduel, S. Pommeret, A. Antonetti, J. Phys. Condens. Matter 2 (1990) 171.
[9] M. Assel, R. Laenen, A. Laubereau, Chem. Phys. Lett. 289 (1998) 267.
[10] H. Lu, F.H. Long, K.B. Eisenthal, J. Opt. Soc. Am. B 7 (1990) 1511.
[11] F.H. Long, X. Shi, H. Lu, K.B. Eisenthal, J. Phys. Chem. 98 (1994) 7252.
[12] W.-S. Sheu, P.J. Rossky, Chem. Phys. Lett. 202 (1993) 186.
[13] W.-S. Sheu, P.J. Rossky, J. Phys. Chem. 100 (1996) 1295.
[14] D. Borgis, A. Staib, J. Chem. Phys. 104 (1996) 4776.
[15] A. Staib, D. Borgis, J. Chem. Phys. 104 (1996) 9027.
[16] J.A. Kloepfer, V.H. Vilchiz, V.A. Lenchenkov, S.E. Bradforth, Chem. Phys. Lett. 298 (1998) 120.
[17] J.A. Kloepfer, V.H. Vilchiz, V.A. Lenchenkov, A.C. Germaine, S.E. Bradforth, J. Chem. Phys. 113 (2000) 6288.
[18] J.A. Kloepfer, V.H. Vilchiz, V.A. Lenchenkov, X. Chen, S.E. Bradforth, J. Chem. Phys. 117 (2002) 766.
[19] E.B. Krissinel, N. Agmon, J. Comput. Chem. 17 (1996) 1085.
[20] M. Raytchev, E. Pandurski, I. Buchvarov, C. Modrakowski, T. Fibig, J. Phys. Chem. A 107 (2003) 4592.
[21] K. Ekvall, P. van der Meulen, C. Dhollande, L.-E. Berg, J. Appl. Phys. 87 (2000) 2340.
[22] F.-Y. Jou, G.R. Freeman, J. Phys. Chem. 83 (1979) 2383.
[23] R.A. Crowell, R. Lian, I.A. Shkrob, D.M. Bartels, X. Chen, S.E. Bradforth, J. Chem. Phys. 120 (2004) 11712.
[24] D. Madsen, C.L. Thomsen, J. Thogersen, S.R. Keiding, J. Chem. Phys. 113 (2000) 1126.
[25] P. Debye, J.O. Edwards, J. Chem. Phys. 20 (1952) 236.
[26] E. Pines, D. Huppert, N. Agmon, J. Chem. Phys. 88 (1988) 5620.
[27] C. Bressler, M. Saes, M. Chergui, D. Grolimund, R. Abela, P. Pattison, J. Chem. Phys. 116 (2002) 2955.
[28] L. Kevan, Acc. Chem. Res. 14 (1981) 138.
[29] S. Koneshan, J.C. Rasaiah, R.M. Lynden-Bell, S.H. Lee, J. Phys. Chem. B 102 (1998) 4193.
[30] K.H. Schmidt, P. Han, D.M. Bartels, J. Phys. Chem. 99 (1995) 10530, 102 (1998) 4193.
[31] W.H. Press, B.P. Flannery, S.A. Teukolsky, W.T. Vetterling, Numerical Recipes, Cambridge University Press, Cambridge, 1986.
[32] R. DeBiase, J.D. Elliot, T.E. Hartnett, ACS Symp. Ser. 303 (1986) 155.

Communications

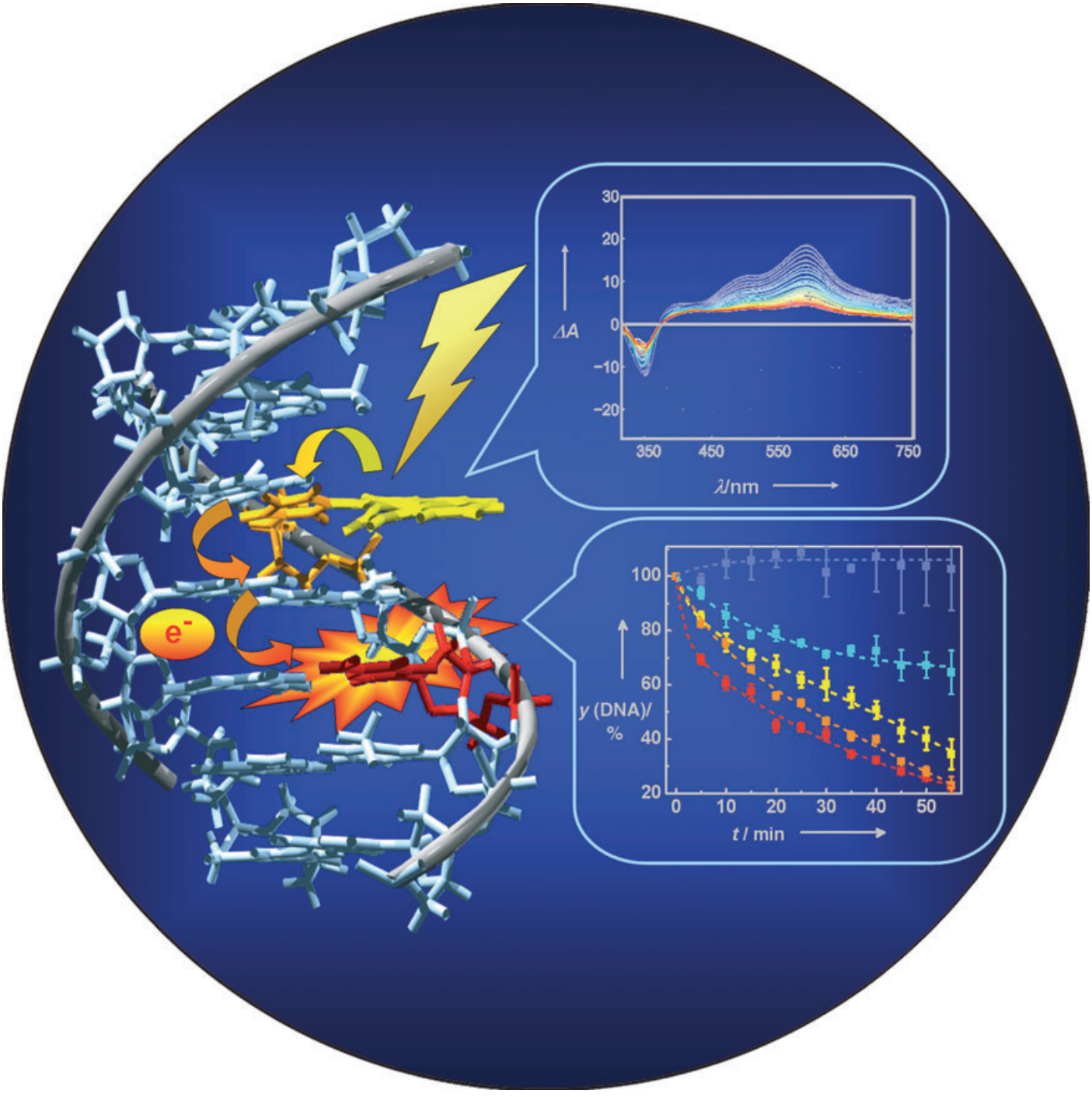

The reductive electron transfer (ET) in DNA can be studied by ultrafast time-resolved measurements combined with chemically probed DNA-strand-cleavage experiments. Owing to the numerous conformations of DNA present the results show a variety of ET rates. For more information see the Communication by H.-A. Wagenknecht, T. Fiebig, et al. on the following pages.

DOI: 10.1002/anie.200462592

Electron Transfer

Real-Time Spectroscopic and Chemical Probing of Reductive Electron Transfer in DNA**

Peter Kaden, Elke Mayer-Enthart, Anton Trifonov, Torsten Fiebig, and Hans-Achim Wagenknecht**

Reductive electron-transfer (ET) processes in DNA have attracted considerable interest over the last 2–3 years.[1] The injection of an excess electron into DNA initiates a type of charge transfer which is complementary to the extensively studied oxidative hole transfer.[1,2] Recent studies[1,3–11] support the idea that the reductive type of charge transfer has a high potential for application in new nanodevices based on DNA or DNA-inspired architectures.

Until five years ago, most knowledge about excess electrons in DNA came from γ-pulse radiolysis studies.[3] However recent photochemical assays focus on the investigation of ET by chemical means:

1) Carell et al. could show that the amount of T–T dimer cleavage depends rather weakly on the distance to the electron donor.[4]
2) Giese et al. could show that a single injected electron can cleave more than one T–T dimer.[5]
3) Rokita et al. detected a significant base-sequence dependence of the ET efficiency.[6]

To date, only Lewis et al.[7] and our groups[8] have focused on the dynamics of ET processes. In refs. [1,3–8] a thermally activated electron hopping mechanism has been suggested with $C^{\bullet-}$ and $T^{\bullet-}$ as intermediates.[9] However, we could show that proton transfer interferes with ET indicating that $T^{\bullet-}$ is more likely to play a major role as an electron carrier than $C^{\bullet-}$.[10,11]

Over the last years it has become apparent that ET phenomena in DNA cannot be understood without explicitly considering the manifold of conformational states present in DNA.[12] Since ET rates strongly depend on the microscopic environment, a single kinetic rate constant might not be observed for DNA-mediated ET but rather a distribution of rates.

Herein, we present our recent efforts to study the mechanism of electron injection and subsequent interbase electron shift by combining ultrafast time-resolved measurements with chemically probed strand-cleavage experiments using 5-bromo-2′-deoxyuridine (Br-dU) as the electron acceptor.[13] Pyren-1-yl-2′-deoxyuridine (Py-dU)[14] has been applied as the electron donor, since photoexcited Py* allows the reduction of C and T.[15] Using our previously published synthetic procedures, we prepared the Py-dU-modified DNA duplexes **1**–**5** (Scheme 1).[8,16] The DNA **1** is a control duplex

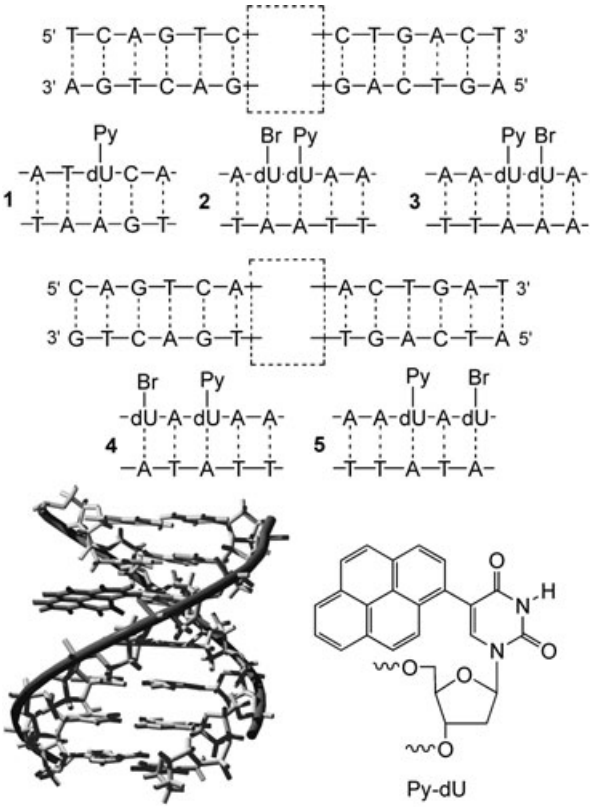

Scheme 1. Pyrene-modified DNA duplexes **1**–**5** and force field (AMBER) minimized structure of a Py-dU-modified DNA duplex (bottom left).

containing only the Py-dU chromophore with adjacent C and T bases as acceptors for the subsequent electron transfer from $dU^{\bullet-}$. The DNA duplexes **2**–**5** contain additionally the Br-dU group which is placed either adjacent to Py-dU or separated from Py-dU by one A–T base pair.

We have applied femtosecond broadband pump-probe spectroscopy[17] to explore the early time ET dynamics in DNAs **1**–**5** within a broad spectral probing window. Upon excitation at 350 nm, a pyrene-like excited state (Py-dU)* is formed which undergoes ET yielding the contact ion pair (CIP) $Py^{\bullet+}$–$dU^{\bullet-}$. Since the ET process formally represents the injection of an electron into the base stack, the injection rate can be obtained from the decay of the transient

[*] P. Kaden, E. Mayer-Enthart, Dr. H.-A. Wagenknecht
Chemistry Department
Technical University Munich
Lichtenbergstrasse 4, 85747 Garching (Germany)
Fax: (+49) 89-289-13210
E-mail: wagenknecht@ch.tum.de
A. Trifonov, Prof. Dr. T. Fiebig
Eugene F. Merkert Chemistry Center
Boston College
Chestnut Hill, MA 02467 (USA)
Fax: (+1) 617-552-2201
E-mail: fiebig@bc.edu

[**] This work was supported by the Deutsche Forschungsgemeinschaft, the Volkswagen-Stiftung, Boston College, and the Fonds der Chemischen Industrie. P.K., E.M.-E., and H.-A.W. are grateful to Professor Horst Kessler, Technical University of Munich, for the generous support.

Supporting information for this article is available on the WWW under http://www.angewandte.org or from the author.

absorption band of (Py-dU)* at 385 nm.[10b] In the CIP state the radical cation ($Py^{\bullet+}$) and the radical anion ($dU^{\bullet-}$) are electronically coupled (as a result of direct π-orbital overlap) and thus exhibit strong spectral features which extend from around 450 to approximately 750 nm. Figure 1 shows representatively the time-dependent decay of the pump-probe spectra of DNA **1** in the time range of 150–1500 ps after excitation. While the rise time of the transient absorption signals in this spectral region is about 2–3 ps (for all five DNA duplexes) the decay times vary from 100 ps to 600 ps depending on the investigated wavelength.[18] This strong kinetic dispersion in the lifetimes of the CIP state is consistent with multi-conformational states in a highly disordered medium such as DNA.[12c]

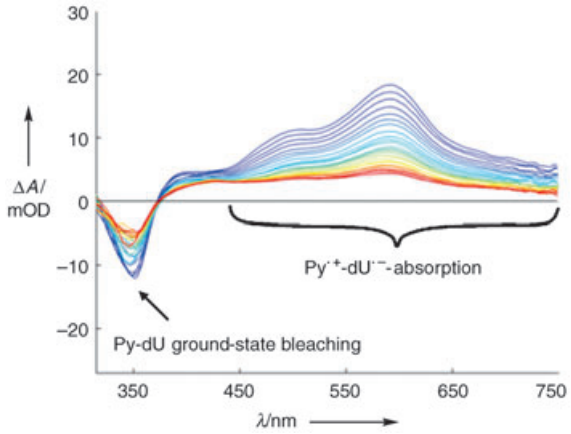

Figure 1. Time-dependent decay of the pump-probe spectra of DNA **1** (350 μM) in buffer (10 mM Na-P_i (P_i = phosphate), 250 mM NaCl, pH 7), in the time range of 150 ps (blue)–1500 ps (red) after excitation at 350 nm.

To see whether subsequent ET into the base stack competes with charge recombination in the CIP state we measured the repopulation dynamics of the Py-dU ground state. The observed dynamics are very similar in all duplexes, **1**–**5**. As shown representatively for DNA **3** (Figure 2), the recovery dynamics of the ground state (530 ps (64%), >2 ns (36%) at 364 nm) does not match the lifetime of the electron-injected CIP state (250 ps (55%), >2 ns (45%); rise time 3 ps at 485 nm) thereby suggesting that an additional decay channel (other than charge recombination!) is present from the CIP state. This result suggests that only a fraction of CIP ensembles returns to the ground state and the remaining CIP populations are reacting through a different channel.

To identify the nature of this other channel we probed the reaction product of this multistep DNA-mediated ET process chemically. Br-dU undergoes a chemical modification after its one-electron reduction which can be analyzed by piperidine-induced strand cleavage[13] and has been applied to quantify the efficiency of DNA-mediated ET processes.[6,11] Based on reduction potentials, Br-dU is not a significantly better electron acceptor than C or T[19] and thus very similar lifetimes for the CIP states were measured in DNA **1**–**3** bearing T or Br-dU directly adjacent to the Py-dU group. Hence, Br-dU is a kinetic electron trap (Scheme 2).

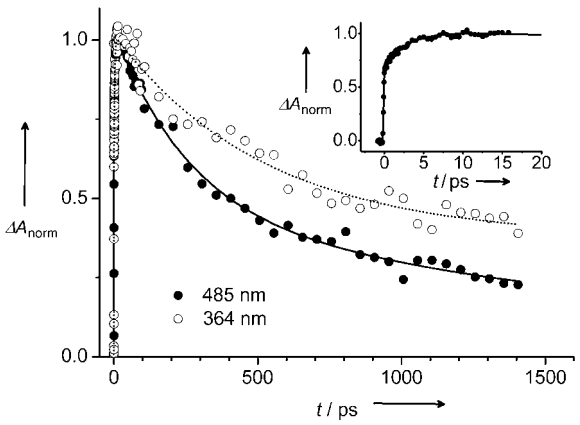

Figure 2. Pump-probe transients of DNA **3** (350 μM) in buffer (10 mM Na-P_i, 250 mM NaCl, pH 7) at two different probe wavelengths. The ground-state recovery signal (○, 364 nm) is negative but has been inverted to be visually comparable to the (positive) transient absorption of the CIP state (●, 485 nm). The inset displays the 3 ps rise of the 485 nm transient which marks the rate for electron injection.

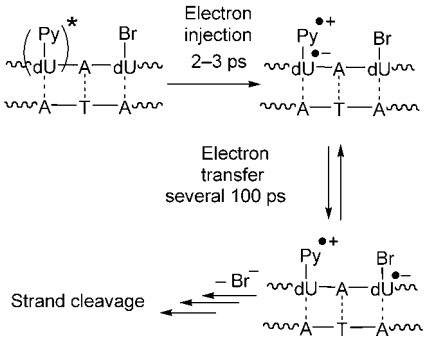

Scheme 2. Electron injection and ET in Py-dU-/Br-dU-modified duplexes.

No strand cleavage has been observed during the irradiation of DNA **1**. This result provides the important control that the observed strand cleavage in the DNA **2**–**5** can be assigned to the presence of Br-dU (Figure 3). DNAs **2** and **3** show much higher cleavage efficiency than **4** and **5**. Thus considering that strand degradation represents the chemical result of the DNA-mediated ET process, it is remarkable that just one intervening A–T base pair lowers the ET efficiency between Py-dU and Br-dU to such an extent. This result indicates that conformational control of ET in DNA becomes more dominant with increasing separations—a result which is entirely consistent with the observed dispersion of CIP lifetimes.

Several important conclusions emerge from this combined study:

1) DNA is a flexible medium with a manifold of conformational states exhibiting a wide range of reactivities and rate constants
2) As expected, the electron-injection process in our functionalized duplexes show only minor variations arising from structural inhomogeneity because it occurs between the covalently connected Py and dU moieties. Subsequent

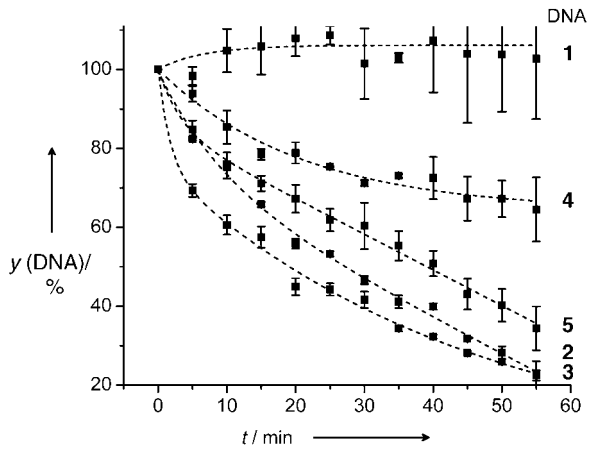

Figure 3. Analysis of the strand-cleavage experiments with DNA duplexes **1**–**5** (4 μM) in buffer (10 mM Na-P_i, 250 mM NaCl, pH 7). During the irradiation aliquots (30 μL) were collected after every 5 min, subsequently treated with piperidine (3 μL) at elevated temperature (90 °C for 30 min), and finally analyzed by HPLC. A 75-W Xe lamp with a cut-off filter (> 305 nm) has been used.

ET into the base stack is much more sensitive to structural parameters and thereby characterized by a distribution of time constants and different strand-cleavage efficiencies

3) It is important to probe both the early time events and the product states for obtaining conclusive mechanistic insight. Since DNA-mediated ET is a multistep process on various time scales, the electron-injection rates may not necessarily correlate with the strand degradation as the chemical result of DNA-mediated ET
4) The subsequent ET in the base stack occurs on the time scale of several hundred ps, therefore competing with charge recombination in our duplexes. It is reasonable to assume that subsequent migration steps will be faster since the Coulomb interaction between the excess electron and $Py^{\bullet+}$ decreases drastically with separation. Hence, our results provide a lower limit for the rate of reductive ET between single bases in DNA.

Received: November 12, 2004

Keywords: DNA · electron transfer · laser spectroscopy · pyrene

[1] Review: H.-A. Wagenknecht, *Angew. Chem.* **2003**, *115*, 2558–2565; *Angew. Chem. Int. Ed.* **2003**, *42*, 2454–2460.
[2] See reviews in: *Top. Curr. Chem.* **2004**, *236* and *237* (whole issues).
[3] Review: Z. Cai, M. D. Sevilla, *Top. Curr. Chem.* **2004**, *237*, 103–128.
[4] C. Haas, K. Kräling, M. Cichon, N. Rahe, T. Carell, *Angew. Chem.* **2004**, *116*, 1878–1880; *Angew. Chem. Int. Ed.* **2004**, *43*, 1842–1844.
[5] B. Giese, B. Carl, T. Carl, T. Carell, C. Behrens, U. Hennecke, O. Schiemann, E. Feresin, *Angew. Chem.* **2004**, *116*, 1884–1887; Angew. *Chem Int. Ed.* **2004**, *43*, 1848–1851.
[6] Most recently: T. Ito, S. E. Rokita, *Angew. Chem.* **2004**, *116*, 1875–1878; *Angew. Chem. Int. Ed.* **2004**, *43*, 1839–1842.
[7] F. D. Lewis, X. Liu, S. E. Miller, R. T. Hayes, M. R. Wasielewski, *J. Am. Chem. Soc.* **2002**, *124*, 11280–11281.
[8] N. Amann, E. Pandurski, T. Fiebig, H.-A. Wagenknecht, *Chem. Eur. J.* **2002**, *8*, 4877–4883.
[9] This mechanism was first proposed in: B. Giese, *Annu. Rev. Biochem.* **2002**, *71*, 51–70.
[10] a) R. Huber, T. Fiebig, H.-A. Wagenknecht, *Chem. Commun.* **2003**, 1878–1879; b) M. Raytchev, E. Mayer, N. Amann, H.-A. Wagenknecht, T. Fiebig, *ChemPhysChem* **2004**, *5*, 706–712.
[11] C. Wagner, H.-A. Wagenknecht, *Chem. Eur. J.* **2005**, *11*, 1871–1876.
[12] a) C. Wan, T. Fiebig, S. O. Kelley, C. R. Treadway, J. K. Barton, A. H. Zewail, *Proc. Natl. Acad. Sci. USA* **1999**, *96*, 6014–6019; b) Y. A. Berlin, A. L. Burin, L. D. A. Siebbeles, M. A. Ratner, *J. Phys. Chem. A* **2001**, *105*, 5666–5678; c) T. Renger, R. A. Marcus, *J. Phys. Chem. A* **2003**, *107*, 8404–8419; d) M. A. O'Neill, H. C. Becker, C. Z. Wan, J. K. Barton, A. H. Zewail, *Angew. Chem.* **2003**, *115*, 1676–1680; *Angew. Chem. Int. Ed.* **2003**, *42*, 5896–5900; e) M. A. O'Neill, J. K. Barton, *J. Am. Chem. Soc.* **2004**, *126*, 11471–11483; f) M. A. O'Neill, J. K. Barton, *J. Am. Chem. Soc.* **2004**, *126*, 13234–13235.
[13] a) E. Rivera, R. H. Schuler, *J. Phys. Chem.* **1983**, *87*, 3966–3971; b) H. Sugiyama, Y. Tsutsumi, I. Saito, *J. Am. Chem. Soc.* **1990**, *112*, 6720–6721; c) G. P. Cook, M. M. Greenberg, *J. Am. Chem. Soc.* **1996**, *118*, 10025–10030; d) R. Tashiro, H. Sugiyama, *J. Am. Chem. Soc.* **2003**, *125*, 15282–15283.
[14] T. L. Netzel, M. Zhao, K. Nafisi, J. Headrick, M. S. Sigman, B. E. Eaton, *J. Am. Chem. Soc.* **1995**, *117*, 9119–9128.
[15] $E(Py^{\bullet+}/Py) = 1.5$ V (vs. normal hydrogen electrode (NHE)) and $E_{00} = 3.25$ eV, see: T. Kubota, K. Kano, T. Konse, *Bull. Chem. Soc. Jpn.* **1987**, *60*, 3865–3877; gives $E(Py^{\bullet+}/Py^*) = 1.85$ V; for reduction potentials of C and T see: S. Steenken, J. P. Telo, H. M. Novais, L. P. Candeias, *J. Am. Chem. Soc.* **1992**, *114*, 4701–4709.
[16] E. Mayer, L. Valis, R. Huber, N. Amann, H.-A. Wagenknecht, *Synthesis* **2003**, 2335–2340.
[17] The laser setup has been described elsewhere: M. Raytchev, E. Pandurski, I. Buchvarov, C. Modrakowski, T. Fiebig, *J. Phys. Chem. A* **2003**, *107*, 4592–4600.
[18] The decay of the $Py^{\bullet+}dU^{\bullet-}$ transient absorption signals between 440 nm and 600 nm were adequately described using biexponential fit functions. In addition to the picosecond decay component there is a long time component (ca. 3 ns) which accounts for 20–40 % of the decay, depending on the wavelength employed.
[19] The reduction potential is only 0.06 eV lower than that of T, see ref. [18] in ref. [7]: V. P. Kadysh, Y. L. Kaminskii, L. N. Rumyantseva, V. L. Efimova, J. P. Strandish, *Khim. Geterotsikl. Soedin.* **1992**, *10*, 1404–1408.

Available online at www.sciencedirect.com
SCIENCE DIRECT®
Chemical Physics Letters 409 (2005) 277–280
CHEMICAL PHYSICS LETTERS
www.elsevier.com/locate/cplett

Real-time observation of hydrogen bond-assisted electron transfer to a DNA base

Anton Trifonov [a], Ivan Buchvarov [a], Hans-Achim Wagenknecht [*,b], Torsten Fiebig [a,*]

[a] Eugene F. Merkert Chemistry Center, Boston College, Chestnut Hill, MA 02467, United States
[b] Chemistry Department, Technical University Munich, Lichtenbergstr. 4, D-85747 Garching, Germany

Received 10 March 2005; in final form 28 April 2005
Available online 4 June 2005

Abstract

Electron transfer (ET) in a pyrene-labeled DNA base (**PydU**) has been investigated with fs-broadband pump–probe spectroscopy. By comparing the dynamics of **PydU** in a nonprotic solvent (acetonitrile) and a protic solvent (methanol) with similar dielectric properties, one can observe the formation of a planar intramolecular charge transfer state and the build-up of the pyrene radical cation population in real time. The temporal evolution of the excited state absorption spectrum provides direct evidence for a greatly enhanced ET yield in methanol. The results emphasize the critical role of hydrogen bonding for ET involving DNA bases. No spectroscopic evidence for (de)protonation of the ET product could be manifested.

1. Introduction

The interplay between electron transfer (ET) and proton transfer (PT) remains a subject of lively scientific debates, especially in biological systems [1–12]. In particular, DNA represents a unique supramolecular medium for PT and ET processes because the base pairs are structurally coupled in a Watson–Crick arrangement. Understanding the role that hydrogen-bond structures can play in driving electronic charges through the base stack is therefore critical. A promising model system for the investigation of this particular aspect of ET in DNA is **PydU**.

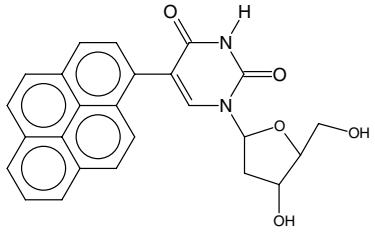

PydU

* Corresponding author. Fax: +1 617 552 2201
E-mail address: fiebig@bc.edu (T. Fiebig).

The system contains pyrene as a chromophore and redox partner in the excited state, directly linked to 2′-deoxyuridine [13,14]. The radical anion of thymidine (which is structurally very similar to uridine) and cytidine have been proposed as major intermediate charge carriers during electron transport in DNA [15]. We have recently reported extensive work on the photophysics of **PydU** (and its cytidine analogue) both in DNA [12,16] and in aqueous solutions [9–11] which demonstrated the significance of protonation concomitant to the reduction of dT and dC. Although these results have relevant implications for electron migration through DNA they have been obtained in water which has a polarity not typical for the inner part of DNA, and under nonphysiological pH conditions.

In this Letter, we report femtosecond dynamics of **PydU** in methanol (MeOH) and acetonitrile (MeCN), typical solvents *without* (MeCN) and *with* hydrogen bonding capabilities (MeOH). By comparing the ET dynamics in these solvents one can address the specific role of a proton donating and accepting medium on the ET process (as found in Watson–Crick base pairs). In 1995, Netzel et al. [14] studied the steady state fluorescence and nanosecond fluorescence lifetime of **PydU**

0009-2614/$ - see front matter © 2005 Elsevier B.V. All rights reserved.
doi:10.1016/j.cplett.2005.05.009

in MeOH and MeCN. It was proposed that ET from Py* to dU should be more favorable in MeOH than in MeCN because of a proton-coupled electron transfer (PCET) process.

Combining the electrochemical potentials $E(Py^{\bullet+}/Py) = 1.5$ V [17] and $E(dT/dT^{\bullet-}) = -1.8$ V (vs. NHE) [18], the driving force ΔG for the ET process in **PydU** is ~0.05 eV (using $E_{00} = 3.25$ eV for Py* [17]) – if Coulombic stabilization is neglected. Netzel et al. concluded that the formation of $Py^{\bullet+}dU(H)^{\bullet}$ is thermodynamically exergonic whereas the formation of $Py^{\bullet+}dU^{\bullet-}$ is endergonic. Consequently, in MeCN no ET reaction would be possible. We have applied femtosecond broadband pump–probe spectroscopy to illuminate the early time excited state dynamics in **PydU** after optical pumping in both MeOH and MeCN.

2. Experimental

Our femtosecond pump–probe setup and the details of the data processing procedure are described elsewhere [19]. Here, we will only give a brief overview. The samples were exited by pump pulses at 345 nm. The changes in optical density were probed by a femtosecond white-light continuum (WLC) generated by tight focusing of a small fraction of the output of a commercial Ti:Sa based pump laser (CPA-2001, Clark-MXR) into a 3 mm calcium fluoride (CaF_2) plate. The obtained WLC provides a usable probe source between 350 and 1000 nm. The WLC was split into two beams (probe and reference) and focused into the sample using reflective optics. After passing through the sample both probe and reference were spectrally dispersed and simultaneously detected on a CCD sensor. The pump pulse (345 nm, 1 kHz, 400 nJ) was generated by frequency doubling of the compressed output of a commercial NOPA system (Clark-MXR, 690 nm, 12 μJ, 40 fs). The overall time resolution of the setup is determined by the cross correlation function between pump and probe pulses which is typically 100–120 fs (fwhm, assuming a Gaussian lineshape). A spectral resolution of 7–10 nm was obtained. All measurements were performed with magic angle (54.7°) setting for the polarization of pump with respect to the probe pulses. A sample cell with 1.25 mm fused silica windows and a light path of 1 mm was used for all measurements. No indications for degradation of the samples were found. The sample concentration was <1 mM.

The synthesis and characterization of **PydU** was reported elsewhere [9].

3. Results and discussion

After photoexcitation **PydU** undergoes an intramolecular ET which results in the formation of the contact ion pair (CIP) $Py^{\bullet+}$–$dU^{\bullet-}$. There are two categories of electronic transitions that can be observed in transient absorption spectra of strongly coupled contact ion pairs [20,21].

Local radical absorption bands are most commonly discussed when transient absorption spectroscopy is applied to charge transfer systems. The bands are usually very similar to those observed in separated $Py^{\bullet+}$ or $dU^{\bullet-}$ reference systems and therefore straightforward to interpret. The interchromophore (IC) transitions in Scheme 1 are reverse charge-transfer (RCT) transitions which lead to nonpolar, locally excited states. RCT absorption is analogous to exciplex emission since both processes involve charge recombination. Their intensities are largely dependent on the electronic coupling between Py and dU and should therefore reflect nuclear motions and structural changes that alter this coupling. The temporal evolution of RCT absorption bands can be regarded as a pendant to time-resolved emission spectra.

Fig. 1 reveals the different characteristics of local and IC bands for **PydU** by showing the pump–probe spectra of **PydU** in three different solvents, 20 ps after photoexcitation. The band around 380 nm (inset)

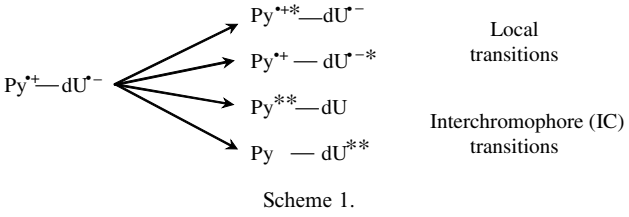

Scheme 1.

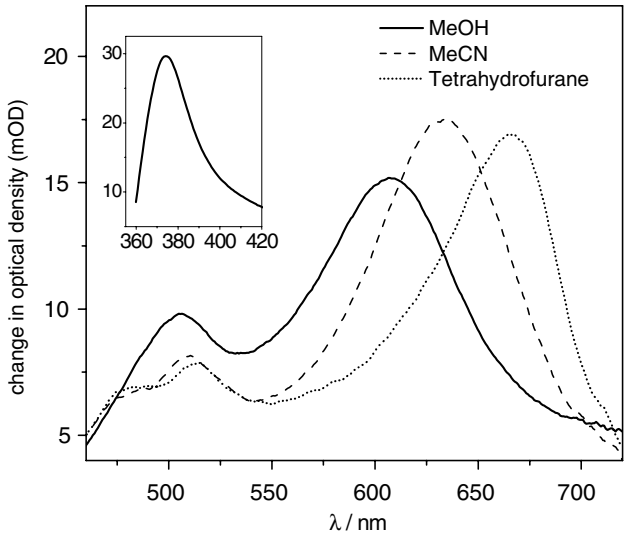

Fig. 1. Pump–probe spectra of **PydU** in three different solvents, 20 ps after excitation at 345 nm. One can clearly distinguish the solvent-independent (local) pyrenyl transitions and the strongly solvent-dependent CIP state absorption bands (reverse charge transfer). The inset shows the characteristic Py* absorption band around 375 nm. See text for details.

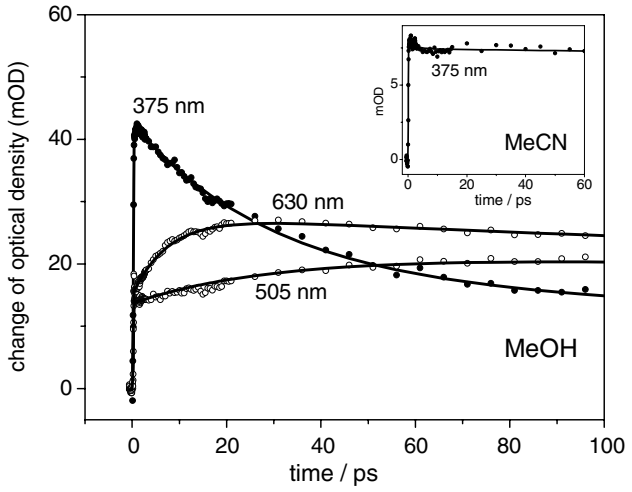

Fig. 2. Time-dependent transient absorption signals of **PydU** in MeOH at three selected wavelengths. Note that the decay time at 375 nm (35 ps, 63%) matches the rise time of the $Py^{\bullet+}$ absorption at 505 nm. The rise time of the IC band (7 ps at 630 nm) is convoluted with the spectral shifting dynamics (see Fig. 3b). Inset: **PydU** in MeCN. The population decay of Py* probed at 375 nm. The short decay component (~4 ps) represents the ET equilibration dynamics (see text).

which reflects the absorption of the initially excited pyrenyl state (Py*) [22] and the bands between 450 and 510 nm (local pyrenyl bands, $Py^{\bullet+}$/Py*) are virtually solvent independent because the underlying transitions are not accompanied by changes in the molecular dipole moments. In contrast, the broad (RCT) absorption band between 600 and 670 nm is strongly solvent dependent. Note that this band exhibits a solvatochromic shift, similar to the shift observed in fluorescence spectroscopy. However, in fluorescence spectroscopy charge transfer bands shift towards longer wavelengths with increasing solvent polarity while a reverse behavior (i.e., shifting towards shorter wavelengths) is observed in transient absorption. One of the key advantages of fs-broadband pump–probe spectroscopy over fluorescence spectroscopy is that both local and interchromophore transitions can be monitored simultaneously which provides a large amount of information about the molecular system evolving on the excited state potential energy surface. In fact, the intensity of the IC band depends on the magnitude of the electronic coupling between the two aromatic subsystems and therefore on the conformation of **PydU**. A rise in the intensity suggests the transition from a twisted to a more planar geometry with enhanced π-electron overlap between Py and dU [23].

In MeOH the single-wavelength kinetics (Fig. 2) indicate that the initial Py* population (~375 nm) decays with a 35 ps time component which matches the rise time of the $Py^{\bullet+}$ absorption at 505 nm. The fact that the ET product ($Py^{\bullet+}$) is rising on the same time scale as the IC band (see Fig. 3b) clearly indicates that the ET process is coupled to a structural change in the molecule. In other words, while the molecule is moving towards a more planar geometry, more charge is transferred from Py* to dU. In MeCN, on the other hand, one observes a fast equilibration between Py* and $Py^{\bullet+}$ on the time scale of a few ps which is typical for electron donor (D)/acceptor (A) systems with small driving forces where the ET is incomplete. The inset of Fig. 2 clearly shows the biexponential decay of the Py* population (probed at 375 nm) where the fast component ~4 ps is characterizing the equilibration dynamics. Subsequently, the molecule is undergoing a similar structural relaxation as observed in MeOH, indicated by the rise of the IC band around 630 nm.

In contrast to the MeOH data, however, the IC band in MeCN is not exhibiting a blue shift (see Fig. 3a). The absence of the spectral shift in MeCN indicates that the shift originates from MeOH-specific solute–solvent

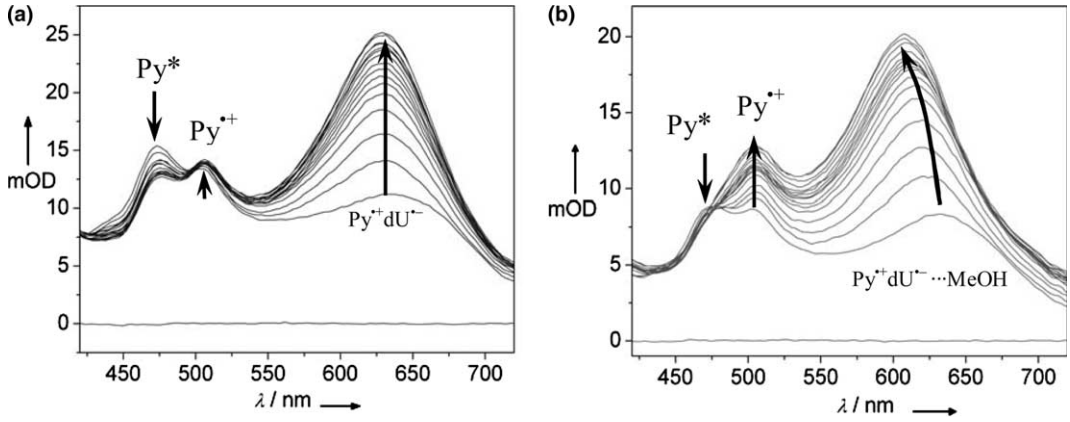

Fig. 3. Time-dependent evolution of the pump–probe spectrum of **PydU** in (a) MeCN and (b) MeOH between 3 and 20 ps after excitation. The time difference between each spectrum is 1 ps.

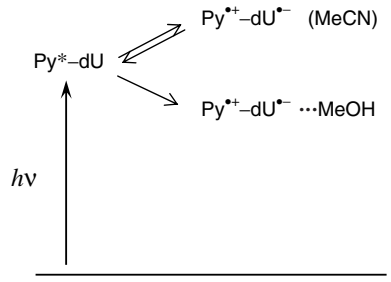

Scheme 2.

interactions. These interactions are likely caused by the hydrogen-bond network, particularly the H-bonds between MeOH and dU/dU$^{\bullet-}$. However, the protonation of dU$^{\bullet-}$ by MeOH should be thermodynamically unfavorable. This conclusion is based on the pK_a value of 6.9 which was determined by Steenken [24] for the protonated thymidine radical dT(H)$^{\bullet}$ which thus represents a stronger acid than MeOH (pK_a 15.7). Based on the difference in pK_a values one would expect a rate constant for dU$^{\bullet-}$ protonation in the order of milliseconds, i.e., several orders of magnitude slower than the lifetime of the CIP state [25]. Instead of PCET we therefore propose a hydrogen bond-assisted ET mechanism where hydrogen bonding facilitates the transfer of electronic charge from Py* to dU. While protons will certainly be 're-adjusted' within the hydrogen bond network there should not be a kinetically distinguishable Py$^{\bullet+}$dU(H)$^{\bullet}$ species based on thermodynamic arguments (see Scheme 2).

The results presented here demonstrate the relevance of a proton donating/accepting environment for ET dynamics, especially in the small driving force regime. Even if protonation/deprotonation of the ionic intermediates is thermodynamically not feasible, the hydrogen bonding interactions are capable of driving the charge to the acceptor site. Such hydrogen-bond-assisted ET mechanisms are likely to play a vital role in many biological ET reactions, especially where ΔG is small.

Acknowledgments

The work was supported by Boston College, and by the Deutsche Forschungsgemeinschaft (Emmy-Noether Program Fi-721/3-1, 3-4, and Wa-1386/7-3).

References

[1] J.M. Mayer, Annu. Rev. Phys. Chem. 55 (2004) 363.
[2] S.K. Pal, A.H. Zewail, Chem. Rev. 104 (2004) 2099.
[3] J. Waluk, Acc. Chem. Res. 36 (2003) 832.
[4] C.J. Chang, M.C.Y. Chang, N.H. Damrauer, D.G. Nocera, Biochim. Biophys. Acta-Bioener. 1655 (2004) 13.
[5] M.Y. Okamura, M.L. Paddock, M.S. Graige, G. Feher, Biochim. Biophys. Acta-Bioenerg. 1458 (2000) 148.
[6] R.I. Cukier, J. Phys. Chem. 100 (1996) 15428.
[7] R.I. Cukier, D.G. Nocera, Annu. Rev. Phys. Chem. 49 (1998) 337.
[8] S. Steenken, Biol. Chem. 378 (1997) 1293.
[9] N. Amann, E. Pandurski, T. Fiebig, H.-A. Wagenknecht, Angew. Chem., Int. Ed. 41 (2002) 2978.
[10] R. Huber, T. Fiebig, H.A. Wagenknecht, Chem. Commun. (2003) 1878.
[11] M. Raytchev, E. Mayer, N. Amann, H.A. Wagenknecht, T. Fiebig, Chem. Phys. Chem. 5 (2004) 706.
[12] P. Kaden, E. Mayer-Enthart, A. Trifonov, T. Fiebig, H.-A. Wagenknecht, Angew. Chem., Int. Ed. 44 (2005) 1636.
[13] T.L. Netzel, M. Zhao, K. Nafisi, J. Headrick, M.S. Sigman, B.E. Eaton, J. Am. Chem. Soc. 117 (1995) 9119.
[14] T.L. Netzel, K. Nafisi, J. Headrick, B.E. Eaton, J. Phys. Chem. 99 (1995) 17948.
[15] B. Giese, Annu. Rev. Biochem. 71 (2002) 51.
[16] N. Amann, E. Pandurski, T. Fiebig, H.-A. Wagenknecht, Chem. Eur. J. 8 (2002) 4877.
[17] T. Kubota, K. Kano, T. Konse, Bull. Chem. Soc. Jpn. 60 (1987) 3865.
[18] T. Fiebig, C. Wan, A.H. Zewail, Chem. Phys. Chem. 3 (2002) 781.
[19] M. Raytchev, E. Pandurski, I. Buchvarov, C. Modrakowski, T. Fiebig, J. Phys. Chem. A 107 (2003) 4592.
[20] M. Ottolenghi, Acc. Chem. Res. 6 (1973) 153.
[21] E. Pandurski, T. Fiebig, Chem. Phys. Lett. 357 (2002) 272.
[22] M.F.M. Post, J. Langelaar, J.D.W.V. Voorst, Chem. Phys. Lett. 10 (1971) 468.
[23] D. Mank, M. Raytchev, S. Amthor, C. Lambert, T. Fiebig, Chem. Phys. Lett. 376 (2003) 201.
[24] S. Steenken, Free Rad. Res. Commun. 16 (1992) 349.
[25] M. Eigen, Angew. Chem., Int. Ed. 3 (1964) 1.

J|A|C|S
ARTICLES
Published on Web 07/07/2005

Photoinduced Charge Transfer Processes along Triarylamine Redox Cascades

Christoph Lambert,*,† Jürgen Schelter,† Torsten Fiebig,*,‡ Daniela Mank,‡ and Anton Trifonov‡

Contribution from the Institut für Organische Chemie, Bayerische Julius-Maximilians-Universität Würzburg, Am Hubland, D-97074 Würzburg, Germany, and Boston College, Department of Chemistry, Eugene F. Merkert Chemistry Center, 2609 Beacon Street, Chestnut Hill, MA 02467

Received February 23, 2005; E-mail: lambert@chemie.uni-wuerzburg.de; Fiebig@bc.edu

Abstract: In this paper, we describe the synthesis and photophysical properties of a series of acridine−triarylamine redox cascades. These cascades were designed in order to promote photoinduced hole transfer from an acridine fluorophore into an adjacent triarylamine. The excited dipolar state then injects a hole into the triarylamine redox cascade. Subsequently, the hole migrates along the redox gradient which was tuned by the substituents attached to the triarylamine redox centers. The rate of hole migration was determined by fluorescence lifetime measurements and is in the ns regime and depends strongly on the solvent polarity. The photophysical processes were also investigated by femtosecond broadband pump−probe spectroscopy. Our studies reveal different dynamic processes in the cascades depending on the solvent polarity, e.g., direct charge separation after photoexcitation vs a two step hole transfer mechanism.

Introduction

Electron transfer (ET) or, more precisely, hole transfer (HT) processes in triarylamine based systems have thoroughly been investigated in the past.[1−4] Owing to the relatively simple synthetic accessibility and the stability of oxidized triarylamines these units are widely used as hole transport components in optoelectronic devices.[5−10] But also on a molecular level, triarylamines have attracted considerable interest: the triarylamine group was used as the charge bearing unit in organic mixed valence compounds for intramolecular ET studies[1−4,11−15] as well as in organic high spin systems for organic ferromagnets.[16−26] One-dimensional systems with two triarylamine groups have been investigated but also cascades with many triarylamines in a row[27−29] up to polymers[11,30] and dendrimers.[31−36] In the present study, we will focus on triarylamine cascades in which a hole can be transferred along a redox gradient. The redox centers of these cascades are built up from triarylamines connected by acetylene spacers. The hole is injected in the cascade by photoinduced electron transfer (PET) of an excited acridine chromophore. Triarylamines were used as redox centers for the above-mentioned reasons but also

† Bayerische Julius-Maximilians-Universität Würzburg.
‡ Boston College.

(1) Lambert, C.; Nöll, G.; Schelter, J. *Nat. Mater.* **2002**, *1*, 69−73.
(2) Lambert, C.; Nöll, G. *Chem. Eur. J.* **2002**, *8*, 3467−3477.
(3) Lambert, C.; Nöll, G. *J. Am. Chem. Soc.* **1999**, *121*, 8434−8442.
(4) Lambert, C.; Amthor, S.; Schelter, J. *J. Phys. Chem. A* **2004**, *108*, 6474−6486.
(5) Zhao, H. T. C.; Thayumanavan, S. *Tetrahedron Lett.* **2001**, *42*, 4421−4424.
(6) Fujikawa, H.; Tokito, S.; Taga, Y. *Synth. Met.* **1999**, *91*, 161−162.
(7) Thayumanavan, S.; Barlow, S.; Marder, S. R. *Chem. Mater.* **1997**, *9*, 3231−3235.
(8) Koene, B. E.; Loy, D. E.; Thompson, M. E. *Chem. Mater.* **1998**, *10*, 2235−2250.
(9) Weiss, D. S.; Cowdery, J. R.; Young, R. H. In *Electron Transfer in Chemistry*; Balzani, V., Ed.; Wiley-VCH: Weinheim, 2001; Vol. 5; pp 379−471.
(10) Thelakkat, M. *Macromol. Mater. Eng.* **2002**, *287*, 442−461.
(11) Lambert, C.; Nöll, G. *Synth. Met.* **2003**, *139*, 57−62.
(12) Lambert, C.; Nöll, G.; Hampel, F. *J. Phys. Chem. A* **2001**, *105*, 7751−7758.
(13) Lambert, C.; Nöll, G.; Kriegisch, V.; Zabel, M.; Hampel, F.; Schmälzlin, E.; Bräuchle, C.; Meerholz, K. *Chem. Eur. J.* **2003**, *9*, 4232−4239.
(14) Bonvoisin, J.; Launay, J.-P.; Verbouwe, W.; Van der Auweraer, M.; De Schryver, F. C. *J. Phys. Chem.* **1996**, *100*, 17079−17082.
(15) Bonvoisin, J.; Launay, J.-P.; Van der Auweraer, M.; De Schryver, F. C. *J. Phys. Chem.* **1994**, *98*, 5052−5057, see also correction **1996**, *100*, 18006.
(16) Blackstock, S. C.; Selby, T. D. In *Magnetic Properties of Organic Materials*; Lahti, P. M., Ed.; Marcel Dekker: New York, 1999; pp 165−178.
(17) Stickley, K. R.; Blackstock, S. C. *Tetrahedron Lett.* **1995**, *36*, 1585−1588.
(18) Stickley, K. R.; Blackstock, S. C. *J. Am. Chem. Soc.* **1994**, *116*, 11576−11577.
(19) Selby, T. D.; Blackstock, S. C. *Org. Lett.* **1999**, *1*, 2053−2055.
(20) Wienk, M. M.; Janssen, R. A. *J. Am. Chem. Soc.* **1997**, *119*, 4492−4501.
(21) Bushby, R.-J. In *Magnetism: Molecules to Materials II*; Miller, J. S., Drillon, M., Eds.; Wiley-VCH: Weinheim, Germany, 2001; pp 149−187.
(22) Selby, T. D.; Blackstock, S. C. *J. Am. Chem. Soc.* **1999**, *121*, 7152−7153.
(23) Selby, T. D.; Stickley, K. R.; Blackstock, S. C. *Optics Lett.* **2000**, *2*, 171−174.
(24) Ito, A.; Urabe, M.; Tanaka, K. *Angew. Chem.* **2003**, *115*, 951−954.
(25) Hauck, S. I.; Lakshmi, K. V.; Hartwig, J. F. *Org. Lett.* **1999**, *1*, 2057−2060.
(26) Michinobu, T.; Takahashi, M.; Tsuchida, E.; Nishide, H. *Chem. Mater.* **1999**, *11*, 1969−1971.
(27) Selby, T. D.; Kim, K.-Y.; Blackstock, S. C. *Chem. Mater.* **2002**, *14*, 1685−1690.
(28) Kim, K.-Y.; Hassenzahl, J. D.; Selby, T. D.; Szulczewski, G. J.; Blackstock, S. C. *Chem. Mater.* **2002**, *14*, 1691−1694.
(29) Plater, M. J.; Jackson, T. *Tetrahedron* **2003**, *59*, 4687−4692.
(30) Ohsawa, Y.; Ishikawa, M.; Miyamoto, T.; Murofushi, Y.; Kawai, M. *Synth. Met.* **1987**, *18*, 371−374.
(31) Louie, J.; Hartwig, J. F.; Fry, A. J. *J. Am. Chem. Soc.* **1997**, *119*, 11695−11696.
(32) Katsuma, K.; Shirota, Y. *Adv. Mater.* **1998**, *10*, 223−226.
(33) Wu, I.-Y.; Lin, J. T.; Tao, Y.-T.; Balasubramaniam, E. *Adv. Mater.* **2000**, *12*, 668−669.
(34) Chen, C. H.; Shi, J.; Tang, C. W. *Macromol. Symp.* **1997**, *125*, 1−48.
(35) Selby, T. D.; Blackstock, S. C. *J. Am. Chem. Soc.* **1998**, *120*, 12155−12156.
(36) Krys, B.; S, T. *J. Org. Chem.* **2003**, *68*, 5559−67.

10.1021/ja0511570 CCC: $30.25

Chart 1

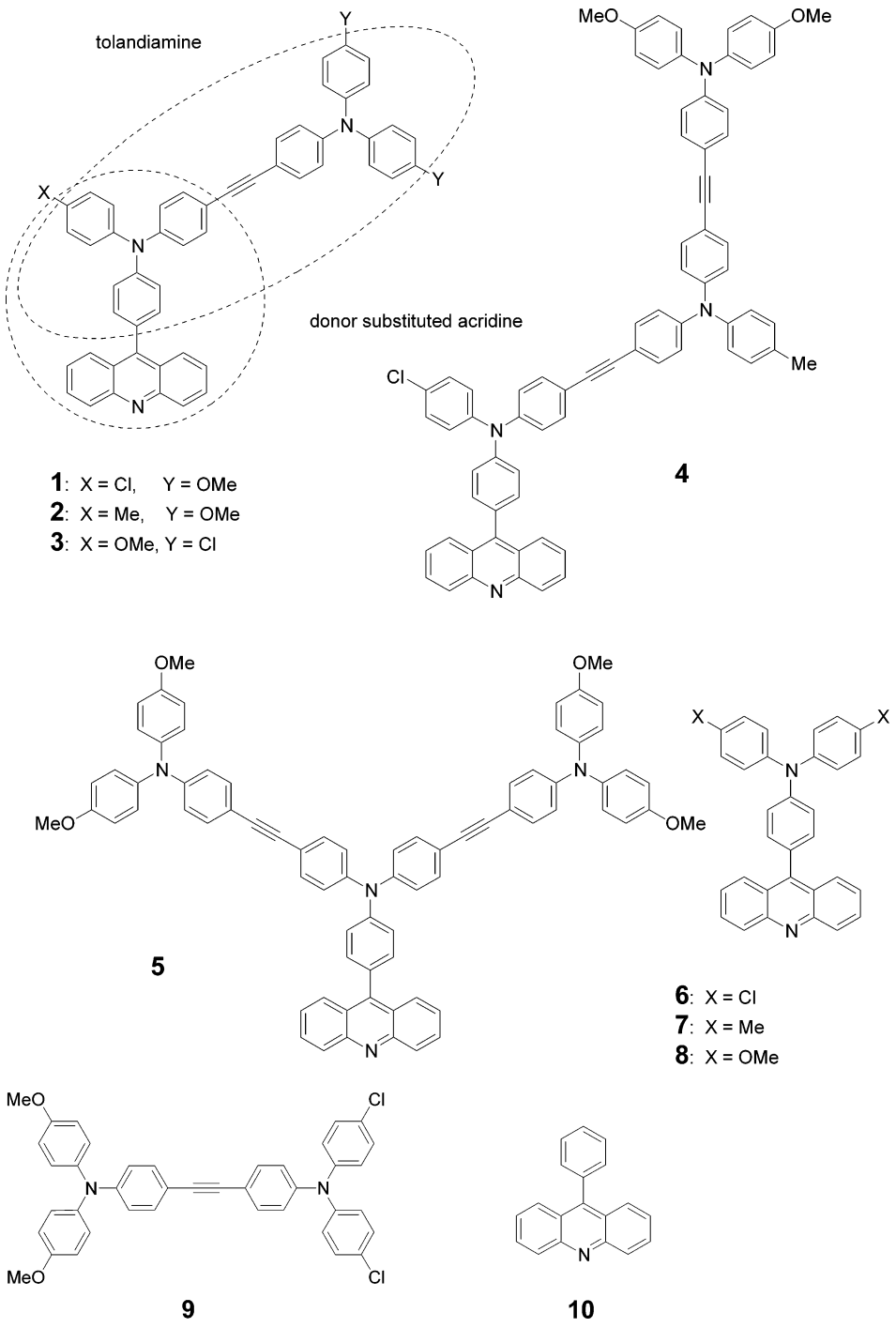

because triarylamines possess relatively low internal reorganization energy.[37,38] Therefore, HT processes are expected to be rather quick which will favor photoinduced charge separation processes over other competing processes. On the other hand, if the back electron transfer is in the Marcus inverted region, a small reorganization energy will slow the back electron transfer and will lead to long-lived charge separated states. Our investigations illustrate a first step how to construct an artificial light-driven system based on triarylamines that might be able to induce the long-range separation of opposite charges upon irradiation. So far, most systems that aim to mimic basic aspects of natural photosynthetic reaction centers use porphyrine chromophores in close analogy to their natural examples.[39] Only a few systems are known that incorporate triarylamine units.[40−48]

(37) Eberson, L. *Electron-Transfer Reactions in Organic Chemistry*; Springer: Berlin (Germany), 1987.
(38) Lin, B. C.; Cheng, C. P.; Lao, Z. P. M. *J. Phys. Chem. A* **2003**, *107*, 5241−5251.
(39) Gust, D.; Moore, T. A.; Moore, A. L. In *Electron Transfer in Chemistry*; Balzani, V., Ed.; Wiley-VCH: Weinheim (Germany), 2001; Vol. 3; p 272.
(40) Ramos, A. M.; Meskers, S. C. J.; van Hal, P. A.; Knol, J.; Hummelen, J. C.; Janssen, R. A. J. *J. Phys. Chem. A* **2003**, *107*, 9269−9283.
(41) Ramos, A. M.; Beckers, E. H. A.; Offermans, T.; Meskers, S. C. J.; Janssen, R. A. J. *J. Phys. Chem. A* **2004**, *108*, 8201−8211.
(42) Ohno, T.; Moriwaki, K.; Miyata, T. *J. Org. Chem.* **2001**, *66*, 3397−3401.
(43) Lor, M. V.; Lucien; Pilot, R.; Fron, E.; Jordens, S.; Schweitzer, G.; Weil, T.; Müllen, K.; Verhoeven, J. W.; Van der Auweraer, M. V.; De Schryver, F. C. *J. Phys. Chem. B* **2004**, *108*, 10721−10731.

In this study, we refrain from employing subunits that resemble the well-known natural systems and turn to completely artificial chromophores and redox centers which are more likely to be incorporated in future optoelectronic devices that shall build up an electrical potential upon irradiation.

The cascade structures **1**−**5** which we have designed are drawn in Chart 1 together with some reference systems. The principal features of the cascade systems are the fluorescent donor substituted acridine chromophore and the triarylamine cascade. The triarylamine units are connected by triple bonds in order to ensure an essentially rigid structure of the whole cascade with fixed HT distances. To illustrate our conceptual approach we divide the chromophores into the following subunits: acridine acceptor (**A**), the first triarylamine attached to the acridine (**Tara1**), the second, and third triarylamine (**Tara2** and **Tara3**) which are farther apart; two triarylamine groups connected by a triple bond yield a tolandiamine (e.g., **Tara1**-≡-**Tara2**). While the HT distances are fixed in **1**−**3** and **5** by the almost rigid structure it is not in **4** in which the N(acridine)···N(Tara3) distance can vary between ca. 23 and 29 Å, depending on the conformer.

The donor substituted acridine fluorophore (**A-Tara1**) is a strong oxidizing agent in the first excited charge transfer (CT) singlet state. This locally excited singlet state is expected to oxidize the adjacent triarylamine moiety (**Tara2**) which is attached to the donor substituted acridine by an acetylene spacer. We use donor substituted acridine dyes because their photophysics are reasonably well understood thanks to the work of Herbich and Kapturkiewicz[49] (hereafter called HK). These authors investigated a series of dialkylamino substituted phenylacridines by fluorescence spectroscopy. The local redox potential of the triarylamine units is tuned by substituents (Cl, Me, MeO) in para position of the phenyl rings so as to form two short (**1**, **2**) and one long (**4**) cascade with downhill hole transport gradient, that is, the triarylamine moiety which is farthest apart from the acridine has the lowest redox potential, i.e., it is more easily oxidized than the triarylamines adjacent to the acridine. In a recent study, we showed that the redox potentials of triarylamine in tolandiamines may span a range of 400 mV depending on the substituents.[50] For comparison, we also synthesized a branched dendrimeric system (**5**) as well as a short cascade with uphill redox gradient (**3**). The photophysical properties of these cascades will be compared with **A-Tara1** subunits (**6**−**8**) as well as with tolandiamine (**9**) and phenylacridine (**10**).

Results and Discussion

A. Stationary Optical Properties. The absorption spectra of the **A-Tara1** species **6**−**8** show a moderately strong CT band around 25 000 cm^{-1} which can be ascribed to a charge transfer from the triarylamine donor to the acridine acceptor (see Figure 1 and Table 1).[49]

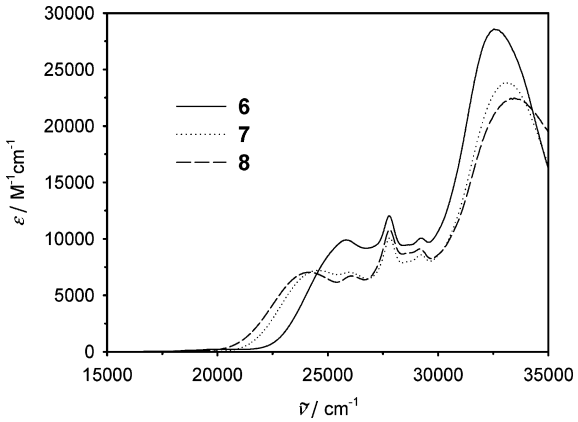

Figure 1. Absorption spectra of **6**−**8** in CH_2Cl_2.

Table 1. Absorption Maxima of **6**−**8**

	$\tilde{\nu}_{abs}/cm^{-1}$ ($\epsilon/M^{-1}cm^{-1}$)	$\tilde{\nu}_{abs}/cm^{-1}$ ($\epsilon/M^{-1}cm^{-1}$)	$\tilde{\nu}_{abs}/cm^{-1}$ ($\epsilon/M^{-1}cm^{-1}$)
	6	**7**	**8**
C_6H_{12}	26200 (10400)	25100 (9050)	24700 (6700)
Bu_2O	26100 (10300)	25100 (8490)	24600 (6830)
MTBE	26200 (10600)	25300 (8640)	24600 (7270)
1,4-dioxane	25900 (9980)	24900 (8030)	24400 (7410)
Et_2O	26100 (10700)	25300 (8210)	24700 (7580)
EtOAc	26000 (10200)	25200 (8100)	24600 (7630)
THF	26000 (9950)	24900 (7810)	24300 (7070)
CH_2Cl_2	25800 (9780)	24600 (7160)	24100 (6940)
DMF	25900 (8980)	24700 (7710)	24200 (6880)
DMSO	25700 (8560)	24400 (6550)	

The sharp peaks at ca. 26 000, 28 000, and 29 000 cm^{-1} stem from localized excitations of phenylacridine (**10**) and the broad and very intense peak at ca. 33 000 cm^{-1} is due to a localized triarylamine excitation. The CT bands are somewhat stronger red shifted with MeO substituents than with Me or Cl, that is, the donor strength of the triarylamine unit can be tuned by the para substituents attached to the phenyl rings.

The CT bands of **6**−**8** are moderately positive solvatochromic (e.g., **6**: 26 200 cm^{-1} in C_6H_{12} and 25 700 cm^{-1} in DMSO) which indicates an increase in dipole moment upon excitation. Fluorescence spectra of all compounds were measured at the excitation energy of the CT band maximum. Much in contrast to 9-phenylacridine **10** which is practically nonfluorescent, the donor substituted compounds **6**−**8** show strong fluorescence with high quantum yields (see Table 2). The fluorescence spectra of **6**−**8** are strongly positive solvatochromic and display a large Stokes shift (see e.g., Figure 2 for the fluorescence spectra of **6**, the full data set for all compounds is given in Table 2) which is stronger for **8** and **7** than for **6**. This Stokes shift indicates a major reorganization in the excited state. HK[49] explain this behavior by a solvent dependent mixing of a locally excited state and a CT state with a different degree of planarization in the excited state while the ground state is generally nonplanar. Here, we simply state that AM1 computations yield two ground-state minima for **8** that are very close in energy but differ in their relative orientation of the dianisylamino group to the acridine moiety, coplanar vs perpendicular, the latter being in accordance with the X-ray crystal structure investigation (see Supporting Information). If cyclohexane is excluded, then a plot of the fluorescence energy vs the solvent parameters according to Lippert and Mataga (eq 1)[51] yields a reasonable linear correlation (Figure 3 and Table 3). Cyclohexane is excluded as

(44) Sandanayaka, A. S. D.; Sasabe, H.; Araki, Y.; Furusho, Y.; Ito, O.; Takata, T. *J. Phys. Chem. A* **2001**, *108*, 5145−5155.
(45) Luo, H.; Fujitsuka, M.; Araki, Y.; Ito, O.; Padmawar, P.; Chiang, L. Y. *J. Phys. Chem. B* **2003**, *107*, 9312−9318.
(46) Komamine, S.; Fujitsuka, M.; Ito, O. M.; Miyata, K.; Toshiyuki; Ohno, T. *J. Phys. Chem. A* **2000**, *104*, 11497−11504.
(47) Lor, M.; Thielemans, J.; Viaene, L.; Cotlet, M.; Hofkens, J.; Weil, T.; Hampel, C.; Müllen, K.; Verhoeven, J. W.; Van der Auweraer, M.; De Schryver, F. C. *J. Am. Chem. Soc.* **2002**, *124*, 9918−9925.
(48) Sandanayaka, A. S. D.; Matsukawa, K.; Ishii, T.; Mataka, S.; Araki, Y.; Ito, O. *J. Phys. Chem. B* **2004**, *108*, 19995−20004.
(49) Herbich, J.; Kapturkiewicz, A. *J. Am. Chem. Soc.* **1998**, *120*, 1014−1029.
(50) Lambert, C.; Nöll, G. *J. Chem. Soc., Perkin Trans. 2* **2002**, 2039−2043.

Table 2. Steady State and Time Resolved Optical Properties of **1**−**8**

	$\tilde{\nu}_f$/cm^{-1}	Φ_f	τ_f/ns	k_f/10^8 s^{-1}	k_{nr}/10^8 s^{-1}	$\tilde{\nu}_f$/cm^{-1}	Φ_f	τ_f/ns	k_f/10^8 s^{-1}	k_{nr}/10^8 s^{-1}
			1					**2**		
C_6H_{12}	22400	0.23	1.5	1.5	5.1	21900	0.42	1.7	2.5	3.4
Bu_2O	20500	0.38				20000	0.53			
MTBE	19400	0.37	5.9	0.63	1.1	19100	0.49	4.8	1.0	1.0
1,4-dioxane	19500	0.49	5.4	0.91	0.94	18900	0.67	6.4	1.0	0.52
Et_2O	18100	0.10				17800	0.22			
EtOAc	17800	0.08	4.7	0.16	2.0	17500	0.27			
THF	17300	0.06	5.0	0.12	1.9	17300	0.22	5.9	0.37	1.3
CH_2Cl_2	15700	0.01	0.8	0.13	12	15500	0.02	0.7	0.28	14
PrCN										
DMF										
DMSO										
			3					**4**		
C_6H_{12}	22000	0.42	1.8	2.4	3.2	22600	0.18	1.0	1.8	8.2
Bu_2O	20000	0.51				21000	0.30			
MTBE	19000	0.67	4.9	1.4	0.68	20000	0.32	4.3	0.75	1.6
1,4-dioxane	18900	0.58	6.3	0.92	0.67	19800	0.42	4.7	0.90	1.2
Et_2O	17800	0.50	6.9	0.73	0.72	18900	0.20			
EtOAc	17300	0.36				18400	0.22	8.0	0.27	0.98
THF	17200	0.46	7.2	0.63	0.76	18300	0.13	9.2	0.14	0.95
CH_2Cl_2	15700	0.18	7.4	0.25	1.1	16000	0.02	4.8	0.032	2.1
PrCN										
DMF	14800	0.01								
DMSO										
			5					**6**		
C_6H_{12}	21800	0.40	1.9	2.1	3.2	23000	0.14	0.55	2.6	16
Bu_2O	20300	0.74	3.4	2.2	0.77	21800	0.26			
MTBE	19100	0.31	4.5	0.69	1.5	20900	0.38	1.9	2.0	3.3
1,4-dioxane	19000	0.47	6.0	0.78	0.88	20600	0.52	3.2	1.6	1.5
Et_2O	17900	0.23				20100	0.47			
EtOAc	17700	0.18	6.3	0.29	1.3	19100	0.86	6.0	1.2	0.43
THF	17400	0.15	6.9	0.22	1.2	19200	0.74	5.7	1.5	0.24
CH_2Cl_2	15300	0.01	1.0	0.10	9.9	18200	0.90	9.3	0.97	0.10
PrCN						17100	0.74			
DMF						16500	0.72	11.4	0.63	0.25
DMSO						15900	0.65	11.6	0.56	0.30
			7					**8**		
C_6H_{12}	22100	0.28	1.3	2.2	5.5	21300	0.34	2.0	1.7	3.3
Bu_2O	20400	0.41				18900	0.56			
MTBE	19400	0.56	4.9	1.1	0.90	17800	0.66	6.7	0.99	0.51
1,4-dioxane	19000	0.72				17600	0.71			
Et_2O	18300	0.63				16600	0.34			
EtOAc	17700	0.67				16100	0.20			
THF	17700	0.76	8.9	0.86	0.27	16000	0.29	6.2	0.47	1.1
CH_2Cl_2	16100	0.58	12.4	0.46	0.34	14800	0.05	2.4	0.21	4.0
PrCN	15600	0.28								
DMF	15000	0.10								
DMSO	14800	0.07	2.8	0.23	3.3					

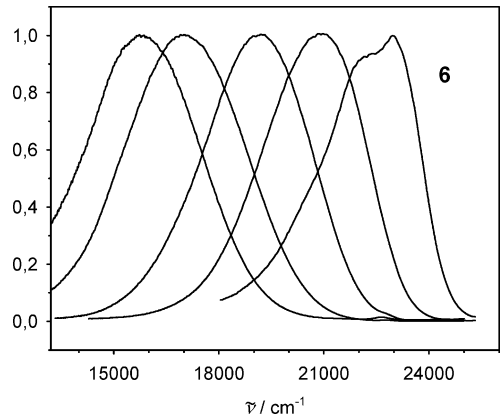

Figure 2. Normalized fluorescence spectra (solid lines) of **6** from left to right in DMSO, PrCN, THF, MTBE, C_6H_{12}.

it gives values which are significantly too low; this effect might have to do with changes in solute geometry in this very apolar solvent. In eq 1 $\tilde{\nu}_f$ is the fluorescence energy maximum, $\tilde{\nu}_f^{vac}$ is the fluorescence energy maximum in vacuum, μ_g and μ_e are the ground state and excited-state dipole moments, respectively, which are assumed to be parallel, a_0 is the effective radius of the solute, n is the refractive index and ϵ is the permittivity of the solvent. The slopes of the Lippert−Mataga correlations for **6**−**8** are quite similar (see Figure 3 and Table 3). An effective solute radius of 7 Å (estimated from an AM1 computation) yields a dipole moment of 31 D for the excited state. The ground state has a dipole moment of 4−5 D depending on the conformation (see above) estimated by AM1 computations. Thus, the dipole moment difference of ca. 26 D roughly corresponds to the transfer of a unit charge from the triarylamine nitrogen to the acridine center. Therefore, we can best describe the CT state by **(A)**$^-$**-(Tara1)**$^+$. In general, the stationary

(51) Suppan, P.; Ghoneim, N. *Solvatochromism*; The Royal Society of Chemistry: Cambridge, 1997.

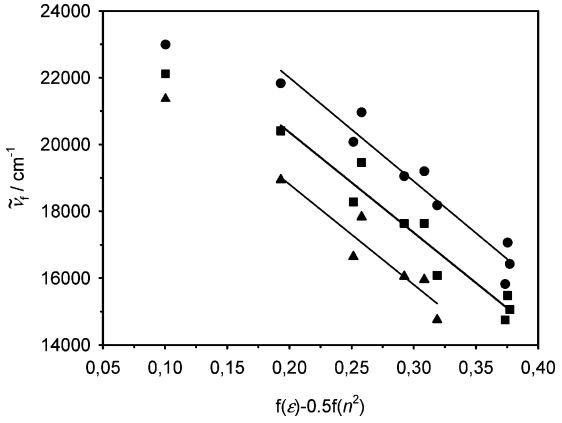

Figure 3. Lippert−Mataga plot for **6** (circles), **7** (squares), and **8** (triangles). The solvents are from left to right: C_6H_{12}, Bu_2O, Et_2O, MTBE, EtOAc, THF, CH_2Cl_2, DMSO, PrCN, DMF. Cyclohexane is excluded from the correlation.

Table 3. Fitted Parameters from Eq 1

	$\tilde{\nu}_f^{vac}$/cm^{-1}	$(2\vec{\mu}_e(\vec{\mu}_e - \vec{\mu}_g))/4\pi\epsilon_0 hc a_0^3$/cm^{-1}
1	27120	−33330
2	26120	−30470
3	25840	−29570
4	27620	−32710
5	26730	−32520
6	28200	−31020
7	26380	−30060
8	24820	−30050

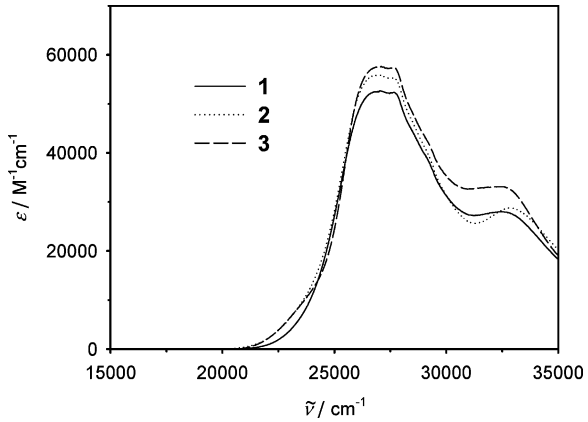

Figure 4. Absorption spectra of **1**−**3** in CH_2Cl_2.

absorption and fluorescence behavior of **6**−**8** is analogous to the dialkylamino substituted species described by HK.[49]

$$\tilde{\nu}_f = \tilde{\nu}_f^{vac} - \frac{2\mu_e(\mu_e - \mu_g)}{4\pi\epsilon_0 hc a_0^3}\left(f(\epsilon) - \frac{1}{2}f(n^2)\right) \text{ with}$$

$$f(\epsilon) = \frac{\epsilon - 1}{2\epsilon + 1} \text{ and } f(n^2) = \frac{n^2 - 1}{2n^2 + 1} \quad (1)$$

The absorption spectra of the cascades **1**−**5** (see Figures 4 and 5) are much less structured than those of **6**−**8** due to severe band overlap. The main feature that is added is a very intense band at ca. 27 000 cm^{-1} which is due to the tolandiamine moiety. This band overlaps strongly with the CT band at ca. 25 000 cm^{-1} which is only seen as a low-energy tail of the tolandiamine band which prevents a reasonable band deconvolution. From Figure 4, it is obvious that the substitution pattern has only a marginal influence on the absorption spectra with exception of the low-energy tail which is more intense in **3** due to the MeO substituent at **Tara1** which makes it a stronger donor compared to **Tara1** in **1** and **2**. The absorption spectra of **4** and **5** are quite similar because both species have the same number of **Tara** groups and tolandiamine units. This observation supports the conceptual approach of dividing the cascades into the above-mentioned moderately interacting units.

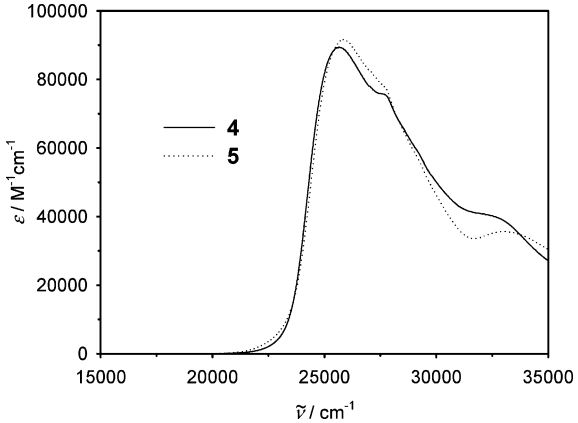

Figure 5. Absorption spectra of **4** and **5** in CH_2Cl_2.

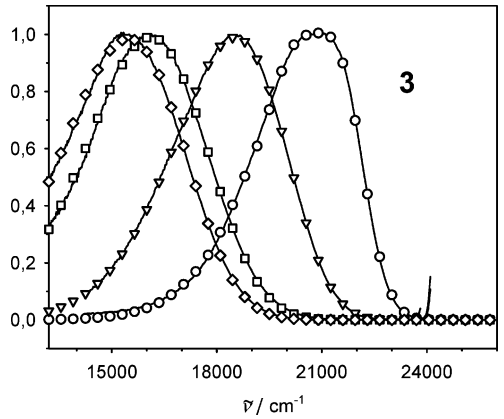

Figure 6. Reduced $(I(\tilde{\nu}_f)/\tilde{\nu}_f^3$ vs $\tilde{\nu}_f)$ and normalized fluorescence spectra (solid lines) of **3** from left to right in THF, Et_2O, Bu_2O, C_6H_{12}, and simulation by eq 2 (symbols).

The fluorescence spectra of **1**−**5** (see Figure 6) are strongly solvatochromic and are very similar in energy and band shape to those of **6**−**8**, irrespective of the excitation energy. However, while there are significant differences in the Stokes shift of **6**−**8** due to strong substituent effects, the fluorescence energy maxima for **1**−**5** are very similar in a given solvent. The slopes of the Lippert−Mataga plots of **1**−**5** are also in good agreement with those of **6**−**8**. Excitation spectra of all compounds are identical to the absorption spectra and prove complete energy transfer to the S_1 state, irrespective of excitation energy. In addition, no fluorescence from other states, e.g., local tolandiamine states was observed which should occur between 25 000 and 20 000 cm^{-1}. For comparison, the fluorescence of tolandiamine **9** occurs between 24 700 cm^{-1} (cyclohexane) and 20 000 cm^{-1} (DMSO) with quantum yields of 0.60 and 0.70. Altogether, these features prove that the fluorescent state in the cascades has the same electronic nature as that in the **A-Tara1** species **6**−**8**, i.e., all cascades emit from a more or less dipolar CT state localized in the **A-Tara1** moiety.

Table 4. Reorganization Energies and Free Energy Difference of **3** as Derived from Eq 2

	λ_v/cm^{-1}	λ_s/cm^{-1}	ΔG_{00}/cm^{-1}	$\tilde{\nu}_v$/cm^{-1}
C_6H_{12}	1100	1240	−23250	1450
Bu_2O	1240	2080	−22510	1400
MTBE	1210	2620	−21980	1400
1,4-dioxane	1100	2600	−21740	1400
Et_2O	1140	3670	−21790	1400
EtOAc	1170	3740	−21340	1400
THF	1090	3650	−21080	1400
CH_2Cl_2[a]	1440	3400	−19520	1400

[a] Bad signal-to-noise ratio.

To extract the reorganization energy λ_s associated with any low-frequency vibrations (such as solvent and low energy solute motions) and the reorganization energy λ_v associated with any high energy vibrations (bond length and angle distortions) as well as the free energy difference ΔG_{00} between the relaxed excited CT and the ground-state we applied the vibrational coupling theory[52−54] based on a Golden rule expression where μ_{fl} is the fluorescence transition moment and S is the Huang−Rhys factor $\lambda_v/\tilde{\nu}_v$.The fluorescence spectra were fitted by eq 2, where $\tilde{\nu}_v$ is an averaged high-frequency mode associated with λ_v.

$$I_{fl}/\tilde{\nu}^3 = \frac{16 \times 10^6 \pi^3}{3\epsilon_0} \frac{n(n^2+2)^2}{9} \mu_{fl}^2 \sum_{j=0}^{\infty} \frac{e^{-S} S^j}{j!} \sqrt{\frac{1}{4\pi hc\lambda_s kT}} \exp\left[- \frac{hc(j\tilde{\nu}_v + \lambda_s + \tilde{\nu} + \Delta G_{00})^2}{4\lambda_s kT} \right] \quad (2)$$

The fitted reorganizational parameters are collected in Table 4 for **3** and the fits are displayed in Figure 6. An averaged vibration $\tilde{\nu}_v$ = ca. 1400 cm^{-1} was used for the fits which roughly correlates to a C−N vibration. Although the partitioning of the total reorganization energy into λ_s and λ_v is somewhat arbitrary, the free energy ΔG_{00} is rather accurate and decreases with increasing solvent polarity. However, the sum of both reorganization energies compares well with those of tetraaryltolandiamine radical cations in CH_2Cl_2 which is ca. 6000 cm^{-1}.[50] Similar observations are true for all other derivatives **1**, **2**, and **4**−**8**.

B. Redox Properties. To gain insight into the energy of localized states with radical cation or radical anion character we measured the redox potentials of **1**−**8** by cyclic voltammetry (CV) in CH_2Cl_2/0.2 M TBAH solution vs Fc/Fc$^+$. The corresponding redox potentials are collected in Table 5 where they are grouped according to their redox potential range. An interpretation as to which triarylamine moiety the given potentials refer is also given in parentheses. The relatively narrow range in which the redox potential for a given type of triarylamine groups occurs shows that the coupling between the triarylamine groups is relatively small compared to the influence of the substituents (Cl, Me, MeO). The redox processes at ca. −2200 mV refer to chemically irreversible reductions of the acridine acceptor, those above 1000 mV refer to the second oxidation of the triarylamine that is most easily oxidized.

(52) Jortner, J.; Bixon, M. *J. Chem. Phys.* **1988**, *88*, 167−170.
(53) Gould, I. R.; Noukakis, D.; Gomez-Jahn, L.; Young, R. H.; Goodman, J. L.; Farid, S. *Chem. Phys.* **1993**, *176*, 439−456.
(54) Marcus, R. A. *J. Phys. Chem.* **1989**, *93*, 3078−3086.

Table 5. Redox Potentials of **1**−**8** in CH_2Cl_2/0.2 M TBAH vs Fc/Fc$^+$, v = 250 mV s^{-1}[a]

	$E_{1/2}^{red}$/mV	$E_{1/2}^{ox,1}$/mV	$E_{1/2}^{ox,2}$/mV	$E_{1/2}^{ox,3}$/mV	$E_{1/2}^{ox,4}$/mV
1	−2160[b]	260 (**Tara2**)		640 (**Tara1**)	1120[b]
2	−2130[b]	250 (**Tara2**)	530 (**Tara1**)		1100[b]
3	−2150[b]	400 (**Tara1**)		620 (**Tara2**)	
4	−2160[b]	240 (**Tara3**)	480 (**Tara2**)	680 (**Tara1**)	1030[b]
5	−2160[b]	270[c] (**Tara2**)		630 (**Tara1**)	1050[b]
6	−1730[b]			690 (**Tara1**)	1320[b]
7	−2080[b]		460 (**Tara1**)		
8	−2140[b]	290 (**Tara1**)			1020[b]

[a] The assignments in parentheses refer to the triarylamine group that is oxidized at the given potential. [b] Irreversible process, peak potential. [c] Two electron transfer, not resolved.

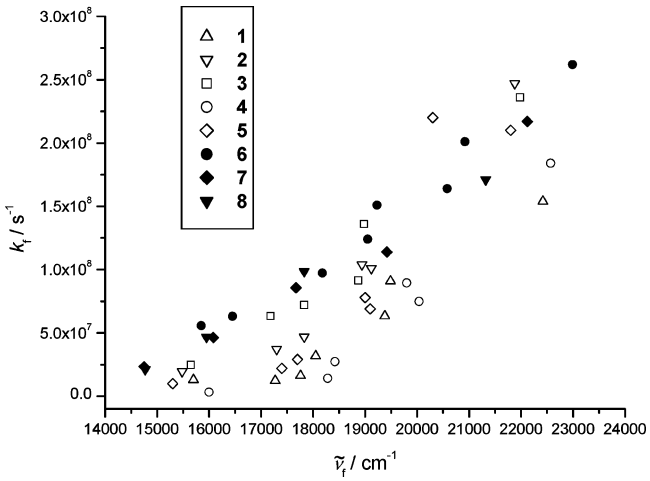

Figure 7. Rate constant of the radiative process k_f vs fluorescence transition energy $\tilde{\nu}_f$ for **1**−**8** in different solvents.

The redox potentials for **1**, **2**, **4**, and **5** show that the energy cascade for an excited state with predominantly localized triarylamine radical cation character is downhill for the migration of a hole from **Tara1** to **Tara2** and **Tara3**. Much in contrast it is uphill for **3** where the triarylamine substituents (Cl, MeO) are exchanged in comparison with **1**.

C. Time-Resolved Fluorescence Properties. Time-resolved fluorescence decays τ_f for **1**−**8** were measured in the nanosecond regime in selected solvents that cover the range from totally apolar (cyclohexane) to highly polar (DMSO). In all cases a single-exponential decay was observed. In addition, we measured the fluorescence quantum yield Φ_f in all solvents. The quantum yields vary depending on the solvent from being low in apolar solvents and in rather polar solvents with a maximum of quantum yield in between up to 0.90 (see Table 2). From both quantities, τ_f and Φ_f we calculated the rate constant for the radiative (k_f) and nonradiative decay (k_{nr}) according to eqs 3 and 4.

$$\Phi_f = \frac{k_f}{k_f + k_{nr}} \quad (3)$$

$$\tau_f = \frac{1}{k_f + k_{nr}} \quad (4)$$

Both a plot of k_{nr} and of k_f for compounds **1**−**8** in different solvents vs the fluorescence energy shows a relatively narrow scattering range of data points (see Figures 7 and 8), Therefore, it is obvious that the photophysics of **1**−**8** in the nanosecond

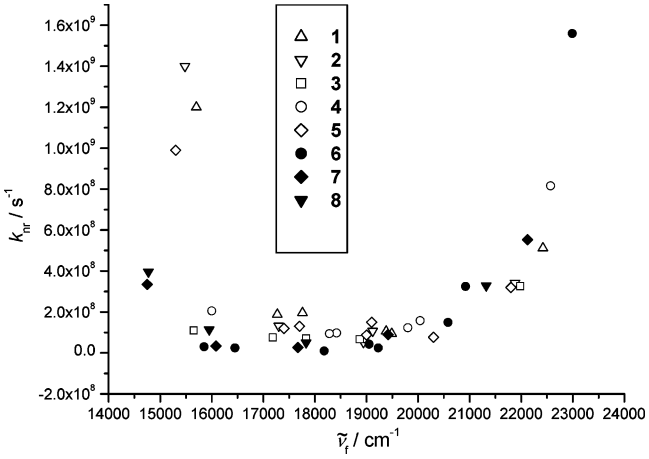

Figure 8. Rate constant of the nonradiative process k_{nr} vs fluorescence transition energy $\tilde{\nu}_f$ for **1**−**8** in different solvents.

time domain are energy controlled, that is, the energy of the fluorescent **A-Tara1** located CT state dominates its deactivation kinetics. The fluorescence energy can either be tuned by substituents (Cl, Me, MeO, Tara2, etc.) or by the solvent (apolar > polar).

As one can see in Figure 8 k_{nr} is practically constant between 16 000 and 20 000 cm^{-1} while above 20 000 cm^{-1} k_{nr} rises strongly. This increase with increasing fluorescence energy was also found by HK in carbazole derivatives[55] and was interpreted by a dominating intersystem crossing (ISC) from the fluorescent CT state to a lower lying triplet state. However, as we will see below we did not find any evidence in the transient absorption (TA) spectra for the population of a long-lived triplet state. The reason of the k_{nr} increase for $\tilde{\nu}_f$ > 20 000 cm^{-1} thus remains cumbersome. For the energies below 16 000 cm^{-1} the set of derivatives **1**−**8** splits into two groups: those derivatives whose nonradiative rate constant remains essentially constant or increases slightly (**6**−**8** and **3**) and those of which k_{nr} dramatically increases by roughly one order of magnitude (**1**,**2**,**5**). Obviously, the above-mentioned energy control of deactivation kinetics fails for the latter group of compounds. For compound **4** there is no data point low enough in energy in order to decide to which group it belongs, however, we will present evidence below that **4** also is likely to belong to the latter group.

The increase in k_{nr} for **1**, **2**, **4**, and **5** is due to an additional deactivation pathway. Though superficially very similar, the contrasting k_{nr} behavior of **3** vs **1** and **2** shows that the lack of an additional deactivation pathway in **3** is due to the fact that **3** displays an uphill gradient for hole migration while **1** and **2** possess a downhill gradient. Therefore, we assume that the additional nonradiative deactivation pathway is a hole transfer (HT) from **Tara1** to **Tara2** in **1** and **2**. This hole migration is only downhill in rather polar solvents, because, in contrast to the oxidation processes observed in CV, hole migration from an excited **A-Tara1** CT state involves a charge separation which is unfavorable in apolar solvents. Much in contrast, the hole migration is uphill for **3** in all solvents and, thus, no additional nonradiative deactivation is observed. To assess whether a photoexcitation process followed by a hole migration can be responsible for the above-mentioned additional fluorescence quenching effect we employ the Rehm−Weller equation. Equation 5 can be used to estimate the free energy for the PET-hole migration process $\Delta G°$ by subtracting the redox potential difference ΔE of donor (**Tara2**) and acceptor (**A**) from the free energy difference of the ground and excited CT state potential energy surface minima ΔG_{00}.[56] The redox potential difference can be obtained from the values in Table 5 which refer to CH_2Cl_2/0.2 TBAH solution: ΔE = 0.260 V (**Tara2**) − (−2.160 V (**A**)) = 2.420 V for **1** and ΔE = 0.620 V (**Tara2**) − (−2.150 V (**A**)) = 2.770 V for **3**. The free energy ΔG_{00} in CH_2Cl_2 is taken from the fits of eq 2 (Table 4) which can be estimated to be ca. 20 000 cm^{-1} for **1** (the ΔG_{00} value for CH_2Cl_2 could not be determined for **1** because of the bad signal-to-noise ratio of the fluorescence spectrum in CH_2Cl_2) and 19 520 cm^{-1} for **3**.

Table 6. Hole Transfer Rate from **Tara1** to **Tara2** in **1**−**5** from Fluorescence Lifetime Measurements[a]

	$k_{HT} = k_{nr}(\mathbf{x}) - k_{nr}(\mathbf{y})/10^8\ s^{-1}$ *x*/*y*				
	1/6	**2/7**	**3/8**	**4/6**	**5/7**
C_6H_{12}	(−)	(−)	(−)	(−)	(−)
MTBE	(−)	0.1	0.17	(−)	0.6
1,4-dioxane	(−)			(−)	
EtOAc	1.6			0.55	
THF	1.7	1.0	(−)	0.71	0.93
CH_2Cl_2	12	14	(−)	2.0	9.6

[a] (−) indicates no hole transfer (k_{HT} is negative).

$$\Delta G° = 8065.5[E°(\mathbf{Tara2}) - E°(\mathbf{A})] - \Delta G_{00} \qquad (5)$$

Eq 5 yields $\Delta G°$ = −500 cm^{-1} for **1** but +2820 cm^{-1} for **3**. Although the Rehm−Weller equation only allows a very rough estimate of the free energy of a PET the exergonic value for **1** suggests that a hole migration from the **A-Tara1** CT state to **Tara2** is energetically favorable while the endergonic value for **3** explains why we cannot observe hole migration, and, consequently no additional fluorescence quenching pathway. The same holds true for **2** for which ΔG^0 = ca. −200 cm^{-1}. Because the cascade **4** and the dendrimer **5** possess very similar fluorescence energy properties and redox potential values we expect hole migration also to be possible in polar solvents. In fact, for **5** the rather high nonradiative rate constant suggests a similar process. For the cascade **4**, we were unable to measure the rate constant in a solvent more polar than CH_2Cl_2 for which the hole transfer is distinctly favorable. In any case, the free energy values derived by the Rehm−Weller equation for **1** and **2** are rather small so that small changes in the medium polarity can switch the system in a way that hole migration to **Tara1** or **Tara2** is favorable or unfavorable while for **3** it is an unfavorable uphill process independent of the solvent. From the fluorescence lifetime data (see Table 2) we can estimate the hole transfer rate k_{HT} from **Tara1** to **Tara2** in **1**−**5** by the difference between k_{nr} of these compounds and the reference compounds **6**−**8** as given in Table 6. The reference compounds were chosen as to match the **A-Tara1** moiety in **1**−**5** as close as possible. A negative sign of k_{HT} indicates that no hole migration is possible either because it is against the redox gradient as in **3** or it is because less polar solvents disfavor charge separation.

(55) Kapturkiewicz, A.; Herbich, J.; Karpiuk, J.; Nowacki, J. *J. Phys. Chem. A* **1997**, *101*, 2332−2344.

(56) Kavarnos, G. J. *Fundamentals of Photoinduced Electron Transfer*; VCH: Weilheim (Germany), 1993.

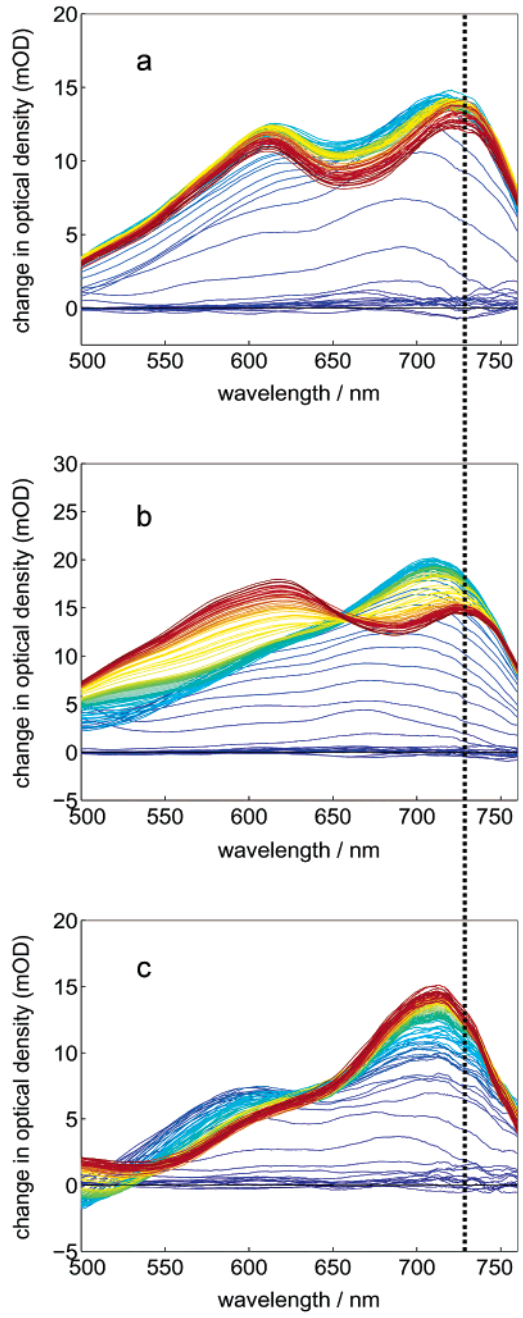

Figure 9. Temporal evolution of the pump−probe spectra of **8** in different solvents; (a) acetontrile, (b) benzonitrile, (c) MTBE, within the first 20 ps after excitation (step size: 60 fs). Early spectra are shown in blue/green and late spectra are shown in orange/red colors.

D. Femtosecond Pump−Probe Spectra. Excited-State Dynamics of 8. To elucidate the photophysical mechanisms in the model redox cascades it is crucial to investigate first the dynamics after photoexcitation in the acridine-triarylamine D−A systems without the tolandiamine "antenna". Figure 9 shows the temporal evolution of the pump−probe-spectra of **8** measured in three different solvents after excitation at 360 nm (27 800 cm^{-1}). Immediately after excitation there is a broad transient absorption band showing a weak bifurcation with weakly pronounced maxima centered around 610 and 690 nm. Note that this initial spectral distribution—which rises within the pulse duration of our experimental setup (~80 fs)—is almost solvent independent (Figure 9a−c, blue spectra). After several 100 fs, however, the evolution becomes strongly solvent dependent. In acetonitrile (Figure 9a) the initial two peak distribution becomes more pronounced while the band at 690 nm undergoes a shift to 725 nm. Reference measurements on dianisylphenylamine have shown that the lowest excited singlet state of these compounds absorb at ~700 nm. At the same time dianisylarylamine radical cations absorb at around 730 nm.[3] Hence, upon charge transfer in **8** one would expect to observe a dynamical shift in this spectral region. Acridine radical anions are known to have an absorption band at ~610 nm.[57] Thus, the temporal evolution of **8** in acetonitrile reflects an ultrafast *photoinduced* (as opposed to *optical*) charge transfer from triarylamine to the acridine unit in less than 2 ps.

In benzonitrile (Figure 9b) the initial spectral bifurcation is merging into a pronounced band at 700 nm which reaches its maximum intensity after 500 fs. The onset of charge transfer is marked by a spectral shift of the amine radical cation band (accompanied by a drop in intensity) as well as by the rise of the band of the acridine radical anion (610 nm). In contrast to acetonitrile, where the charge-transfer process leads to a continuous spectral shift the results in benzonitrile reveal characteristic "two-level" kinetics with a well pronounced isosbestic point at 660 nm.

Finally, in MTBE we observe the rise of the triarylamine excited-state absorption band at 710 nm. However, the rise is not followed by a spectral shift toward 730 nm (triarylamine radical cation) and the acridine radical anion band around 610 remains absent as well. Consequently, there is no evidence for the population of a strongly dipolar CT state in MTBE.

From the results shown in Figure 9 the following mechanistic picture emerges. Excitation of **8** leads to a largely delocalized excited state with similar electronic (and geometrical) structure in acetonitrile, benzontrile and MTBE. Immediately after excitation, coupling to various nuclear modes (both internal and solvent modes) leads to energy localization on the time scale of 100 fs to 1 ps. The spectroscopic signatures found in the transient absorption spectra suggest that—in all three solvents—a locally excited (LE) triarylamine state is formed shortly after excitation. Reference measurements on dianisylphenylamine have shown that the lowest excited singlet state of these compounds absorb at ~700 nm. In the polar acetonitrile, ultrafast energy localization competes with charge transfer which occurs on the same time scale. In benzonitrile, the thermodynamic driving force for CT is much smaller which leads to a reduced CT rate. Hence, energy localization and CT are clearly separable processes. Finally, in MTBE the thermodynamics for CT are highly unfavorable and thus the triarylamine excited-state cannot undergo efficient CT.

CT and Effect of Driving Force in Tolandiamine-Bridged Systems. Photoexcitation of **1**−**5** at the pump wavelength (360 nm = 27 800 cm^{-1}) initially populates a tolandiamine state (see Figure 10) because this unit has the highest absorptivity at this energy (see Figures 4 and 5). Hence, the tolandiamine units serve as antenna system. These tolandiamine states are expected to be the precursor states for ultrafast intramolecular energy transfer to the corresponding charge transfer states. Immediately after photoexcitation of **1** and **3** we observe a broad, structureless absorption between 500 and 700 nm (see Figure 10a). This band

(57) Shida, T. *Electronic Absorption Spectra of Radical Ions*; Elsevier: Amsterdam, 1988.

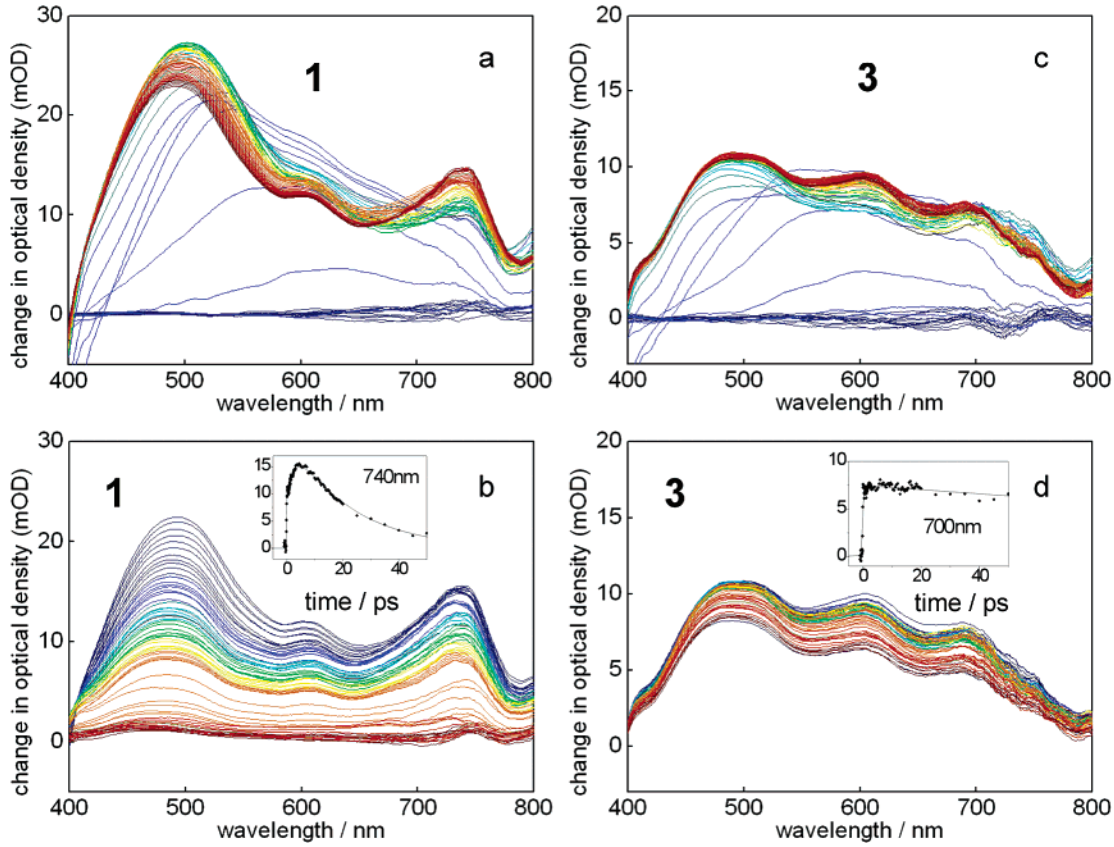

Figure 10. Temporal evolution of the pump−probe spectra of **1** (a, b) and **3** (c,d) in acetonitrile, the upper panels (a) and (c) show early spectra from −1.0 to 3 ps after excitation (60 fs step size). The lower panels (b) and (d) represent the spectra 3 to 130 ps after excitation (various step sizes). Early spectra in each panel are shown in blue/green and late spectra are shown in orange/red colors. The insets show the time-dependent absorption at 740 and 700 nm, respectively (see text for details).

represents the absorption of the unrelaxed Franck Condon state populations. After several 100 fs, there are three main transient absorption bands, the 610 nm (acridine radical anion), the 700−740 nm band (triarylamine radical cation), and a very intense band at 490 nm which must be assigned to excited-state absorption of the tolandiamine system. A similar transient absorption band at 480 nm is also visible in the spectra of tolandiamine **9** in MeCN. The fact that the tolandiamine band at 490 nm is present throughout the lifetime of the excited states of **1**−**5** must be viewed as a clear indication that the transient absorption spectra cannot be reconstructed by (diabatic) mixing of spectral reference components obtained from separate measurements. Hence, the electronic coupling between the chromophores is significant.

Figure 10 also displays the time-dependent transient absorption signal of the 740 nm band. In contrast to **8** (acetonitrile) where this band rises within the time resolution of our experimental setup the rise of this band in **1** is strongly biexponential, i.e., it shows a rise time of 4 ps (40%). This rise time must be interpreted as the hole transfer time from the triarylamine (**Tara1**) which is adjacent to the acridine to the terminal amine (**Tara2**).

Because of the substitution scheme in **3** hole transfer between the central and the terminal amine unit is thermodynamically unfavorable. Hence, a long-lived charge transfer state of the type $\mathbf{A}^{-}-(\mathbf{Tara1})^{+}-\mathbf{Tara2}$ is formed. Entirely consistent with this proposal is the fact, that the rise of the 700 nm band in **3** is not showing a ps component (see Figure 10 inset).

A comparison of the 740 and 700 nm transients of **1** and **3** (insets of Figure 10) reveals a significantly longer lifetime of the CT state of **3**. However, in addition to these differences the intensity ratio reveals also interesting information about the excited-state relaxation in **1** and **3**. Most obvious is the difference in the relevant contribution of the 610 nm band which is significantly stronger in **3** than in **1**, suggesting a more localized, twisted acridine radical anion in **3** than in **1**. In fact, this interpretation is in agreement with the rest of our data: In **3** the charge is only being transferred between the acridine and the adjacent **Tara1** amine unit. To establish a large dipole moment the acridine has to twist to electronically decouple from the rest of the aromatic system. This will result in a fairly pure acridine radical anion band. The CT state dipole moment of **1** is somewhat larger than that of **3** (see the larger slope of **1** vs **3** in the Lippert−Mataga plot, Table 3), however one has to bear in mind that the positive charge is delocalized much farther over the second amine unit. Hence, the negative charge on the acridine will also be delocalized. As a result, the radical anion character is "diluted" which is manifested in the reduced 610 nm band.

Effect of the Redox Cascade Extension. Figure 11 shows the temporal evolution of the pump−probe spectra of **4** and **5** in acetonitrile. The insets display the time-dependent transient absorption at 740 nm (triarylamine radical cation band). From a comparison of the symmetrical "doubly branched" system **5** with its single-branch analogue **1** it becomes clear that the spectral properties are very similar (both in time evolution and

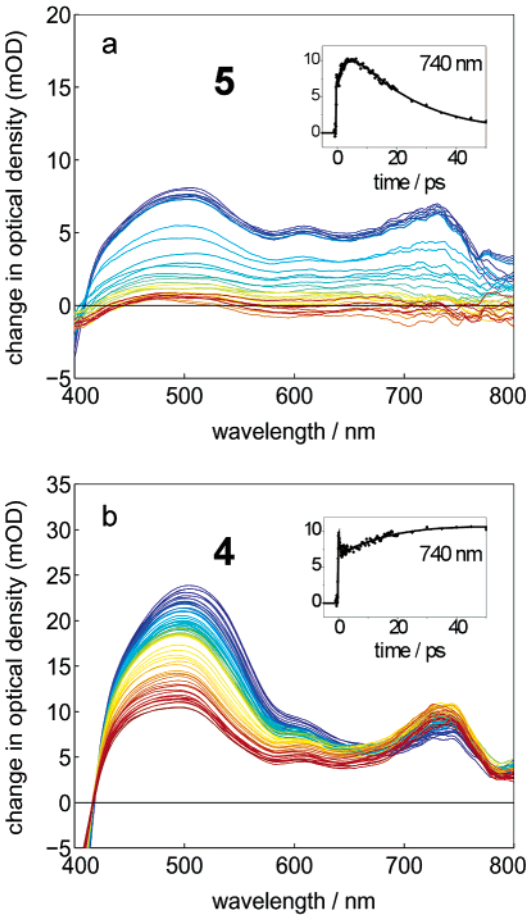

Figure 11. Temporal evolution of the pump−probe spectra of (a) **5** and (b) **4** in acetonitrile, 3 ps to 150 ps after excitation (various step sizes). Early spectra are shown in blue/green and late spectra are shown in orange/red colors. The insets show the time-dependent absorption at 740 nm (see text for details).

in spectral distribution) suggesting that the two tolandiamine branches are acting as independent substituents.

Figure 11b shows the pump−probe spectra of the extended redox system **4**. Most noticeable is the kinetic behavior (inset 11b) which differs qualitatively and quantitatively from all other systems. The instant rise of the 740 nm signal is followed by an ultrafast decay (200−300 fs) and then another slow rise with a time constant of 20 ps. These characteristics can be explained by assuming that the signal is a composite of two overlapping spectral contributions. Given the structure of **4** it seems reasonable to propose the following model: Photoexcitation at 360 nm of the tolandiamine units leads to two parallel processes: a direct charge separation from the tolandiamine excited-state yielding **A**$^-$**-Tara1-Tara2-(Tara3)**$^+$ (which occurs in 200−300 fs) and a slower *indirect* hole transfer from the CT state **A**$^-$**-(Tara1)**$^+$**-Tara2-Tara3** to **A**$^-$**-Tara1-Tara2-(Tara3)**$^+$ in 20 ps (see Figure 12). The latter process is analogous to the ones observed in the shorter cascades. In **4** there are actually two similar but distinctly different tolandiamine groups which should result in (partially) overlapping absorption transitions. Nevertheless, these two tolandiamine units are likely to exhibit different reactivity with respect to hole transfer. The direct charge separation process can be rationalized based on the fact that the tetraaryl tolandiamine adjacent to the acridine is actually an electron D/A moiety which can form biradical intermediates. Hence, upon excitation of the tolandiamine system in **4** there

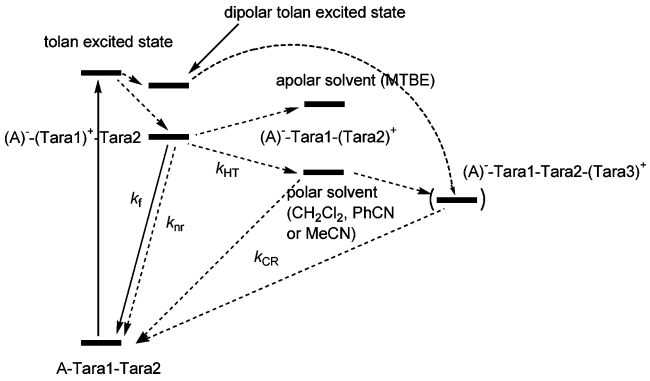

Figure 12. State diagram for **1**, **2**, and **5** (left-hand side) and for **4** (extension right-hand side).

Table 7. Rise Time τ_{HT} of the TA Peak at Ca. 740 nm and k_{HT} as Well as Life Time τ_{CR} of the Final Charge Separated State and k_{CR} of the Charge Recombination.

	acetonitrile (TA)		benzonitrile(TA)		CH_2Cl_2
	τ_{HT}/ps (k_{HT}/10^9 s^{-1})	τ_{CR}/ps (k_{CR}/10^9 s^{-1})	τ_{HT} /ps (k_{HT} /10^9 s^{-1})	τ_{CR}/ps (k_{CR}/10^9 s^{-1})	(fluoresc.) (k_{HT}/10^9 s^{-1})
1	3.2 (310)	22 (45)	30 (33)	180 (5.5)	(1.2)
4	20 (50)	410 (2.5)	250 (4)	>2000 (<0.5)	(0.20)
5	2.3 (440)	23 (44)	28 (36)	480 (2.1)	(0.96)

is—dependent on the conformation of the molecule—an initial extent of charge separation which will immediately undergo relaxation toward the final extended charge transfer state within 200−300 fs.

The rate constants for HT and charge recombination resulting from spectra deconvolution of the pump−probe measurements for **1**, **2**, **4**, and **5** in acetonitrile and benzonitrile are collected in Table 7. From these data it is apparent that the extension of the cascade (**4** vs **1**) slows down both k_{HT} and k_{CR} by one order of magnitude. In the same way, replacement of the polar acetonitrile by the less polar benzonitrile slows down both rate constants by one order of magnitude because back electron transfer occurs in the Marcus inverted region. For comparison, the rate constants k_{HT} from fluorescence measurements in CH_2Cl_2 are also given in Table 7. The values are still smaller than those obtained in benzonitrile because CH_2Cl_2 is somewhat less polar than benzonitrile.

Conclusions

From the fluorescence data in Table 6 it is obvious that the hole transfer from **Tara1** to **Tara2** is rapid and is the same for **1**, **2** and **5** in CH_2Cl_2 within experimental error. The hole transfer can compete very efficiently with the deactivation pathways in the reference chromophores as can be seen from the fluorescence quantum yields which are very low for **1**, **2**, **4**, and **5** (0.01−0.02 in CH_2Cl_2) but high for the reference compounds **6** and **7** (0.90 and 0.58, respectively, in CH_2Cl_2). Interestingly, there is no significant difference for the hole transfer rate in the branched molecule **5** compared to the linear array **1**. However, the hole transfer from **Tara1** to **Tara2** in **4** is significantly slower because of the lower free energy difference between **Tara2** and **Tara1** in **4** compared to that in e.g. **1** due to the methyl substitution in **Tara2** of **4**. This conclusion is fully supported by the pump−probe measurements in acetonitrile and benzonitrile. The hole transfer in **1**, **2**, **4**, and **5** should lead to a charge separation, i.e., a negative charge on acridine (**A**), and a positive

charge on **Tara2**. In the case of **4** one can expect that the smaller redox potential of **Tara3** compared to **Tara2** leads to a second hole transfer step in which the hole migrates to the terminal **Tara3**. If less polar solvents than CH_2Cl_2 are used, hole transfer in **1**, **2**, **4**, and **5** is either too slow or even unfavorable because the free energy difference of charge separation is very sensitive to the polarity of the solvent. In the case of **3**, the hole transfer is unfavorable irrespective of the solvent due to the wrong direction of the redox gradient.

The temporal evolution of the fs-broadband pump−probe spectra provides detailed insight into the photophysical properties of **1**−**8**, e.g., the data show that the extent of charge separation in the CT state of **8** strongly depends on the solvent. While in acetonitrile rapid energy localization competes with photoinduced charge transfer in benzonitrile these processes are distinctly separated on the time scale, the latter process being absent in MTBE.

The analysis of the TA spectra of **1** and **3** prove the HT process of **1** in polar solvents along the redox gradient while this process is uphill in **3**. The TA spectra also reveal the close analogy of the branched **5** to the single cascade **1**. For the extended cascade **4** the TA spectra suggest that two different processes lead to the final charge separated state, a direct charge separation which follows the excitation of the tolandiamine antenna moieties and a much slower process which involves the generation of a CT state followed by a HT step analogous to those in **1** and **5**. In the compounds **1**, **2** and **5** but especially in **4** the tolandiamine moieties not only serve as the cascade backbone but also possess a distinct antenna effect which collects all primary excitation energy.

In conclusion, we were able to show that acridine-triarylamine redox cascades can be used in efficient photoinduced electron-transfer processes. This PET can be governed by fine-tuning of the local redox potentials of the triarylamine redox centers, i.e., the redox gradient along the cascade molecules. Close analogy to triarylamine compounds used in optoelectronic devices make the presented arrays hopeful candidates for applications in, e.g., solar cells or photoconductors.

Experimental Section

Cyclic Voltammetry. The electrochemical experiments have been performed using a conventional three-electrode setup with a platinum disk working electrode in dry, argon-saturated CH_2Cl_2 with 0.2 M tetrabutylammonium hexafluorophosphate (TBAH) as supporting electrolyte and 0.001 M substrate. The potentials are referenced against ferrocene (Fc/Fc^+). The reversibility or irreversibility, respectively, of all redox processes were checked by measurements at different scan rates.

UV−vis/NIR and Fluorescence Spectroscopy. The UV−vis/NIR spectra were recorded with a JASCO V570 spectrometer in transmission. Steady-state fluorescence spectra were recorded with a PTI QuantaMaster Model QM-2000-4 spectrometer using degassed, argon saturated solvents in the μM concentration range. The spectra are corrected for the wavelength sensitivity of the detector. Spectra are converted to wavenumber scale by multiplication of the intensity with λ^2. Fluorescence quantum yields were determined relative to rhodamine 101 in EtOH (conc = ca. 1 μM) which has a quantum yield of 1.00. The quantum yields are corrected for the index of refraction of the solvent. Fluorescence decays were measured with a PTI TimeMaster Model TM-2/2003 stroboscopic boxcar spectrometer and a flash lamp charged with a H_2/N_2 1:1 mixture. Excitation wavelength was 381 nm for all compounds. The instrument response function was obtained by using a dilute coffee creamer as a scatterer. The decay fits were single exponential in all cases as checked by the χ^2 value, the Durbin−Watson parameter and the final residuals.

Femtosecond Broadband Pump−Probe Setup. A detailed description of the setup has been been given elsewhere.[58] Briefly, the compounds were exited by pump pulses at 360 nm at $5 \times 10^{-4} - 5 \times 10^{-6}$ M sample concentration. The changes in optical density were probed by a femtosecond white-light continuum (WLC) generated by tight focusing of a small fraction of the output of a commercial Ti:Sapphire based pump laser (CPA-2001, Clark-MXR) into a 3 mm CaF_2 plate. The obtained WLC provided a usable probe source between 370 and 720 nm. The WLC was split into two beams (probe and reference) and focused into the sample using reflective optics. After passing through the sample both probe and reference were spectrally dispersed and simultaneously detected on a CCD sensor. The pump pulse (340 nm, 100−200 nJ) was generated by frequency doubling of the compressed output of a commercial NOPA system (Clark-MXR, 680 nm, 8 μJ, 30 fs). To compensate for group velocity dispersion in the UV-pulse we used an additional prism compressor. Independent measurements of the chirp of the WLC were carried out to correct the pump−probe spectra for time-zero differences. The overall time resolution of the setup was obtained from the rise time of the signal (above 580 nm). Assuming a Gaussian shape cross-correlation we obtained a width of 100−120 fs (fwhm). A spectral resolution of 7−10 nm was obtained. Measurements were performed with magic angle geometry (54.7°) for the polarization of pump and probe pulses to avoid contributions from orientational relaxation. Pump energy and pump spot size (~200−400 μm) were adjusted to minimize contributions from the solvent to the signal. Steady-state absorption and fluorescence spectra of the samples measured before and after the time-resolved experiments were compared with each other and no indications for degradation were found. A sample cell with 1.25 mm fused silica windows and a light path of 1 mm was used for all measurements. No indications for aggregation could be observed in the measurements.

Acknowledgment. This work was supported by the Fonds der Chemischen Industrie, the Deutsche Forschungsgemeinschaft, the Volkswagenstiftung, and the Bayerisches Staatsministerium für Wissenschaft, Forschung und Kunst (FORMAT project). We thank JASCO GmbH Deutschland as well as Heraeus GmbH for kind support.

Note Added after ASAP Publication. After this article was published ASAP on July 7, 2005, a production error in the redox potential difference equation for **1** in the text just above eq 5 was discovered. The corrected version was published ASAP on July 11, 2005.

Supporting Information Available: Synthetic details and characterization for all compounds. X-ray crystallographic analysis data for **8**. This material is available free of charge via the Internet at http://pubs.acs.org.

JA0511570

(58) Raytchev, M.; Pandurski, E.; Buchvarov, I.; Modrakowski, C.; Fiebig, T. *J. Phys. Chem. A* **2003**, *107*, 4592−4600.